BOUNDARY LAYER FLOWS OVER SHARP AND SPHERICALLY BLUNTED CONES AT ANGLE OF ATTACK TO SUPERSONIC NONUNIFORM FREE STREAMS

by

Michael C. Frieders

Thesis submitted to the Graduate
Faculty of the Virginia Polytechnic
Institute and State University in partial
fulfillment of the requirements for the degree of

MASTER OF SCIENCE
in
Aerospace Engineering

APPROVED:

Dr. C. H. Lewis, Chairman

Dr. D. P. Telionis

Dr. J. A. Schetz

Dr. Y. J. Wu

March 1973
Blacksburg, Virginia

ACKNOWLEDGEMENTS

The author wishes to express his appreciation to his wife for her patience with the extended and time consuming nature of this study.

Appreciation is also extended to the following people:

Dr. C. H. Lewis for his guidance and support of this study.

for teaching the author everything he knows about computers.

Dr. J. A. Schetz, Dr. D. P. Telionis, and Dr. Y. Wu for serving on the reviewing committee.

, , and for their support of this project at sometimes unreasonable hours.

TABLE OF CONTENTS

LIST OF SYMBOLS

The following list of symbols is divided according to sections of the report from which the symbols come. Duplication of many symbols in the various areas covered by this study have made this necessary.

II (1) General Description

A	velocity defect parameter
B	velocity defect parameter, controls the width of the wake
V	total velocity
y	radial distance to a point in the flow field
ω	slope of shearing velocity profile

II (2) Governing Equations of the Three-Dimensional Solution

A_i	coefficients of the transformed boundary-layer equations
C_p	specific heat at constant pressure, $C_p = \overline{C}_p/R$
G	similarity parameter, $G = v/v_e$
h_1, h_2	surface scale factors in the ξ and η directions, $h = \overline{h}/\overline{L}$
h_3	transformed normal scale factor in the ζ direction
H	similarity parameter, $H = w/u_e$
K	thermal conductivity
$\overline{L}$	reference length
P	nondimensional pressure, $P = \dfrac{\overline{P}}{\overline{\rho}_\infty \overline{u}_\infty^{\,2}}$

Pr Prandtl number, $Pr = \dfrac{\bar{\mu}\bar{C}_p}{\bar{K}}$

R universal gas constant

Re reference Reynolds number, $Re = \dfrac{\bar{\rho}_\infty \bar{u}_\infty \bar{L}}{\bar{\mu}_r}$

t nondimensional temperature, $t = \bar{t}/\bar{t}_r$

$\bar{t}_r$ reference temperature, $\bar{t}_r = \dfrac{\bar{u}_\infty{}^2}{R}$

u nondimensional longitudinal velocity component, $u = \bar{u}/\bar{u}_\infty$

v nondimensional cross flow velocity component, $v = \bar{v}/\bar{u}_\infty$

w transformed normal velocity component

ξ streamwise surface coordinate (see Fig. 6)

ξ^* arbitrary function used to reduce the governing equations to similarity form

η transverse surface coordinate (see Fig. 6)

ζ normal coordinate (see Fig. 6)

ℓ similarity parameter, $\ell = \bar{\mu}/\bar{t}$

ρ nondimensional density, $\rho = \bar{\rho}/\bar{\rho}_\infty$

θ similarity parameter, $\theta = t/t_e$

ϕ shear parameter

μ nondimensional viscosity, $\mu = \bar{\mu}/\bar{\mu}_r$

$\bar{\mu}_r$ reference viscosity, $\bar{\mu}_r = \bar{\mu}(\bar{t}_r)$

II (3) Governing Equations of the Axisymmetric Solution

$\bar{a}$ unit reference length

C density-viscosity product ratio, $C = \frac{\rho\mu}{\rho_e\mu_e}$

F normalized tangential velocity component, $F = u/u_e$

G stagnation enthalpy ratio, $G = H/H_e$

H nondimensional total enthalpy, $H = \bar{H}/\bar{u}_\infty^{\,2}$

P nondimensional pressure, $P = \bar{P}/\bar{\rho}_\infty\bar{u}_\infty^{\,2}$

Pr Prandtl number, $Pr = \frac{\bar{\mu}\bar{C}_p}{K}$

Re reference Reynolds number, $Re = \frac{\bar{\rho}_\infty\bar{u}_\infty\bar{a}}{\bar{\mu}_r}$

$\bar{t}_r$ reference temperature, $\bar{t}_r = \bar{u}_\infty^{\,2}/\bar{C}_p$

u nondimensional tangential velocity, $u = \bar{u}/\bar{u}_\infty$

V transformed normal velocity

w nondimensional normal velocity

x surface distance, $x = \bar{x}/\bar{a}$

y normal coordinate, $y = \frac{\bar{y}\sqrt{Re}}{\bar{a}}$

ξ transformed surface coordinate

ζ transformed normal coordinate

μ nondimensional viscosity, $\mu = \bar{\mu}/\bar{\mu}_r$

$\bar{\mu}_r$ reference viscosity, $\bar{\mu}_r = \bar{\mu}(\bar{t}_r)$

ρ nondimensional density, $\rho = \bar{\rho}/\bar{\rho}_\infty$

ψ stream function

II (4) Surface Scale Factors in the Three-Dimensional Solutions

h_1, h_2 surface scale factors in the s_1 and s_2 directions

$\bar{L}$ reference length

R see Figure 6a.

r cylindrical coordinate (see Figure 6a.)

$\bar{r}_n$ dimensional nose radius

$\bar{s}_1$, $\bar{s}_2$ dimensional arc lengths in the ξ and η coordinate directions respectively

z cylindrical coordinate (see Figure 6a.)

ξ streamwise surface coordinate $\xi = \bar{S}_1/\bar{L}$

η transverse surface coordinate (see Figure 6b.)

θ_c cone half-angle

ϕ cylindrical coordinate (see Figure 6a.)

II (5) Edge Properties

a. Axisymmetric solution

M Mach number

M_L local Mach number

T temperature, $T = \bar{T}/\bar{T}_r$

$\bar{T}_r$ reference temperature, $\bar{T}_r = \bar{u}_\infty^{\,2}/\bar{C}_p$

C' C/T_e

C Sutherland's constant for calculation of viscosity

γ ratio of specific heats

All other variables in II (5)a. are as described in II (3) above.

b. Three-Dimensional Solution

V total velocity

ϕ cross flow angle

Φ η, in degrees

γ ratio of specific heats

All other variables in II (5)b. are as described in II (2) above.

II (6) Initial Data for the Three-Dimensional Solution

$\bar{r}_n$ nose radius

$\bar{S}_w$ wind-fixed distance to points on the leeward plane of the wedge section of a blunt cone

$\bar{y}$ physical normal boundary-layer distance

α angle of attack

ϕ as used first it is an angle as defined in figure 7; as used secondly it is the cross flow angle; as used finally it is the shear parameter

All other variables used in section II (6) are as defined in section II (2) above.

II (7) Boundary-Layer Parameters

a. Axisymmetric Solution

Variables not defined in this section are defined in II (3) above.

b. Three-Dimensional Solution

Variables not defined in this section are defined in II (2) above.

III Results and Discussion: Figures

C_f skin friction coefficient, $C_f = \dfrac{2\bar{\tau}_w}{\bar{\rho}_\infty \bar{u}_\infty^2}$

P nondimensional pressure, $P = \dfrac{\bar{p}}{\bar{\rho}_\infty \bar{u}_\infty^2}$

q_w nondimensional wall heating rate $q_w = \bar{q}_w/\bar{\rho}_\infty \bar{u}_\infty^3$

Re reference Reynolds number, $Re = \dfrac{\bar{\rho}_\infty \bar{u}_\infty \bar{L}}{\bar{\mu}_r}$ where $\bar{\mu}_r$ is based on $\bar{t}_r = \dfrac{\bar{u}_\infty^2}{R}$

R_n dimensional nose radius of blunt cone

S nondimensional surface distance on a sharp cone, $S = \bar{S}_1/\bar{L}$; dimensional body-fixed surface distance on a blunt cone

T nondimensional temperature, $T = \bar{t}/\bar{t}_r$ where $\bar{t}_r = \bar{u}_\infty^2/R$

U nondimensional longitudinal velocity component, $U = \bar{u}/\bar{u}_\infty$

V nondimensional cross flow velocity component, $V = \bar{v}/\bar{u}_\infty$

ξ^* as described in II (2) above

Φ position in degrees from the windward streamline

Subscripts

aw adiabatic wall value

co normalizing value, from a uniform flow case at zero angle of attack

e edge property

n	nose condition
o	stagnation property
r	reference conditions
ref	reference condition
w	wall value
∞	free-stream condition
AXI	value from the axisymmetric solution
3-D	value from the three-dimensional solution

LIST OF FIGURES

FIGURE PAGE

SECTION I

INTRODUCTION

Methods have been developed to study the effect of nonuniform free streams on the laminar boundary layer of a sharp or spherically blunted cone at angle of attack. Study in this area has been generated by an interest in aerodynamic decelerators and the separation of stores from aircraft. In general the problem is applicable whenever an aerodynamic body encounters a supersonic wake or boundary layer of another body. Another problem of interest is the encountering of atmospheric disturbances by supersonic bodies.

This problem has been investigated by Bordner and Davis [1] for the case of a sharp cone in two-dimensional shear flow and axisymmetric wake flow. In their study they modified the three-dimensional boundary-layer program of McGowan and Davis [2] to allow the introduction of nonuniform edge properties. This was done using cubic splines to interpolate the inviscid data at the proper coordinate points. In their method, the distribution of u_e was calculated numerically from the interpolated distribution of V_e, and P_e was calculated using stagnation properties and the temperature distribution. Bordner and Davis compared their results with the small cross flow model of Moore [3]. Their conclusion was that the small cross flow model was not sufficient to predict heat transfer, skin friction, or separation in cases where there are large cross flows.

Recent studies by Lewis, Moore, Black, and DeJarnette [4] have made available a great deal of inviscid flow data for the cases of sharp and blunt cones in nonuniform free streams. Moore and DeJarnette [5] developed a program to solve for the sharp cone inviscid flow field in a nonuniform free stream. Black and Lewis [6] later incorporated the Moore-DeJarnette program into a larger system of programs capable of handling blunt cone problems as well. The resulting system of inviscid programs is an extremely versatile tool by which inviscid flow fields may be predicted for a wide range of sharp and blunt cone problems. These problems include sharp cones in two-dimensional shear flow or axisymmetric wake flow, blunt cones in axisymmetric wake flow, and either cone in uniform flow, all of which may be at zero or non-zero angle of attack.

The present study has taken advantage of the system of programs developed by Black and Lewis. In the present study the McGowan-Davis three-dimensional program has again been used as a basis for the solution of the three-dimensional boundary-layer equations; however, the incorporation of nonuniform edge properties is by a method consistent with the inviscid programs. An axisymmetric boundary-layer program by Miner, Anderson, and Lewis [7] has been modified to solve the boundary layer over the axisymmetric region of a blunt cone in a nonuniform supersonic free stream.

Separate programs have been developed for the study of sharp and blunt cones. The sharp cone program is a modification of the McGowan-Davis program alone. The blunt cone program is a merger of the modified

McGowan-Davis three-dimensional program with the modified axisymmetric program of Miner, Anderson, and Lewis. Each program has been developed in as general a sense as possible in order to give the user maximum versatility in its use. Each inviscid program has the capability of creating a set of surface data for use as boundary-layer edge properties. The two boundary-layer programs need only access the inviscid data sets to have all needed edge data. Once the "raw" data has been accessed by the boundary-layer programs, it is converted into a new data set of edge data in the form required for boundary-layer solution. This second set of data is stored in the form of Fourier coefficients and may be used as many times as required.

The major differences between the present sharp cone program and the program developed by Bordner and Davis are the methods for interpolating "raw" inviscid data as received from the inviscid programs and for calculating the final form of the edge properties. The present program expands the limited circumferential data, as supplied by the Black-Lewis programs, to the required number of planes of circumferential data by using the Fourier sine and cosine series. The expansion of data in the Bordner-Davis program was accomplished by using the spline fits already discussed. The present method for expanding the data is more efficient and is consistent with the method by which the data are generated in the inviscid programs. The distributions of u_e and P_e are calculated directly from the V_e, ϕ_e and P_e distributions of the inviscid programs, in contrast to the numerical method used by Bordner and Davis.

The blunt cone boundary-layer program employs the same methods for introduction of edge data as are used in the sharp cone program. In the axisymmetric portion of the program the assimilation of edge data is straight-forward and does not require Fourier analysis. An interpolation method has been developed to enable the use of the axisymmetric boundary-layer solution as starting data for the three-dimensional boundary-layer solution.

In this report, both sharp and blunt cone problems are investigated. Sharp cones are subjected to a two-dimensional shear flow at varying angles of attack. The flow conditions are the same as those used by Bordner and Davis. Blunt cones are subjected to axisymmetric wake flows at varying angles of attack.

Results obtained for blunt cones in uniform flow are compared to the experiments of Cleary [8] and Widhopf [9] with good agreement. The case of a sharp cone in uniform flow is compared to the experiments of Cleary [8] and to the results as predicted by the original unmodified McGowan and Davis program, both with near agreement. Skin-friction and heat-transfer data obtained for sharp and blunt cones in nonuniform flow fields show a departure from the uniform flow values. Along the windward streamline of sharp cones in two-dimensional shear flow, normalized skin-friction and heat-transfer coefficients increase relative to coni' ıl flow values. Circumferential values of the skin friction and heat transfer for nonuniform flows go through an inflection point, having values above the conical flow values on the windward side, and below the conical flow values on the leeward side. The effect of wake flow on a blunt cone is to increase the heat transfer considerably along the windward streamline, relative to uniform flow values. Downstream values of the skin-friction coefficient along the windward streamline are shown to fall below uniform flow values. Decreasing the width of the wake causes more severe departures from uniform flow values for both heat transfer and skin friction on a blunt cone. The presence of free-stream nonuniformities hastened the onset of separation for both sharp and blunt cones. The beginnings of separation occurred sooner in both the longitudinal and transverse planes. Smaller width wakes and higher angles of attack caused an earlier onset of separation.

A more detailed description of the relation between the inviscid and boundary-layer programs can be found in the general description under Section II. The results are described in more detail in Section III.

SECTION II

ANALYSIS

Following is an analysis of the problem solved by the two computer programs developed in this study. The first section is a general description of how the problem is solved. The method of solution for the inviscid flow fields is described first, since the viscous solutions follow the same pattern and require the inviscid solutions as edge properties. The second section briefly describes the governing equations. The emphasis, however, will be on subsequent sections that describe the introduction of edge properties from the inviscid solutions, and describe the method of matching the axisymmetric and three-dimensional solutions on the spherically blunted cone.

1. GENERAL DESCRIPTION

A system of computer programs has been developed to determine the supersonic inviscid and viscous flow fields over bodies in the presence of nonuniform free streams. The bodies considered in this study are sharp and spherically blunted cones at zero and non-zero angles of attack. The programs are capable of solving for the inviscid and viscous flow fields over sharp cones in two-dimensional shear flow, or in axisymmetric wake flow. The free streams over blunt cones are restricted to axisymmetric wake flows situated so that the flow in the stagnation region remains axisymmetric.

Two-dimensional shear flow is characterized by the following equation

$$\frac{V_1}{V_n} = 1 - \omega y_1$$

where ω is the slope of the velocity profile, V_n is the velocity along the stagnation streamline and V_1 is the velocity at a point y_1 from the stagnation point (Figure 1). Axisymmetric wake flow is characterized by the following equation

$$\frac{V_1}{V_\infty} = 1 - A \exp\,(-By_1^2)$$

where A is the velocity defect parameter which controls the ratio of far wake velocity to the velocity along the stagnation streamline, and B controls the width of the wake. V_1 is the velocity at a radial distance of y_1 (Figures 2 and 3).

Two basic methods have been used for solving regions of the inviscid flow field. For the stagnation region of a blunt cone an inverse method originally developed by Lomax and Inouye [10] was used. In this method the shock shape was assumed and the governing equations were solved by a finite-difference technique. An iterative technique was employed to modify the shock shape to obtain the solution for the specified body shape. This procedure was used to solve the entire subsonic region of a spherically blunted cone, and to obtain a completely supersonic initial data line used to start the solution of the flow over the remainder of the body. The blunt cone solution procedure is shown in Figure 4.

The solution procedure for the supersonic flow field over the remainder of the spherically blunted cone, and over the entire sharp cone was a method of characteristics. For cases where the entire flow field is axisymmetric, a method of characteristics program developed by Inouye, Rakich, and Lomax [11] was used. In cases where the body is at angle of attack or where shear flow is considered, a three-dimensional method of characteristics program developed by Rakich [12] was used. Since the method of characteristics is an initial value problem, an initial data surface must be provided. The initial data surface for the supersonic region of a blunt cone was generated by the inverse method as indicated above. For the sharp cone a small region of uniform flow was assumed near the nose, and the initial shock layer data were computed by standard sharp cone techniques. All of the above methods were modified and used to solve the nonuniform inviscid flow fields. These flow fields are used to provide edge properties for the solution of laminar boundary layers over the sharp or blunt cones.

For the spherically blunted cone there are three basic regions of flow. The first region is the sphere cap extending from the stagnation point to a wind-fixed plane immediately behind the sonic line. The second region is a spherical wedge section whose angle is equal to the angle of attack and has its apex at the base of the sphere cap at the windward streamline (Figure 5). The last region extends from the wedge section to the end of the cone.

Depending on the body chosen, two methods are available for solving the viscous flow field. For the sphere cap and wedge sections of the spherically blunted cone, an axisymmetric boundary-layer program developed by Miner, Anderson, and Lewis [7] has been used. Edge properties for this axisymmetric solution are generated by the modified inverse method. The solution employs the basic compressible axisymmetric boundary-layer equations transformed by the Levy-Lee's transformation equations, and solved by a finite-difference method. This procedure solves the boundary layer over the sphere cap and wedge sections of the blunt cone, and is used to obtain an initial data line for the solution of the boundary layer over the rest of the body.

A three-dimensional boundary-layer program developed by McGowan and Davis [2] has been used for the afterbody of the blunt cone, and over the entire surface of the sharp cone. Edge properties for the three-dimensional solution are generated by the method of characteristics. The solution employs the basic three-dimensional boundary-layer equations transformed by a Crocco transformation and solved by a four-point finite-difference method. This procedure predicts the boundary layer over the afterbody of the blunt cone and over the entire sharp cone.

The above boundary-layer solution methods have been modified to accommodate the geometry of a sphere-cone, and the nonuniform inviscid edge conditions.

2. GOVERNING EQUATIONS OF THE THREE-DIMENSIONAL SOLUTION

The governing equations for the entire sharp cone and the afterbody of the blunt cone are the basic three-dimensional compressible boundary-layer equations in body oriented coordinates (Fig. 6):

ξ momentum equation

$$\frac{u}{\bar{h}_1}\frac{\partial \bar{u}}{\partial \xi} + \frac{\bar{v}}{\bar{h}_2}\frac{\partial \bar{u}}{\partial \eta} + \frac{\bar{w}}{\bar{h}_3}\frac{\partial \bar{u}}{\partial \zeta} + \frac{\bar{u}\,\bar{v}}{\bar{h}_1\bar{h}_2}\frac{\partial \bar{h}_1}{\partial \eta} + \frac{\bar{v}^2}{\bar{h}_1\bar{h}_2}\frac{\partial \bar{h}_2}{\partial \xi} = -\frac{1}{\bar{\rho}\bar{h}_1}\frac{\partial \bar{P}}{\partial \xi} + \frac{1}{\bar{\rho}\bar{h}_3}\frac{\partial}{\partial \zeta}\left[\frac{\bar{\mu}}{\bar{h}_3}\frac{\partial \bar{u}}{\partial \zeta}\right]$$

η momentum equation

$$\frac{\bar{u}}{\bar{h}_1}\frac{\partial \bar{v}}{\partial \xi} + \frac{\bar{v}}{\bar{h}_2}\frac{\partial \bar{v}}{\partial \eta} + \frac{\bar{w}}{\bar{h}_3}\frac{\partial \bar{v}}{\partial \zeta} - \frac{\bar{u}^2}{\bar{h}_1\bar{h}_2}\frac{\partial \bar{h}_1}{\partial \eta} + \frac{\bar{u}\,\bar{v}}{\bar{h}_1\bar{h}_2}\frac{\partial \bar{h}_2}{\partial \xi} = -\frac{1}{\bar{\rho}\bar{h}_2}\frac{\partial \bar{P}}{\partial \eta} + \frac{1}{\bar{\rho}\bar{h}_3}\frac{\partial}{\partial \zeta}\left[\frac{\bar{\mu}}{\bar{h}_3}\frac{\partial \bar{v}}{\partial \zeta}\right]$$

Continuity equation

$$\frac{\partial}{\partial \xi}\left(\bar{h}_2\bar{h}_3\bar{\rho}\bar{u}\right) + \frac{\partial}{\partial \eta}\left(\bar{h}_1\bar{h}_3\bar{\rho}\bar{v}\right) + \frac{\partial}{\partial \zeta}\left(\bar{h}_1\bar{h}_2\bar{\rho}\bar{w}\right) = 0$$

Energy equation

$$\frac{\bar{u}}{\bar{h}_1}\frac{\partial \bar{t}}{\partial \xi} + \frac{\bar{v}}{\bar{h}_2}\frac{\partial \bar{t}}{\partial \eta} + \frac{\bar{w}}{\bar{h}_3}\frac{\partial \bar{t}}{\partial \zeta} = \frac{1}{\bar{C}_p\bar{\rho}}\left[\frac{\bar{u}}{\bar{h}_1}\frac{\partial \bar{P}}{\partial \xi} + \frac{\bar{v}}{\bar{h}_2}\frac{\partial \bar{P}}{\partial \eta}\right] + \frac{\bar{\mu}}{\bar{C}_p\bar{\rho}\bar{h}_3^2}\left[\left(\frac{\partial \bar{u}}{\partial \zeta}\right)^2 + \left(\frac{\partial \bar{v}}{\partial \zeta}\right)^2\right]$$

$$+ \frac{1}{\bar{C}_p\bar{\rho}\bar{h}_3}\frac{\partial}{\partial \zeta}\left[\frac{\bar{K}}{\bar{h}_3}\frac{\partial \bar{t}}{\partial \zeta}\right]$$

The equations are then nondimensionalized according to the following relations:

$$u = \frac{\bar{u}}{\bar{u}_\infty} \qquad v = \frac{\bar{v}}{\bar{u}_\infty} \qquad w = \frac{\bar{w}}{\bar{u}_\infty}\sqrt{Re}\ \xi^*\ \frac{\bar{\rho}}{\bar{\rho}e}$$

$$\rho = \frac{\bar{\rho}}{\bar{\rho}_\infty} \qquad \mu = \frac{\bar{\mu}}{\bar{\mu}_r} \qquad t = \frac{\bar{t}}{\bar{t}_r}$$

$$P = \frac{\bar{P}}{\bar{\rho}_\infty \bar{u}_\infty^{\,2}} \qquad K = \frac{\bar{C}_p \bar{\mu}}{Pr} \qquad h_1 = \frac{\bar{h}_1}{\bar{L}}$$

$$h_2 = \frac{\bar{h}_2}{\bar{L}} \qquad h_3 = \frac{\bar{h}_3}{\bar{L}} \sqrt{\frac{Re}{\xi^*}}\, \frac{\bar{\rho}}{\bar{\rho}_e}$$

where $Re = \dfrac{\bar{\rho}_\infty \bar{u}_\infty \bar{L}}{\bar{\mu}_r}$, $\bar{\mu}_r = \bar{\mu}(\bar{t}_r)$, and $\bar{t}_r = \dfrac{\bar{u}_\infty^{\,2}}{R}$

Sutherland's viscosity law is used to calculate all viscosities. The normal velocity, w, and normal scale factor, h_3, reduce the equations to a similarity form through the use of the arbitrary function $\xi^*(\xi,\eta)$. Similarity parameters are defined as follows:

$$H = \frac{w}{u_e} \qquad \theta = \frac{t}{t_e} \qquad G = \frac{v}{v_e} \qquad \ell = \frac{\mu}{t}$$

and $\phi = \dfrac{\ell}{2\zeta h_3} \dfrac{\partial}{\partial \zeta} \left(\dfrac{u}{u_e}\right)$.

The equations are then put in a Crocco form by defining a coordinate transformation:

$$\zeta = \sqrt{1 - u/u_e}$$

The resulting equations are:

ξ momentum

$$A_4(1-\zeta^2)^2 + A_5(1-\zeta^2)\, G + A_3 \frac{\zeta\phi H}{\ell} - A_6 G^2 = -A_7\theta - \frac{\phi}{\ell}\frac{\partial}{\partial\zeta}(\phi\zeta)$$

η momentum

$$A_1(1-\zeta^2)\frac{\partial G}{\partial\xi} + A_2 G\frac{\partial G}{\partial\eta} - A_3\frac{\phi H}{\ell}\frac{\partial G}{\partial\zeta} + A_8(1-\zeta^2)G + A_9 G^2 = -A_{10}\theta + \frac{\phi}{\ell}\frac{\partial}{\partial\zeta}\left(\phi\frac{\partial G}{\partial\zeta}\right)$$

Continuity

$$A_1(1-\zeta^2)\frac{\partial}{\partial\xi}\frac{\ell}{\phi} + A_2\frac{\partial}{\partial\eta}\frac{G\ell}{\phi} - A_3\frac{\partial H}{\partial\zeta} + (4A_4 + A_{15})(1-\zeta^2)\frac{\ell}{\phi} + (2A_{17} + A_{16})\frac{\ell G}{\phi} = 0$$

Energy

$$A_1(1-\zeta^2)\frac{\partial\theta}{\partial\xi} + A_2 G\frac{\partial\theta}{\partial\eta} - A_3\frac{\phi H}{\ell}\frac{\partial\theta}{\partial\zeta} = A_{11}(1-\zeta^2)\theta + A_{12}G\theta + A_{13}\zeta^2 + A_{14}\left(\frac{\partial G}{\partial\zeta}\right)^2\left(\frac{\phi}{\ell}\right)^2 + \frac{1}{Pr}\frac{\phi}{\ell}\frac{\partial}{\partial\zeta}\left(\frac{\phi\partial\theta}{\partial\zeta}\right) - \theta A_{18}(1-\zeta^2) - A_{19}G\theta$$

where the A_i coefficients are functions of the edge properties and the geometry. The coefficients are listed in reference 2. The preceding equations have the following boundary conditions, at $\zeta = 1$ (wall):

$$G = 0,\ \theta = \frac{t_w}{t_e} \qquad \frac{\partial\phi}{\partial\zeta} = \left(-A_3H - A_7\frac{\ell}{\phi}\theta - \phi\right)_w$$

at $\zeta = 0$ (outer edge):

$G = 1$, $\theta = 1$, $\phi = 0$

To facilitate numerical solution on a computer, the ξ momentum equation was solved for H. The solution for H was then substituted into the other three equations leading to the following final form for each equation:

$$\frac{\partial^2 \omega}{\partial \zeta^2} + \alpha_1 \frac{\partial \omega}{\partial \zeta} + \alpha_2 \omega + \alpha_3 + \alpha_4 \frac{\partial \omega}{\partial \xi} + \alpha_5 \frac{\partial \omega}{\partial \eta} = 0$$

where $\omega = G$, θ, or ϕ. The coefficients α_i are functions of A_i of the previous set of equations, and of the variables G, θ, and ϕ themselves. An iterative solution of each equation is required since the coefficients are dependent on the dependent variables.

The numerical scheme involves expanding the final form of the governing equations in a series about a centrol point "0" resulting in a finite-difference equation of second-order accuracy. For details of the numerical scheme and how it is handled by the computer, see the report by McGowan and Davis [2].

3. GOVERNING EQUATIONS OF THE AXISYMMETRIC SOLUTION

The governing equations for the boundary layer over the axisymmetric portion of the blunt cone are as follows:

Continuity equation:

$$\frac{\partial}{\partial \bar{x}} \left(\bar{\rho}\ \bar{u}\ \bar{r} \right) + \frac{\partial}{\partial \bar{y}} \left(\bar{\rho}\ \bar{w}\ \bar{r} \right) = 0$$

Momentum equation:

$$\bar{\rho}\bar{u} \frac{\partial \bar{u}}{\partial \bar{x}} + \bar{\rho}\bar{w} \frac{\partial \bar{u}}{\partial \bar{y}} = - \frac{d\bar{P}e}{d\bar{x}} + \frac{\partial}{\partial \bar{y}} \left[\bar{\mu} \frac{\partial \bar{u}}{\partial \bar{y}} \right]$$

Energy equation:

$$\bar{\rho}\bar{u}\,\frac{\partial\bar{H}}{\partial\bar{x}} + \bar{\rho}\bar{w}\,\frac{\partial\bar{H}}{\partial\bar{y}} = \frac{\partial}{\partial\bar{y}}\left[\frac{\bar{\mu}}{Pr}\,\frac{\partial\bar{H}}{\partial\bar{y}} + \bar{\mu}\left(1 - \frac{1}{Pr}\right)\bar{u}\,\frac{\partial\bar{u}}{\partial\bar{y}}\right]$$

These equations are nondimensionalized according to the following relations:

$$x = \frac{\bar{x}}{\bar{a}} \qquad y = \frac{\bar{y}}{\bar{a}}\sqrt{Re} \qquad r = \frac{\bar{r}}{\bar{a}}$$

$$w = \frac{\bar{w}}{\bar{u}_\infty}\sqrt{Re} \qquad H = \frac{\bar{H}}{\bar{u}_\infty^{\,2}}$$

The definitions of variables u, ρ, Re, μ, and μ_r are identical to the three-dimensional case already discussed. However $\bar{t}_r = \frac{\bar{u}_\infty^{\,2}}{C_p}$ in this case. The normal variables y and w are "stretched" by nondimensionalizing them by a quantity of order one in the boundary layer. As in the three-dimensional equations, the viscosity is calculated from Sutherland's Law, and values of the Prandtl number and specific heat are assumed constant (perfect gas).

The governing equations are then put in terms of Levy-Lees variables for convenience of numerical solution. The Levy-Lees transformation is made by introducing the following stream function.

$$\psi(x,y) = (2\xi)^{1/2}\, f(\xi,\zeta)$$

where ξ,ζ are the new transformed coordinates:

$$\xi(x) = \int_0^x \rho_e u_e \mu_e r^2 dx$$

$$\zeta(x,y) = \frac{\rho_e u_e r}{\sqrt{2\xi}} \int_0^y \frac{\rho}{\rho_e}\, dy$$

The resulting equations are:

Continuity

$$2\xi \frac{\partial F}{\partial \xi} + \frac{\partial V}{\partial \zeta} + F = 0$$

Momentum

$$2\xi F \frac{\partial F}{\partial \xi} + V \frac{\partial F}{\partial \zeta} = \frac{2\xi}{u_e} \frac{du_e}{d\xi} \left[\frac{\rho_e}{\rho} - F^2 \right] + \frac{\partial}{\partial \zeta} \left[C \frac{\partial F}{\partial \zeta} \right]$$

Energy

$$2\xi F \frac{\partial G}{\partial \xi} + V \frac{\partial G}{\partial \zeta} = \frac{C}{Pr} \frac{\partial^2 G}{\partial \zeta^2} + \frac{C}{Pr} \frac{\partial G}{\partial \zeta} + \frac{u_e^2}{H_e} \left[\left(1 - \frac{1}{Pr}\right) \left(\frac{\partial C}{\partial \zeta} \frac{\partial F}{\partial \zeta} F \right.\right.$$
$$\left.\left. + C \left(\frac{\partial F}{\partial \zeta}\right)^2 + C \frac{\partial^2 F}{\partial \zeta^2} \right) + CF \frac{\partial F}{\partial \zeta} \frac{\partial}{\partial \zeta} \left(1 - \frac{1}{Pr}\right) \right]$$

where $F = \frac{u}{u_e}$; $G = \frac{H}{H_e}$; $C = \frac{\rho\mu}{\rho_e \mu_e}$

and $V = \frac{2\xi}{\rho_e u_e \mu_e r^2} \left[\frac{\partial \zeta}{\partial x} F + \frac{r \rho v}{\sqrt{2\xi}} \right]$

Boundary conditions at the wall are:

$F = 0$ $\qquad G = \frac{H_w}{H_e}$ $\qquad$ and $C = \frac{(\rho\mu)_w}{(\rho\mu)_e}$

and at the outer edge $F = G = C = 1$.

As in the three-dimensional case, the momentum and energy equations are expressed in the following form for numerical solution:

$$\frac{\partial^2 \omega}{\partial \zeta^2} + \alpha_1 \frac{\partial \omega}{\partial \zeta} + \alpha_2 \omega + \alpha_3 + \alpha_4 \frac{\partial \omega}{\partial \xi} = 0$$

where ω = F or G, and the coefficients α_i are functions of the edge conditions and of ξ, ζ, and ω. The numerical procedure involves replacing the normal derivatives with a Taylor series expansion for varying step sizes in the ζ direction.

The Continuity equation is solved by a numerical integration of:

$$V = V_w - \int_0^{\zeta_e} \left(2\xi \frac{\partial F}{\partial \xi} + F\right) d\zeta$$

after each iteration of the energy and momentum equations. The trapezoidal rule is used to perform the integration.

For details of the numerical scheme used in the axisymmetric part of the solution, see Miner, Anderson, and Lewis [7], and Anderson, and Lewis [13].

4. SURFACE SCALE FACTORS IN THE THREE-DIMENSIONAL SOLUTIONS

Two surface scale factors, h_1, and h_2, are involved in the three-dimensional boundary-layer solutions. They relate the physical lengths along each surface coordinate to the coordinate direction. The scale factors are defined by the following expressions:

$$\bar{h}_1 = \frac{\partial \bar{s}_1}{\partial \xi} \text{ ; and } \bar{h}_2 = \frac{\partial \bar{s}_2}{\partial \eta}$$

where $\bar{s}_1$ and $\bar{s}_2$ are the physical lengths along coordinates ξ, and η respectively.

The scale factors for the case of a sharp cone will be examined first. In cylindrical coordinates (Figure 6a) an infinitesimal arc length is

$$ds^2 = dr^2 + r^2\, d\phi^2 + dz^2 \tag{1}$$

In the present curvilinear coordinate system (Figure 6b), the infinitesimal arc length is

$$ds^2 = d\xi^2 + (\xi \sin\theta_c)^2\, d\eta^2 \tag{2}$$

Referring again to Figure 6a it can be seen that

$$dR^2 = dr^2 + dz^2$$

and

$$\xi \sin\theta_c = r$$

Substituting these expressions into the above equations the following is obtained:

$$ds^2 = dR^2 + r^2\, d\phi^2$$

$$ds^2 = d\xi^2 + r^2\, d\eta^2$$

Then, setting $\xi = R$ we obtain an expression for η:

$$d\eta = d\phi$$

The physical distances are calculated as follows:

$$\bar{s}_1 = \bar{R} = \xi \bar{L}$$

$$\bar{s}_2 = \bar{r}\phi = \xi \bar{L} \sin\theta_c\, \eta$$

Therefore the dimensional scale factors are:

$$\bar{h}_1 = \frac{\partial \bar{s}_1}{\partial \xi} = \bar{L} \qquad \bar{h}_2 = \frac{\partial \bar{s}_2}{\partial \eta} = \xi \sin\theta_c \, \bar{L}$$

and the nondimensional scale factors are:

$$h_1 = \frac{\bar{h}_1}{\bar{L}} = 1 \text{ and } h_2 = \frac{\bar{h}_2}{\bar{L}} = \xi \sin\theta_c$$

The derivatives of the surface scale factors for the sharp cone are

$$\frac{\partial h_1}{\partial \xi} = \frac{\partial h_1}{\partial \eta} = 0$$

and

$$\frac{\partial h_2}{\partial \xi} = \sin\theta_c ; \ \frac{\partial h_2}{\partial \eta} = 0$$

In calculating the scale factors for the case of the blunt cone, two regions of geometry complicate the calculations slightly. The first region of three-dimensional flow is still on the sphere cap, whereas the remainder of the three-dimensional flow is on the conical afterbody. When on the sphere cap, Eq. (2) becomes:

$$ds^2 = d\xi^2 + r_c^{\,2} \, d\eta^2$$

where

$$\bar{r}_c = \bar{r}_c \sin(\xi \bar{L}/\bar{r}_n)$$

$$\bar{L}^2 \xi^2 = r^2 + z^2$$

$$\eta = \phi$$

The scale factors on the sphere cap are derived as follows:

$$h_1 = \frac{\bar{h}_1}{\bar{L}} = \frac{1}{\bar{L}}\frac{\partial(\xi\bar{L})}{\partial\xi} = 1$$

$$h_2 = \frac{\bar{h}_2}{\bar{L}} = \frac{1}{\bar{L}}\frac{\partial}{\partial\eta}\left[\, r_n \sin(\bar{L}\xi/\bar{r}_n)\eta \,\right] = \bar{r}_n \sin(\xi/\bar{r}_n)$$

and their derivatives are

$$\frac{\partial h_1}{\partial\xi} = \frac{\partial h_1}{\partial\eta} = 0$$

$$\frac{\partial h_2}{\partial\xi} = \cos(\xi/\bar{r}_n); \; \frac{\partial h_2}{\partial\eta} = 0$$

On the conical afterbody, Eq. (2) becomes:

$$ds^2 = d\xi^2 + r_c^2\, d\eta^2$$

where

$$\bar{r}_c = \bar{r}_j + \bar{L}\,(\xi - \xi_j)\sin\theta_c$$

$$\bar{r}_j = \bar{r}_n \sin(\xi_j \bar{L}/\bar{r}_n)$$

ξ_j = value of ξ at the sphere cone juncture

$$\eta = \phi$$
$$\bar{L}^2\xi^2 = r^2 + z^2$$

The scale factors on the conical afterbody are derived as follows:

$$h_1 = \frac{\bar{h}_1}{\bar{L}} = \frac{1}{\bar{L}}\frac{\partial(\xi\bar{L})}{\partial\xi} = 1$$

$$\bar{h}_2 = \frac{\bar{h}_2}{\bar{L}} = \frac{1}{\bar{L}} \frac{\partial}{\partial \eta} (\bar{r}_c \eta) = \frac{\bar{r}_c}{\bar{L}}$$

and their derivatives are

$$\frac{\partial h_1}{\partial \xi} = \frac{\partial h_1}{\partial \eta} = 0$$

$$\frac{\partial h_2}{\partial \xi} = \sin\theta_c ; \frac{\partial h_2}{\partial \eta} = 0$$

5. EDGE PROPERTIES

As stated previously the edge properties for the sharp cone come from method of characteristics solutions, and the edge properties for blunt cones come from a combination of the modified inverse method and from the method of characteristics solutions.

Considerable modification to the existing solution methods was necessary in order to introduce nonuniform edge properties into the sharp and blunt cone boundary-layer solutions.

Edge data from the above inviscid solution methods is specified at unequal intervals in the streamwise direction, and at certain equally spaced planes in the transverse direction.

a. Edge Properties for the Axisymmetric Solution

The boundary-layer solution over a blunt cone requires that the pressure distribution be known. The remaining edge properties and their derivatives are determined for a perfect gas. In the axisymmetric boundary-layer solution, pressure is known in the form $\frac{P_e}{P_o}$, where

P_o is the nondimensionalized stagnation pressure expressed as:

$$P_o = \frac{\left[\frac{(\gamma+1)M_\infty^2}{2}\right]^{\frac{\gamma}{\gamma-1}} \left[\frac{\gamma+1}{2\gamma M_\infty^2-(\gamma-1)}\right]^{\frac{1}{\gamma-1}}}{\gamma M_\infty^2}$$

From the stagnation conditions behind the normal shock, a one-dimensional isentropic expansion of a perfect gas proceeds along the body streamline. Reference conditions are based on the flow conditions ahead of the bow shock. Tables of nondimensional edge pressure and velocity are computed from the following expressions:

$$P_e = \frac{\bar{P}_e}{\bar{\rho}_\infty \bar{u}_\infty^2} = \frac{\bar{P}_o}{\bar{\rho}_\infty \bar{u}_\infty^2} \frac{P_e}{\bar{P}_o}$$

$$u_e = \frac{\bar{u}_e}{\bar{u}_\infty} = 2(T_o - T_e)$$

where

$$T_o = \frac{\bar{T}_o}{\bar{T}_{ref}} = \frac{\bar{T}_o \bar{C}_p}{\bar{u}_\infty^2} = \frac{\bar{T}_o}{(\gamma-1)M_\infty^2 \bar{T}_\infty}$$

$$T_e = \frac{T_o}{1+\frac{\gamma-1}{2} M_L^2}$$

and

$$M_L = \left[\frac{2}{\gamma-1}\left(\frac{P_e}{P_o}\right)^{\frac{-\gamma}{\gamma-1}} - 1\right]^{\frac{1}{2}}$$

The values of P_e and u_e are interpolated at each solution point. The value of du_e/dx is obtained numerically. The values of T_e, ρ_e, and μ_e are calculated at each solution point according to the following expressions:

$$T_e = T_o - u_e^{2}/2$$

$$\rho_e = \frac{\gamma}{\gamma-1}\,\frac{P_e}{T_e}$$

$$\mu_e = \frac{1+C'}{T_e+C'}\left(T_e\right)^{3/2}$$

The pressure derivative $\frac{dP_e}{dx}$ is calculated as:

$$\frac{dP_e}{dx} = -\rho_e u_e \frac{du_e}{dx}$$

For the purpose of matching the axisymmetric solution to the three-dimensional solution along a body fixed plane, a table of edge temperatures was added to the axisymmetric solution. This made possible the numerical calculation of $\frac{dT_e}{dx}$ as part of the required initial data for the three-dimensional boundary-layer solution.

b. Edge Properties for the Three-Dimensional Solution

Since the three-dimensional solution is used only in regions of supersonic flow, all edge properties come from a method of characteristics solution. The method of characteristics solution may specify as many as ten solution planes around the cone. In solving the boundary layer on a cone at angle of attack, it may be desirable to have more or less than ten solution planes around the cone. For maximum versatility and minimum data storage, the edge data from the method of characteristics are converted to Fourier coefficients at each of a number of streamwise stations along the cone. This procedure allows edge data to be recreated at any plane and streamwise station from a limited amount of stored data.

The series used to calculate the Fourier coefficients is based on the fact that the data come from equally spaced meridional planes. The values of pressure, density, velocity, and their circumferential derivatives are reconstructed from a Fourier cosine series;

$$u_K = \sum_{n=0}^{L-1} a_n \cos n\Phi_K$$

The coefficients a_n are calculated by the following equation:

$$a_n = \frac{2}{L-1}\left[\frac{(u_1 + u_L \cos(n-1)\pi)}{2} + \sum_{K=2}^{L-1} u_K \cos(n-1)\Phi_K\right]$$

$$n = 1, 2, 3, \ldots, L$$

where L is the number of meridional planes, u_K is the function P_e, ρ_e, or v_e and

$$\phi_K = \pi \frac{K-1}{L-1}, \ (K = 1, 2, 3, \ldots, L)$$

Circumferential derivatives are calculated from the derivative of the series:

$$\frac{\partial u_K}{\partial \Phi} = \sum_{n=1}^{L-1} -na_n \sin n\Phi_K$$

The Fourier sine series is used to calculate the cross flow angle:

$$\phi_K = \sum_{n=1}^{L-1} b_n \sin n\Phi_K$$

and its derivative:

$$\frac{\partial \phi_K}{\partial \Phi} = \sum_{n=1}^{L-1} nb_n \cos n\Phi_K$$

The coefficients b_n are found from the expression:

$$b_n = \frac{2}{L-1} \sum_{K=2}^{L-1} \phi_K \sin n\Phi_K \qquad (n = 1, 2, 3, \ldots, L-1)$$

Once the pressure, density, velocity, and cross flow angle are known the required inviscid edge data are found:

longitudinal velocity, $u_e = V_e \cos\phi$

cross flow velocity, $v_e = V_e \sin\phi$

temperature, $t_e = (KP_e{}^{\gamma-1})^{1/\gamma}$ where $K = \frac{P_e}{\rho_e{}^{\gamma}}$ at the windward streamline

$$\frac{\partial u_e}{\partial \eta} = v_e$$

$$\frac{\partial t_e}{\partial \eta} = \frac{\gamma-1}{\gamma} \frac{t_e}{P_e} \frac{\partial P_e}{\partial \eta}$$

$$\frac{\partial v_e}{\partial \eta} = \frac{\partial V_e}{\partial \Phi} \sin\phi + V_e \cos\phi \, \frac{\partial \phi}{\partial \Phi}$$

Derivatives of P_e, u_e, v_e, and t_e with respect to ξ are obtained from a two-point difference method.

For the case of a sharp cone the edge properties near the sharp tip are taken from a standard sharp cone solution which is used as initial data for the method of characteristics solution for the remainder of the sharp cone.

6. INITIAL DATA FOR THE THREE-DIMENSIONAL BOUNDARY LAYER SOLUTION OVER A BLUNT CONE

The axisymmetric and three-dimensional boundary-layer solutions meet along a body-fixed plane which at zero angle of attack terminates the sphere cap, and at non-zero angle of attack terminates the wedge section.

The three-dimensional solution requires initial data profiles at evenly spaced points in ζ; however, the axisymmetric solution profiles are not specified at evenly spaced points in ζ. Six profiles are required as initial data for the three-dimensional solution, viz., shear parameter, temperature, cross-flow velocity, and their respective normal derivatives.

The temperature distribution and its normal derivative already exist in the axisymmetric solution. The shear parameter and cross-flow velocity distributions and their derivatives are created from the axisymmetric solution. Initial data profiles are created for each of the equally spaced planes in the boundary-layer solution. Therefore, it must be possible to specify the solution point locations along the leeward plane of the wedge section such that the points rotate into an equally spaced pattern along the body-fixed plane. Referring to Figure 7, it is seen that equally spaced points in ϕ may be translated into points on the leeward plane by the following expression:

$$S_w = r_n \ \mathrm{Cos}^{-1}(\sin\gamma\cos\alpha - \cos\gamma\sin\alpha\cos\phi)$$

where $\gamma = \mathrm{Cos}^{-1} r_w$, and r_w is the local radius of the body-fixed plane.

To obtain the equally spaced data in the normal direction, the longitudinal velocity profile of the three-dimensional solution is employed:

$$\left.\frac{u}{u_e}\right|_{3-D} = 1 - \zeta^2$$

giving a value of u/u_e for each equally spaced point in ζ. At a point where $u/u_{e_{3-D}}$ corresponds to u/u_e in the axisymmetric velocity profile, values of θ, $\left.\frac{\partial\theta}{\partial\zeta}\right|_{AXI}$, $\left.\frac{\partial F}{\partial\zeta}\right|_{AXI}$, and $\left.\frac{\partial y}{\partial\zeta}\right|_{AXI}$ corresponding to $\left.\frac{u}{u_e}\right|_{3-D}$ are found by interpolation in their axisymmetric solution profiles respectively. The double interpolation is done by using a three-point Lagrangian interpolating formula.

The cross flow velocity profile is obtained from the $\left.\frac{u}{u_e}\right|_{3-D}$ profile and the corresponding edge crossflow angles:

$$\frac{v}{v_e} = \left[\frac{u}{u_e}\; u_e\right]_{3\text{-}D} \left[\frac{\sin \phi_e}{u_{e_{AXI}} \sin \phi_e}\right]$$

$$\frac{v}{v_e} = \frac{u}{u_e}$$

Thus the cross-flow velocity profile will be taken equal to the longitudinal velocity profile as an initial guess to start the three-dimensional solution.

The normal coordinate transformation has put the shear parameter in simpler terms:

$$\phi = \frac{\ell}{2\zeta h_3} \frac{\partial}{\partial \zeta} \left(\frac{u}{u_e}\right) = \frac{-\ell}{h_3}$$

From this simple expression the shear parameter profile may be calculated from axisymmetric solution profile data:

$$\phi = \frac{-\ell}{h_3} = \frac{-\bar{\mu}}{\bar{\mu}_{ref}} \frac{\bar{t}_{ref}}{\bar{t}} \frac{\bar{L}\xi^* \bar{\rho}_e}{\bar{h}_3\sqrt{Re}\;\bar{\rho}}$$

where

$$\frac{\bar{\rho}_e}{\bar{\rho}} = \theta, \; \bar{h}_3 = \left.\frac{\partial \bar{y}}{\partial \zeta}\right|_{3\text{-}D}$$

Therefore $\phi = \dfrac{-\bar{\mu}}{\bar{\mu}_{ref}} \dfrac{\bar{L}\xi^*}{t_e\;\sqrt{Re}} \left[\left.\dfrac{\partial \bar{y}}{\partial \zeta}\right|_{AXI} \dfrac{\partial \zeta}{\partial \zeta}\begin{matrix}AXI\\3\text{-}D\end{matrix}\right]^{-1}$

As in the case of the shear parameter, derivatives with respect to the axisymmetric normal coordinate must be converted to derivatives with respect to the three-dimensional normal coordinate. The conversion derivative is calculated as follows:

$$\zeta_{3-D} = \sqrt{1 - F}$$

Therefore $\dfrac{\partial \zeta_{AXI}}{\partial \zeta_{3-D}} = \dfrac{-2(1-F)^{1/2}}{\partial F/\partial \zeta_{AXI}}$, where the values of F and $\partial F/\partial \zeta_{AXI}$ are obtained by the double interpolation in the axisymmetric solution profiles described previously.

Edge data along the body-fixed plane are obtained from the first station of the method of characteristics solution. In the inviscid program the edge data along the leeward plane in the wedge section are rotated to set up initial inviscid profiles for the method of characteristics solution. Therefore the first method of characteristics solution is along the body-fixed plane terminating the wedge section, or in the zero angle of attack case, the body-fixed plane terminating the sphere cap.

7. BOUNDARY-LAYER PARAMETERS

Skin-friction coefficients, heat-transfer rates, heat-transfer coefficients, boundary layer thickness, displacement thickness, and Stanton numbers are calculated in both the axisymmetric and three-dimensional solutions. The parameters as derived from the axisymmetric solution will be considered first. Parameters will be defined in terms of dimensional variables, nondimensional variables, and finally, transformed variables.

a. Boundary-Layer Parameters for the Axisymmetric Solution

The heat transfer in dimensional variables is

$$\bar{q}_w = -K_w \frac{\partial \bar{T}}{\partial \bar{y}}\bigg|_w = \frac{-\bar{\mu}_w}{Pr}\frac{\partial \bar{H}}{\partial \bar{y}}\bigg|_w$$

In nondimensional form:

$$q_w = \frac{\bar{q}_w \sqrt{Re}}{\bar{\rho}_\infty \bar{u}_\infty{}^3} = \frac{-\mu_w \, He}{Pr}\frac{\partial H}{\partial y}\bigg|_w$$

In Levy-Lees variables:

$$q_w = \frac{-\mu_e C_w H_e}{Pr}\frac{\rho_e u_e r}{\sqrt{2\xi}}\frac{\partial H}{\partial \zeta}\bigg|_w$$

The dimensional heat transfer rate is found from

$$\bar{q}_w = \frac{q_w \bar{\rho}_\infty \bar{u}_\infty{}^3}{\sqrt{Re}\,(778)}\ \frac{Btu}{ft^2\text{-sec}}$$

The heat-transfer coefficient based on free-stream conditions is defined as:

$$Ch_\infty = \frac{\bar{q}_w}{\bar{\rho}_\infty \bar{u}_\infty (\bar{H}_{aw}-\bar{H}_w)} .$$

Therefore

$$Ch_\infty = \frac{q_w}{\sqrt{Re}\,(H_{aw}-H_w)}$$

The heat-transfer coefficient based on edge conditions is found from:

$$Ch_e = \frac{Ch_\infty}{\rho_e u_e}$$

The skin-friction coefficient based on free-stream conditions is

$$C_{f_\infty} = \frac{2\bar{\tau}_w}{\bar{\rho}_\infty \bar{u}_\infty^{\,2}}$$

In Levy-Lees variables

$$C_{f_\infty} = \frac{2\mu_e u_e^2 C_w \rho_e r}{\sqrt{2\xi Re}} \left.\frac{\partial F}{\partial \zeta}\right|_w$$

The skin-friction coefficient based on edge conditions is expressed as:

$$C_{f_e} = \frac{2\bar{\tau}_w}{\bar{\rho}_e \bar{u}_e^{\,2}}$$

which may be obtained from:

$$C_{f_e} = \frac{C_{f_\infty}}{\rho_e u_e^{\,2}}$$

The Stanton number based on free-stream conditions is defined as:

$$St_\infty = \frac{\bar{q}_w}{\bar{\rho}_\infty \bar{u}_\infty (\bar{H}_e - \bar{H}_w)}$$

Therefore;

$$St_\infty = \frac{-q_w}{\sqrt{Re}(H_e - H_w)}$$

Based on edge conditions the Stanton number is

$$St_e = \frac{-q_w}{\bar{\rho}_e \bar{u}_e (\bar{H}_e - \bar{H}_w)}$$

which may be obtained from

$$St_e = \frac{St_\infty}{\rho_e u_e}$$

The displacement thickness for a two-dimensional flow is defined as:

$$\bar{\delta}^* = \int_0^{\bar{y}_e} \left[1 - \frac{\bar{\rho}\,\bar{u}}{\rho_e u_e}\right] d\bar{y}$$

In nondimensional variables it is:

$$\frac{\bar{\delta}^*}{\bar{a}} = \frac{1}{\sqrt{Re}} \int_0^{y} \left[1 - \frac{\rho\, u}{\rho_e u_e}\right] dy$$

and in transformed variables:

$$\frac{\bar{\delta}^*}{\bar{a}} = \sqrt{\frac{2\xi}{Re}}\, \frac{1}{\rho_e u_e r} \int_0^{\eta_e} \left[\frac{\rho_e}{\rho} - F\right] d\eta$$

The axisymmetric compressible displacement thickness is approximated from the two-dimensional value as follows:

$$\frac{\bar{\delta}^*_{AXI}}{\bar{a}} = r \left[\left(1 + \frac{2\bar{\delta}^*/\bar{a}}{r}\right)^{1/2} - 1\right]$$

In both the axisymmetric and three-dimensional solutions, the boundary-layer thickness is assumed to be the value of $\bar{y}$ at the point where u/u_e is equal to 0.995. In both cases it is determined by interpolation in the velocity profile.

b. Boundary-Layer Parameters for the Three-Dimensional Solution

Parameters from the three-dimensional solution will now be presented in the same way they were in the axisymmetric case. The heat-transfer rate is defined as follows:

$$\bar{q}_w = -K_w \frac{\partial \bar{T}}{\partial \bar{y}}\bigg|_w$$

In nondimensional form the heat transfer rate is

$$q_w = \frac{\bar{q}_w}{\bar{\rho}_\infty \bar{u}_\infty^{\,3}}$$

and in transformed variables it is

$$q_w = \frac{\phi_w t_e^{\,2} \gamma}{\xi^* Pr(\gamma-1)} \frac{\partial \theta}{\partial \zeta}\bigg|_w \frac{1}{\sqrt{Re}}$$

The dimensional heat transfer rate is found from

$$\bar{q}_w = q_w \frac{\bar{\rho}_\infty \bar{u}_\infty^{\,3}}{778} \frac{\text{Btu}}{\text{ft}^2\text{-sec}}$$

The heat-transfer coefficient based on free-stream conditions is defined as follows:

$$Ch_\infty = \frac{-\bar{q}_w}{\bar{\rho}_\infty \bar{u}_\infty \bar{C}_p (\bar{t}_{aw} - \bar{t}_w)}$$

and therefore

$$Ch_\infty = \frac{-q_w}{C_p(t_{aw}-t_w)}$$

Based on edge conditions, the heat transfer coefficient is

$$Ch_e = \frac{-q_w}{\bar{\rho}_e \bar{u}_e \bar{C}_p(\bar{t}_{aw}-\bar{t}_w)}$$

and therefore

$$Ch_e = \frac{-q_w}{\rho_e u_e C_p(t_{aw}-t_w)}$$

The skin friction coefficient is broken into two components, longitudinal and transverse. The skin-friction coefficients based on free-stream conditions are defined as follows:

$$\text{longitudinal:} \quad C_{f_{\xi_\infty}} = \frac{2\bar{\tau}_{w_\xi}}{\bar{\rho}_\infty \bar{u}_\infty^2}$$

$$\text{transverse:} \quad C_{f_{\eta_\infty}} = \frac{2\bar{\tau}_{w_\eta}}{\bar{\rho}_\infty \bar{u}_\infty^2}$$

In transformed variables the skin-friction coefficients become

$$\text{longitudinal:} \quad C_{f_{\xi_\infty}} = \frac{4t_e \phi_w u_e}{\xi^* \sqrt{Re}}$$

$$\text{transverse:} \quad C_{f_{\eta_\infty}} = \frac{-2t_e \phi_w v_e}{\xi^* \sqrt{Re}} \frac{\partial G}{\partial \zeta}\bigg|_w$$

The skin-friction coefficients based on edge conditions are determined from the following general formula:

$$C_{f_e} = \frac{C_{f_\infty}}{\rho_e u_e^{2}}$$

The Stanton number based on free-stream conditions is defined as:

$$St_\infty = \frac{-\bar{q}_w}{\bar{\rho}_\infty \bar{u}_\infty \bar{C}_p (\bar{t}_o - \bar{t}_w)}$$

and therefore

$$St_\infty = \frac{-q_w}{C_p (t_o - t_w)}$$

Based on edge conditions, the Stanton number is

$$St_e = \frac{-\bar{q}_w}{\bar{\rho}_e \bar{u}_e \bar{C}_p (\bar{t}_o - \bar{t}_w)}$$

and therefore

$$St_e = \frac{-q_w}{\rho_e u_e C_p (t_o - t_w)}$$

The displacement thickness in the three-dimensional boundary-layer solution is defined as follows:

$$\bar{\delta}^* = \int_0^\infty \left[1 - \frac{\rho\, u}{\rho_e u_e} \right] d\bar{y}$$

The transformed displacement thickness is then

$$\delta^* = \int_0^1 (\theta - F) \frac{\ell}{\phi}\, d\zeta \frac{\bar{L}\xi^*}{\sqrt{Re}}$$

The boundary-layer normal distance profile is determined by the following integral:

$$\bar{y} = \int_1^{\zeta} \bar{h}_3 \, d\zeta$$

which in transformed variables is

$$\bar{y} = - \int_1^{\zeta} \frac{\ell}{\phi} \theta \, d\zeta \frac{\bar{L}\xi^*}{\sqrt{Re}}$$

SECTION III

RESULTS AND DISCUSSION

Results are presented in two parts. Results for a sharp cone in shear flow are presented first, followed by results obtained for a spherically blunted cone in axisymmetric wake flow. Plotted results are presented in Figures 8 thru 71.

1. SHARP-CONE RESULTS

Sharp-cone results are presented in Figures 8 thru 32. The cases investigated are for a 20 degrees half-angle sharp cone in two-dimensional shear flow at 2, 6, 10, and 14 degrees angles of attack. The velocity defect parameter, $\omega = 0.05$, and the $M_\infty = 3$. The free-stream temperature is 58.2^oR, and the wall to stagnation temperature ratio is 0.40. A perfect gas is assumed and the ratio of specific heats is 1.4.

All shear-flow results are in terms of normalized coefficients which have been normalized to the values for the same sharp cone at zero angle of attack in a uniform Mach 3 free stream.

Figure 8 shows the dimensional wall heat-transfer rate for uniform Mach 10.6 laminar flow over a 15^o half-angle cone at 5^o angle of attack. Windward streamline values are plotted from the experiments of Cleary [8] versus the prediction of the three-dimensional boundary-layer solution before modification for nonuniform flow.

The good agreement obtained in this case establishes the McGowan-Davis three-dimensional program as an acceptable solution method for modification to the nonuniform flow case.

In Figure 9 a 10^0 angle of attack shear flow case has been converted to uniform flow to test the modified three-dimensional program against the unmodified uniform flow program as developed by McGowan and Davis. Transformed values of the longitudinal skin-friction and heat-transfer coefficients are plotted around the cone. Since this is a conical flow case, the plotted solution is valid all along the cone. It is seen that, for nonuniform flows, the present method actually obtains a smoother solution than the original three-dimensional program. Excellent agreement has been obtained between the two methods. The smoother solution from the nonuniform flow program can be attributed to the use of Fourier series to expand the edge properties around the cone.

The numerical procedure used to solve the three-dimensional boundary-layer equations is particularly sensitive to how smooth the cross-flow velocity derivative is around the cone at each streamwise station. The original McGowan and Davis program computed this derivative numerically, and smoothed it numerically at least twice. The present method obtains this derivative analytically through the use of Fourier series and is not smoothed further. The two methods are compared in Figure 10 for the same uniform flow case plotted in Figure 9. The curve for the present method exhibits a flat curvature near the leeward and windward planes, as it should. It has a more pronounced curvature throughout the entire range than does the McGowan-Davis curve; however, the values are in reasonable agreement.

Figures 11 thru 24 are plots of the various edge properties used in the solution of the four shear flow cases. It is seen in Figures 11 and 13 that there is a sizable streamwise pressure gradient for the windward streamline for all shear flow cases, and that the gradient is more pronounced with increasing angle of attack. In Figure 14 it is shown that as far as S = 2 the pressure increases in the streamwise direction on all streamlines between $\phi = 0^o$ and $\phi = 90^o$. Between $\phi = 90^o$ and $\phi = 120^o$ the pressure for all cases begins to fall. Looking at figures 12 and 16 it can be seen that a strong favorable transverse pressure gradient exists around the cone as far as S = 2. The gradient is increased as the angle of attack is increased; however, in all cases the peak gradient was near the $\phi = 60^o$ streamline. Figure 16 shows the highest values of $\partial^2 P_e/\partial\eta^2$ to be near the windward streamline. Figure 15 establishes the trend of the transverse pressure gradient to be consistent along the entire length of the cone.

The edge temperature, as shown in Figures 17 and 18, follows the same trend established in the pressure curves for both streamwise and transverse directions. These trends are insured by the isentropic relations on the inviscid surface of the cone. In response to the streamwise adverse edge pressure gradient, the longitudinal edge velocity component shows a decrease in the streamwise direction for all shear flow cases. A corresponding increase in the longitudinal component of the edge velocity takes place around the cone (Figure 20). Figures 21 and 22 show an increasing edge cross-flow velocity in both the streamwise and transverse directions. Figure 22 shows the cross-flow edge velocity to be rapidly increasing near the windward streamline, and Figure 24 shows the values of $\partial v_e/\partial \eta$ to be greatest at the windward streamline where v_e is zero. Figure 23 establishes the existence of strong transverse cross flow edge velocity gradients all along the windward streamline of the cone and increasing in the streamwise direction. Of course, the effect of cross flow increases with increasing angle of attack.

In Figures 25 thru 27 the present method is compared to the method of Bordner and Davis [1]. Normalized heat-transfer and skin-friction coefficients are plotted for the windward streamline of a sharp cone at 10^0 angle of attack. Reasonably good agreement is shown in the comparison (Figure 25). The present method appears to give a smoother solution for the skin-friction coefficient in at least one region of the cone. In Figures 26 and 27 results in the transverse plane from both methods are compared, first for the normalized heat-transfer coefficient (Figure 26) and then for the normalized skin-friction coefficient (Figure 27). Nearly identical results are obtained by the two methods for two values of S.

In Figures 28 thru 32 the remainder of the sharp cone results in shear flow are presented. Streamwise plots of the normalized skin-friction and heat-transfer coefficients are presented in Figures 28 and 29. It is seen that for all angles of attack both the heat transfer and skin friction depart from the corresponding conical flow values (represented in all applicable plots by dashed lines). This occurs even in the presence of the adverse axial pressure gradient previously discussed. A physical explanation for this somewhat unexpected result can be found in the rapidly decreasing pressure near the windward streamline as the solution marches around the cone (Figure 16). This favorable pressure gradient causes a positive transverse cross flow velocity gradient, $\partial v_e/\partial \eta$, to develop, tending to move fluid away from the windward plane toward the leeward plane. This effect offsets the usual boundary-layer thickening which accompanies an adverse axial pressure gradient, and hence produces higher values of skin friction and heat transfer. It can also be seen in Figures 28 and 29 that the rate of increase of the coefficients with S increases with increasing angle of attack. This is to be expected since the higher angles of attack bring on more pronounced cross flow effects, including a much more pronounced decrease of pressure around the cone.

Plots of the normalized skin-friction and heat-transfer coefficients around the cone at S = 0, 1 and 2 are presented in Figures 30 thru 32 for $\alpha = 2^{o}$, 6^{o}, and 14^{o}. It can be seen that the skin friction and heat transfer decrease around the cone in all cases. The skin-friction coefficient curves exhibit very little difference from station to station even though the pressure profiles are significantly different at those stations. A possible explanation may be found again in the migration of fluid away from the windward plane in response to the favorable transverse pressure gradient. As the solution moves downstream the boundary layer around the cone tends to become thinner due to more favorable transverse pressure gradients; however, the increasing transverse pressure gradients invite added migration of fluid from the windward plane where pressure is building at the same time. The added fluid escaping the windward plane tends to cancel the effect of the increased favorable transverse pressure gradient; hence predicting nearly constant skin-friction curves around the cone as one moves downstream. This effect is least noticeable at 2^0 angle of attack where cross-flow effects are a minimum. The effect is very pronounced at 14^0 angle of attack. In all cases, increasing the angle of attack increases the skin-friction and heat-transfer coefficients at all circumferential points. Each of the circumferential curves goes through an inflection point corresponding to the maximum transverse pressure gradient which in turn corresponds to an inflection point in the transverse pressure curve. Past the inflection point the coefficient curves reverse their station to station trend. For instance, where the heat transfer for S = 2, at a particular angle of attack, was the highest, relative to S = 0 and 1, before the inflection point, it will be the lowest heat-transfer coefficient value after the inflection point. Before the inflection point the pressure at S = 2 is higher and decreasing faster than the pressure at S = 0 or 1. After the inflection point the favorable transverse pressure gradient decreases but not fast enough to offset the effect of the initial high gradient, and the pressure at S = 2 falls below the pressures at S = 0 and 1. The effect is to reverse the coefficient trends as noted.

2. BLUNT-CONE RESULTS

Blunt-cone results are presented in Figures 33 thru 71. The cases investigated are for a 15° half-angle, spherically blunted cone in axisymmetric wake flow at $\alpha = 0^{\circ}$, 5°, and 10°. The velocity defect parameter A = 0.015 in all cases. The wake parameter B was varied from 0.1 to 0.2 to show the effects of the width of the wake on the flows. Uniform flow results have been included in each figure for comparison with the wake flow data. The thermodynamic data matches the conditions used by Cleary in his uniform flow experiments for $Re_{\infty} = 0.4 \times 10^{6}$ per foot. All Re_{∞} appearing in the figures are per foot quantities. The M_{∞} for these cases is 10.6, the total temperature is $2000^{\circ}R$, and the total pressure is 400 psia. These conditions correspond to a free-stream temperature of $85.2^{\circ}R$ and a free-stream pressure of 0.006383 psf.

Figures 33 and 34 show a Mach 10.6 uniform free-stream flow over a 15° half-angle cone at three angles of attack. Windward streamline values of the nondimensional heat transfer rate are plotted from the from the experiments of Cleary [8] versus the prediction of the blunt cone boundary-layer solution developed in this study (Figure 33). For this particular case experimental data are available only at 0^{o} and 5^{o} angles of attack. The present method is seen to be in very good agreement with the windward streamline data of Cleary's experiment. Figure 33 also shows the effect of angle of attack on the nondimensional heat-transfer rate. The heat transfer increases very significantly with increasing angle of attack; however, the trend of the curves is the same for all angles of attack. In Figure 34 circumferential heat-transfer data from Cleary's experiment at 5^{o} angle of attack are compared to the present prediction method at three values of S/R_n. Reasonable agreement is obtained for each station. Significant exceptions are the experimental values near the leeward streamline for S/R_n of 2.84 and 5.58. This figure also shows the decreasing heat-transfer rates as the solution marches around the cone from the windward to leeward plane. The figure also shows that the heat-transfer rate decreased downstream on all streamlines.

Further experimental correlation is given in Figure 36. A Mach 5 uniform flow over a 9^{o} half-angle cone at 0^{o} and 5^{o} angles of attack is plotted. The experimental data are from an experiment by Widhopf [9]. Very good agreement is obtained all along the windward streamline for the zero angle of attack case. The 5^{o} angle of attack experiment of Widhopf exhibits transition to turbulence at approximately an $S/R_n = 2$, and therefore is not a valid comparison. Experimental data in the laminar region for the 5^0 angle of attack case shows reasonable agreement with the results of the present method. The pressure distributions for the Widhopf cases are given in Figure 35.

The comparison of the results of the present method with experimental data establishes the method as a valid tool for prediction of the boundary-layer flows in uniform flow. It is, therefore, assumed that the method is equally valid for nonuniform flow cases such as the axisymmetric wake flows of this study. The assumption is necessary since neither experimental nor numerical data exist for blunt cones at angle of attack to nonuniform free streams. The remaining results, for blunt cones in axisymmetric wake flow, are grouped by angle of attack.

Figures 37 thru 39 show results for a blunt cone in wake flow at zero angle of attack. All plotted data are along the windward streamline. In each figure uniform flow is plotted along with two wake flows. Figure 37 shows the pressure distributions for the three flow cases. It is seen that much more severe adverse pressure gradients exist along the windward streamline in wake flow. As in the uniform flow cases, the adverse pressure gradient for nonuniform flow cases results from the over-expansion and recompression of the flow as it travels around the spherical nose. Decreasing the width of the wake (increasing B) also causes a greater pressure gradient. From Figures 38 and 39, there is very little effect of the wake flow on either the skin friction or heat transfer before traveling a distance of 2 nose radii downstream. This is in response to the pressure curves as shown in Figure 37. If one were to blow up the scale in the nose region, he would see definite pressure increases at all points for wake flows; however, the changes are small near the nose since all of the solutions begin with the same nose conditions. Inviscid solutions are obtained by keeping nose conditions constant and changing only the wake parameters.

The streamwise increase in heat transfer is probably due to the same physical process which caused this effect for sharp cones. In fact, as the blunt cone solution proceeds downstream, it asymptotically approaches the sharp cone solution for the same conditions; hence we may notice similar behavior as the two solutions march downstream. This effect can be seen by comparing the trends of the solid line of Figure 47 with the solid line of Figure 8 far downstream. Dividing $\bar{q}_w$ of Figure 8 by $\bar{q}_0$ (11.2 Btu/ft^{2}sec), it is seen that the solutions for sharp and blunt cone cases approach identical values far downstream. The skin-friction coefficient (Figure 39) shows an increase over the uniform flow values for wake flow cases and a more severe departure when the width of the wake is decreased. The increase of skin friction is reversed far downstream. The boundary-layer thickening along the windward streamline overcomes the effect of the cross flow as the wake flow solutions proceed far downstream. This behavior is not the case for the heat transfer because the normal temperature gradient is still increasing in the thickening boundary layer. The peak value of skin friction occurs at the same location for all wake flow and uniform flow cases. Small increases are evident in the value of the peak friction which occurs in each case near the sphere-cone juncture ($S/R_n = 1.3$).

Figures 40 thru 58 present the results obtained for the same blunt cone in wake flow at 5^0 angle of attack. Figure 40 is analogous to Figure 37.

Figures 41 thru 43 show the rising and falling of the favorable transverse pressure gradient around the cone at three downstream stations. Note the different scales used in the figures. The uniform flow values show very little change from station to station as do the wake flow values. As the solution goes from an $S/R_n = 2.84$ to 7.8, the wake flow values of the pressure gradient increase three fold ($B = .2$). The values for the wider wake more than double in the same range of S/R_n. As the solution moves down the cone, the tendency is for the transverse pressure gradient to rise faster (become more negative) on the windward side than it drops on the leeward side thus causing the curves at $S/R_n = 5.58$ and 7.8 to be skewed to the left.

In Figures 44 thru 46 the response of the edge cross-flow velocity to the previously discussed transverse pressure gradient variation is seen. Where the difference in pressure gradients is smallest ($S/R_n = 2.84$), the difference in cross-flow velocity gradients is smallest. The greatest difference is shown to be where the greatest pressure gradient difference was found ($S/R_n = 7.8$). These curves exhibit the same behavior on either side of an inflection point as was observed in the sharp cone results.

The behavior of the nondimensional heat transfer rate for the $\alpha = 5^o$ case on the windward streamline (Figure 47) exhibits trends identical to those discussed for Figure 38. The values for $\alpha = 5^o$ are substantially higher than are those for the zero angle of attack case and the same is true for the streamwise gradients of the heat transfer. The effect of downstream position on the nondimensional heating rate is traced through Figures 48 thru 51. The curves in Figure 48 show the heat transfer around the cone at $S/R_n = 1.41$ which is just past the sphere-cone juncture and still in a region of sharply dropping windward streamline pressures. The results plotted in Figures 49 and 50 "straddle" the minimums of the heat transfer as seen in Figure 47, leading to nearly identical curves at the two values of S/R_n. It can be seen that the trend established by the uniform flow results at each station has not been changed by the introduction of free-stream nonuniformities; however, the nondimensional heating rates for the wake flow cases are higher for all streamlines around the cone at each station. Decreasing the width of the wake causes further increase in the heating rate over the uniform flow values. Looking again at Figures 48 thru 51, it is seen that the leeward side values of the heating-rate distribution fall as S/R_n increases. This is true for both uniform and wake flows and is due to the thickening of the boundary layer on the leeward side of the cone as S/R_n increases. This in turn is a response to the build-up of fluid migrating from the windward plane to the leeward side of the cone.

Figures 52 thru 55 present the longitudinal skin friction coefficient. In Figure 52 the longitudinal skin friction distribution exhibits a behavior analogous to the zero angle of attack results (Figure 39). The peak values are nearly identical, but the downstream drop in the coefficients is not as great. The circumferential curves of longitudinal skin friction follow the general trend set by the circumferential heat transfer curves. As in the heat-transfer case, the skin friction falls to lower values on the leeward side as S/R_n increases. This is true for each of the flows represented. In keeping with the windward streamline inflection point, a definite change in the behavior can be seen between the curves at $S/R_n = 2.84$ and $S/R_n = 5.58$. The same physical explanation may be applied to the skin friction curves in the area of the leeward plane as was applied to the heat-transfer curves in that region.

The transverse skin-friction coefficient is shown around the cone at three different values of S/R_n in Figures 56 thru 58. For each of the flows represented, the transverse skin-friction coefficients show very large increases as S/R_n increases for all streamlines. At each station the transverse skin friction curves are completely analogous with the transverse pressure-gradient curves in Figures 41 thru 43.

The maximums, leftward skews, rises and falls all correspond to the pressure-gradient curves at the same station. Again, the effect of the nonuniform flow has been to raise the skin friction at all points, and decreasing the width of the wake causes further increases in skin friction.

Results are presented in Figures 59 thru 71 for the same spherically blunted cone in wake flow $\alpha = 10^{o}$ where every trend noted in the 5^{o} angle of attack case can be seen to occur at this angle of attack. It will be noted, however, that all of the trends and results of the 10^{o} angle of attack case are far more pronounced than they were in the 5^{o} case. In comparing the 5^{o} and 10^{o} angle of attack cases, it can be seen that the effect of flow nonuniformity is greater for the higher angle of attack flow. For instance, the difference between the peak uniform flow transverse pressure gradient at $S/R_n = 2.84$ for the wake flow value of $B = 0.1$ is approximately 0.014 at 10^{o} angle of attack. The corresponding difference in the 5^{o} angle of attack case is one-half the 10^{o} value (see Figures 41 and 60). The same effect is readily obvious in the transverse skin-friction curves of Figures 56 and 70.

The effects of free-stream nonuniformity on boundary-layer separation have not been studied in detail. No evidence of separation was found for blunt cones in uniform and wake flows at $\alpha = 0^{o}$ or for a blunt cone in uniform flow at $\alpha = 5^{o}$. For all cases at $\alpha = 10^{o}$, and for wake flow cases at $\alpha = 5^{o}$ there was a significant decrease in the length of cone which was solved. Solutions of these cases terminated due to a negative shear parameter at the wall. In the longitudinal plane, the onset of separation occurred sooner (fewer nose radii) for smaller width wakes and for higher angles of attack. In the transverse plane the onset of separation occurred sooner for smaller width wakes and for higher angles of attack. In both planes the presence of a free-stream wake flow significantly hastened the onset of separation.

The current results were obtained using 26 normal points in the boundary layer for sharp cones and 101 normal points for blunt cones. The number of circumferential solutions planes was limited to 7 in order to avoid prohibitive computer times. In order to do an effective study of separation in three-dimensional cases, it would be desirable to have at least 31 solution planes in the boundary layer.

SECTION IV

CONCLUSIONS

1. Heat-transfer and skin-friction coefficients increase along the windward streamline of a sharp cone relative to conical flow values when the cone is subjected to a nonuniform supersonic free stream.

2. Heat-transfer and skin-friction coefficients are higher on the windward side of a sharp cone in nonuniform flow and lower on the leeward side relative to the conical flow solution. The trend of the uniform flow data is preserved in the nonuniform data. Higher values of the coefficients near the windward plane and lower values of the coefficients near the leeward plane are attained as S increases. This effect is more pronounced for heat transfer than for skin-friction distribution.

3. Increasing the angle of attack causes more pronounced departures from uniform flow results for cones in nonuniform flow. This is the case in both the streamwise and transverse directions.

4. The present sharp cone program for nonuniform free-stream flows has exhibited good agreement with existing uniform-flow solutions, experimental data, and existing nonuniform solutions, and the program is considered to be a useful, versatile tool for predicting boundary-layer flows over sharp cones at angle of attack to nonuniform supersonic free streams.

5. The present blunt-cone program for nonuniform free streams has exhibited good agreement with experimental uniform flow data at both zero and non-zero angle of attack. The agreement with uniform flow data together with reasonable and consistent nonuniform flow results establishes the program as a useful and versatile tool for predicting boundary layer flows over blunt cones at angle of attack in nonuniform supersonic free streams.

6. Heat transfer along the windward streamline of a blunt cone increases relative to uniform flow values when the cone is subjected to nonuniform supersonic free streams. Decreasing the width of the wake causes a further departure from uniform flow values.

7. In the blunt nose region of a blunt cone ($S/R_n < 2$), the nonuniformity of the free stream has little effect on the values of skin friction or heat transfer along the windward streamline. The location of the peak skin friction and its value remain very nearly constant with changes in angle of attack, velocity defect, and/or width of the wake.

8. Skin friction along the windward streamline of a blunt cone in axisymmetric wake flow increases relative to the uniform flow values before falling below the uniform flow values far downstream. The "crossover" point is a function of the angle of attack.

9. Both skin-friction and heat-transfer coefficients decrease around the cone from the windward plane to the leeward plane; however, the values of the coefficients are higher than the corresponding uniform flow values. (This is not uniformly true for skin friction downstream of the "crossover" point described above.)

10. Free-stream nonuniformities hasten the onset of separation in both the longitudinal and transverse planes. Smaller width wakes cause separation to occur sooner in both planes.

11. All effects attributed to the nonuniform free stream, for both sharp and blunt cones, are substantially "magnified" by increasing the angle of attack.

REFERENCES

1. Bordner, G. L. and Davis, R. T., "Compressible Three-Dimensional Laminar Boundary Layers on Cones at Incidence to Shear and Axisymmetric Wake Flows", Aerospace Research Laboratories, ARL 71-0262, Wright-Patterson AFB, Ohio, 1971.

2. McGowan, J. J. and Davis, R. T. , "Development of a Numerical Method to Solve the Three-Dimensional Compressible Laminar Boundary-Layer Equations with Application to Elliptical Cones at Angle of Attack", Aerospace Research Laboratories, ARL-70-0341, Wright-Patterson AFB, Ohio, 1970.

3. Moore, F. G., "Calculation of Inviscid and Viscid Flow Fields Past Pointed Bodies at Angles of Attack in Supersonic Nonuniform Freestreams", Ph.D. Thesis, Virginia Polytechnic Institute and State University, 1971.

4. Lewis, C. H., Moore, F. G., Black, R. R., and DeJarnette, F. R., "Sharp and Blunt Cones at Angle of Attack in Supersonic Nonuniform Free Streams", AIAA Paper No. 71-51 presented at AIAA 9th Aerospace Sciences Meeting, New York, New York, January, 1971.

5. Moore, F. G., DeJarnette, F. R., and Brooks, E. N., "Supersonic Flow of Nonuniform Free-Streams Past Aerodynamic Decelerators", AIAA Paper No. 70-1176, September, 1970.

6. Black, R. R. and Lewis, C. H., "Inviscid Flow Over Sharp and Blunt Cones at Angle of Attack in Nonuniform Supersonic Free Streams", Aerospace Research Laboratories, ARL Report to be published, Wright-Patterson AFB, Ohio, 1973.

7. Miner, E. W., Anderson, E. C., and Lewis, C. H., "A Computer Program for Two-Dimensional and Axisymmetric Nonreacting Perfect Gas and Equilibrium Chemically Reacting Laminar, Transitional and/or Turbulent Boundary Layer Flows", VPI Engineering Report E-71-8, Virginia Polytechnic Institute and State University, 1971.

8. Cleary, J. W., "Effects of Angle of Attack and Bluntness on Laminar Heating-Rate Distributions of a 15^{o} Cone at a Mach Number of 10.6", NASA TN D-5450, Ames Research Center, Moffet Field, California, 1969.

9. Widhopf, G. F., "Laminar, Transitional, and Turbulent Heat Transfer Measurements on a Yawed Blunt Conical Nosetip", TR-0073(S3450-60)-1, The Aerospace Corporation, San Bernardino, California, 1972, Air Force Report No. SAMSO-TR-72-209.

10. Lomax, H. and Inouye, M., "Numerical Analysis of Flow Properties About Blunt Bodies Moving at Supersonic Speeds in an Equilibrium Gas", NASA TR R-204, 1964.

11. Inouye, M., Rakich, J. V., and Lomax, H., "A Description of Numerical Methods and Computer Programs for Two-Dimensional and Axisymmetric Supersonic Flow Over Blunt-Nosed and Flared Bodies", NASA TN D-2970, 1965.

12. Rakich, J. V., "A Method of Characteristics for Steady Three-Dimensional Supersonic Flow with Application to Inclined Bodies of Revolution", NASA TN D-5341, Ames Research Center, Moffet Field, California, 1969.

13. Anderson, E. C. and Lewis, C. H., "Laminar or Turbulent Boundary-Layer Flows of Perfect Gases or Reacting Gas Mixtures in Chemical Equilibrium", NASA CR-1893, Langley Research Center, Virginia, 1971.

BIBLIOGRAPHY

Black, R. R., Frieders, M. C., and Lewis, C. H., "A Computerized Analysis of Supersonic Nonuniform Flows Over Sharp and Spherically Blunted Cones at Angle of Attack", Paper No. 3A(2) presented at the Two-Day Symposium on Application of Computers to Fluid Dynamics Analysis and Design, Polytechnic Institute of Brooklyn, Farmingdale, N. Y., January, 1973.

Boericke, R. R., "The Laminar Boundary Layer on a Cone at Incidence in Supersonic Flow", AIAA Paper No. 70-48 presented at AIAA 8th Aerospace Sciences Meeting, New York, N. Y., January, 1970.

Carnahan, B., Luther, H. A., Wilkes, J. O., Applied Numerical Methods, John Wiley and Sons, New York, N. Y., 1969.

Curle, N., Laminar Boundary Layer Equations, Oxford University Press, London, 1965, Oxford Mathematical Monographs.

Der, Joe, Jr., "A Study of General Three-Dimensional Boundary-Layer Problems by an Exact Numerical Method", AIAA Journal, Vol. 9, No. 7, July, 1971.

Der, Joe, Jr. and Raetz, G. S., "Solution of General Three-Dimensional Laminar Boundary-Layer Problems by an Exact Numerical Method", IAS Paper No. 62-70 presented at the IAS 30th Annual Meeting, New York, N. Y., January, 1962.

Dwyer, H. A., "The Analysis and Calculation of the Three-Dimensional Boundary Layer over a Sharp Cone at Angle of Attack", Sandia Corporation Contract (48-7084) with the University of California, Davis, California, 1969.

Frieders, M. C. and Lewis, C. H., "Laminar Boundary Layers on Sharp and Blunt Cones at Angle of Attack in Supersonic Streams", Virginia Journal of Science, Vol. 23, No. 3, Fall, 1972, Abstract of talk presented at Virginia Academy of Science 50th Annual Meeting, Lexington, Virginia, May, 1972.

Kreyszig, Erwin, Advanced Engineering Mathematics, John Wiley and Sons, New York, N. Y., 1967.

Powers, S. A., Niemann, A. F., and Der, J., Jr., et al., "A Numerical Procedure for Determining the Combined Viscid-Inviscid Flow Fields Over Generalized Three-Dimensional Bodies", AFFDL-TR-67-124, Volume I, Air Force Flight Dynamics Laboratory, Wright-Patterson AFB, Ohio, 1967.

Schlichting, H., Boundary Layer Theory, McGraw-Hill Book Co., New York, N. Y., 1968.

Van Dyke, M., "Second Order Compressible Boundary-Layer Theory with Application to Blunt Bodies in Hypersonic Flow", AFOSR-TN-61-1270, Department of Aeronautical Engineering, Stanford University, 1961.

Widhopf, G. F., "Heat Transfer Correlations for Blunt Cones at Angle of Attack", TR-0172(S2816-63)-1, The Aerospace Corporation, San Bernardino, California, 1971, Air Force Report No. SAMSO-TR-71-157.

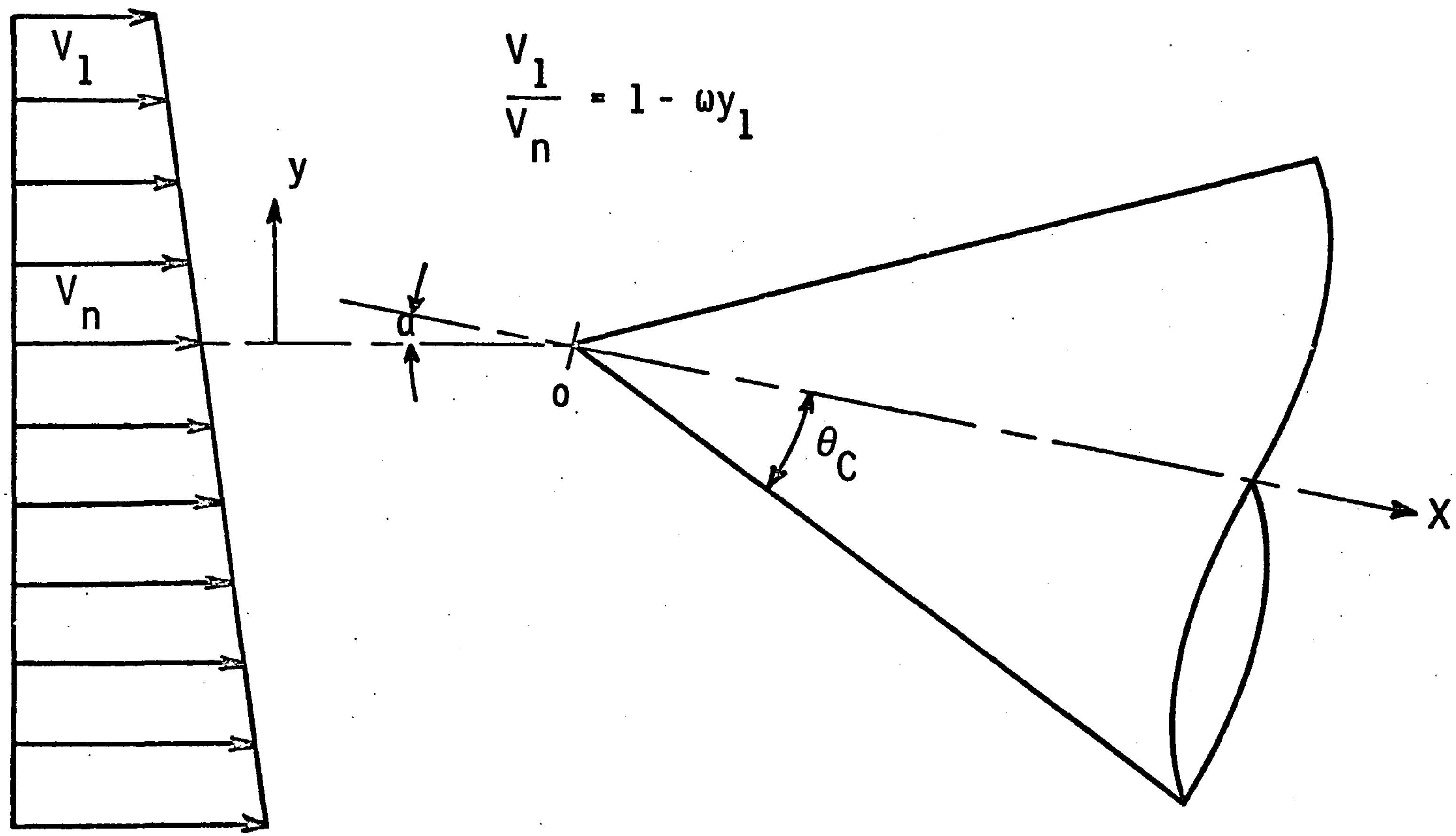

Figure 1. Sharp Cone in Two-Dimensional Shear Flow

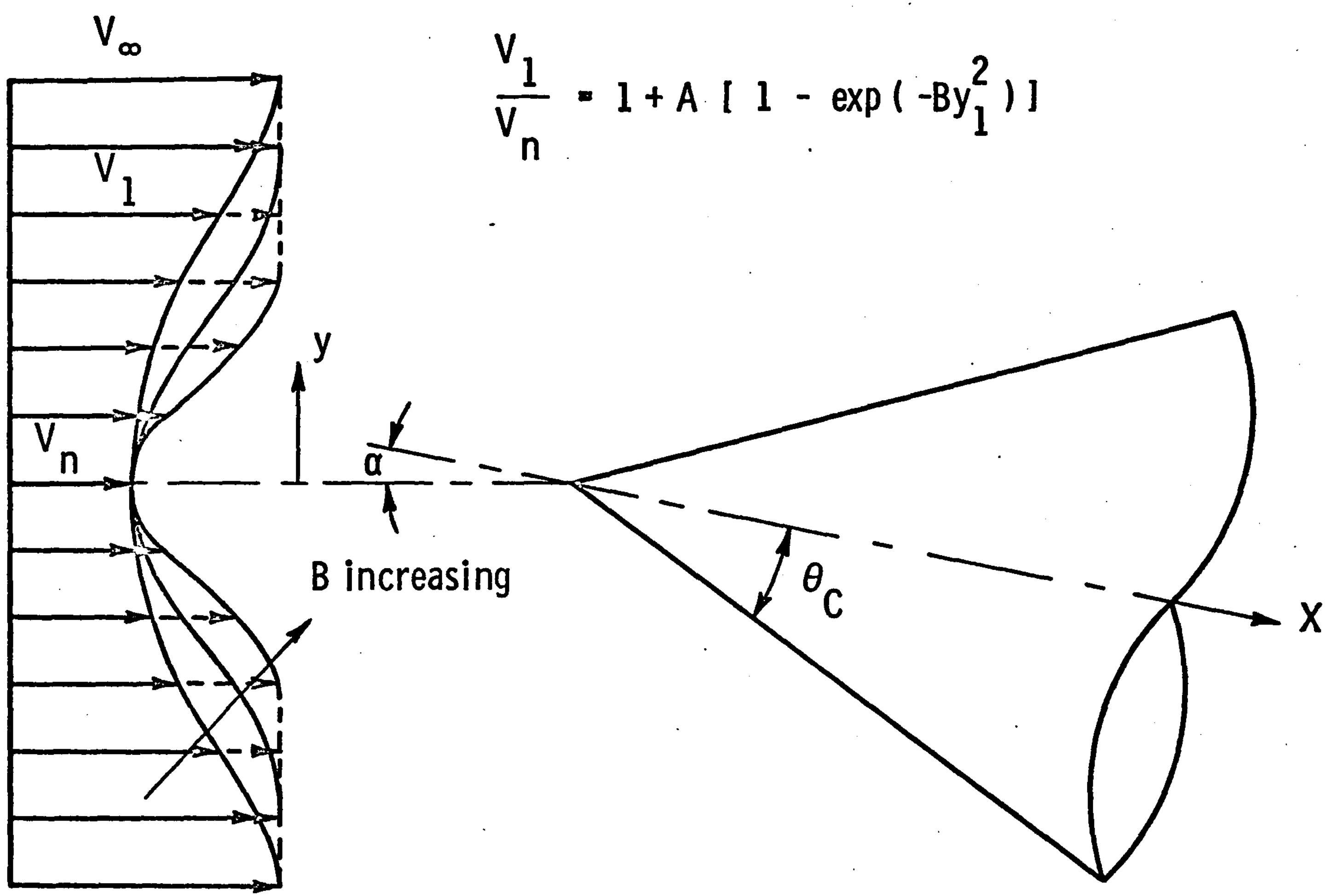

Figure 2. Sharp Cone in Axisymmetric Wake FLow

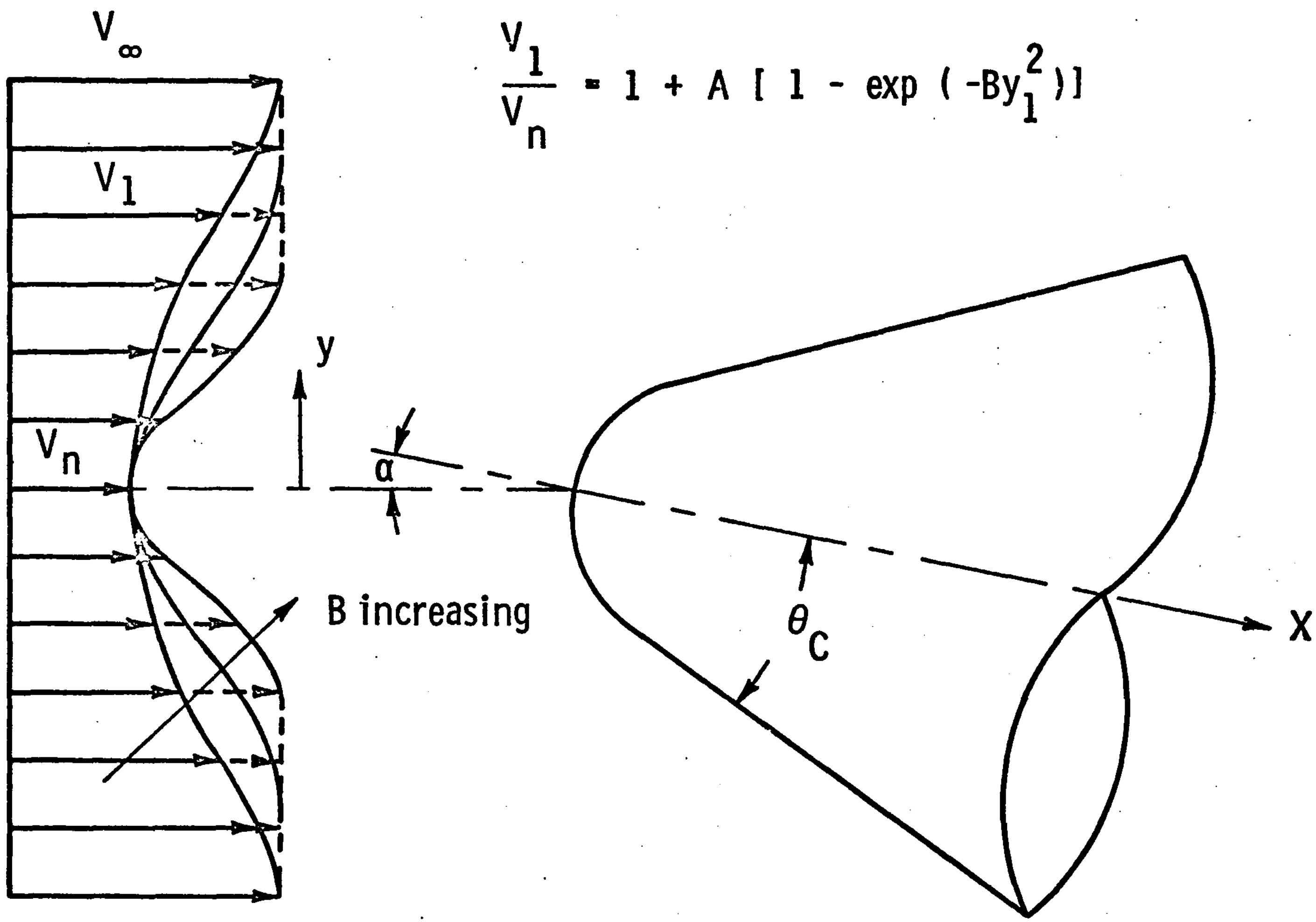

Figure 3. Blunt Cone in Axisymmetric Wake Flow

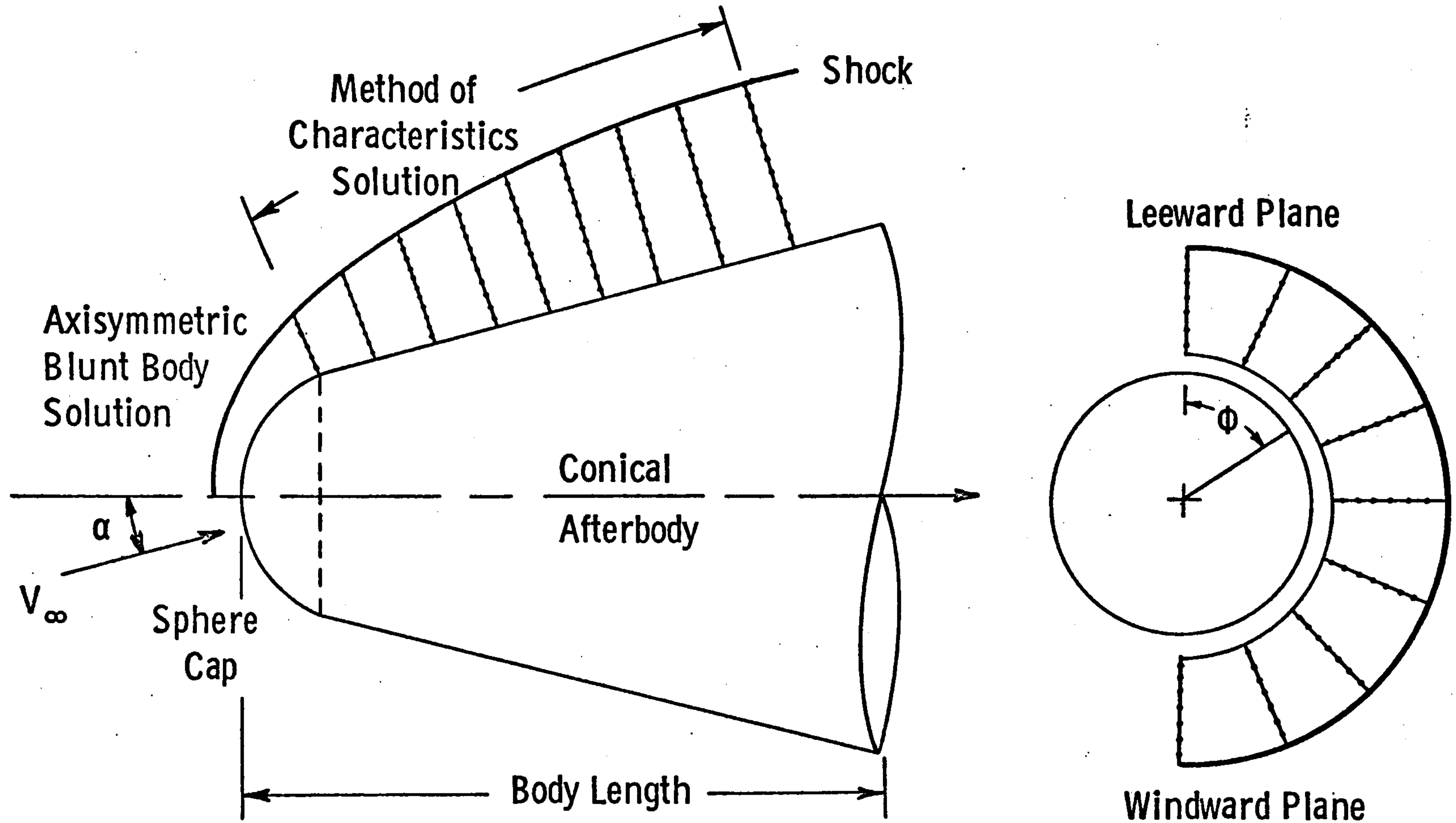

Figure 4. Solution Method for the Inviscid Flow Field of a Blunt Cone

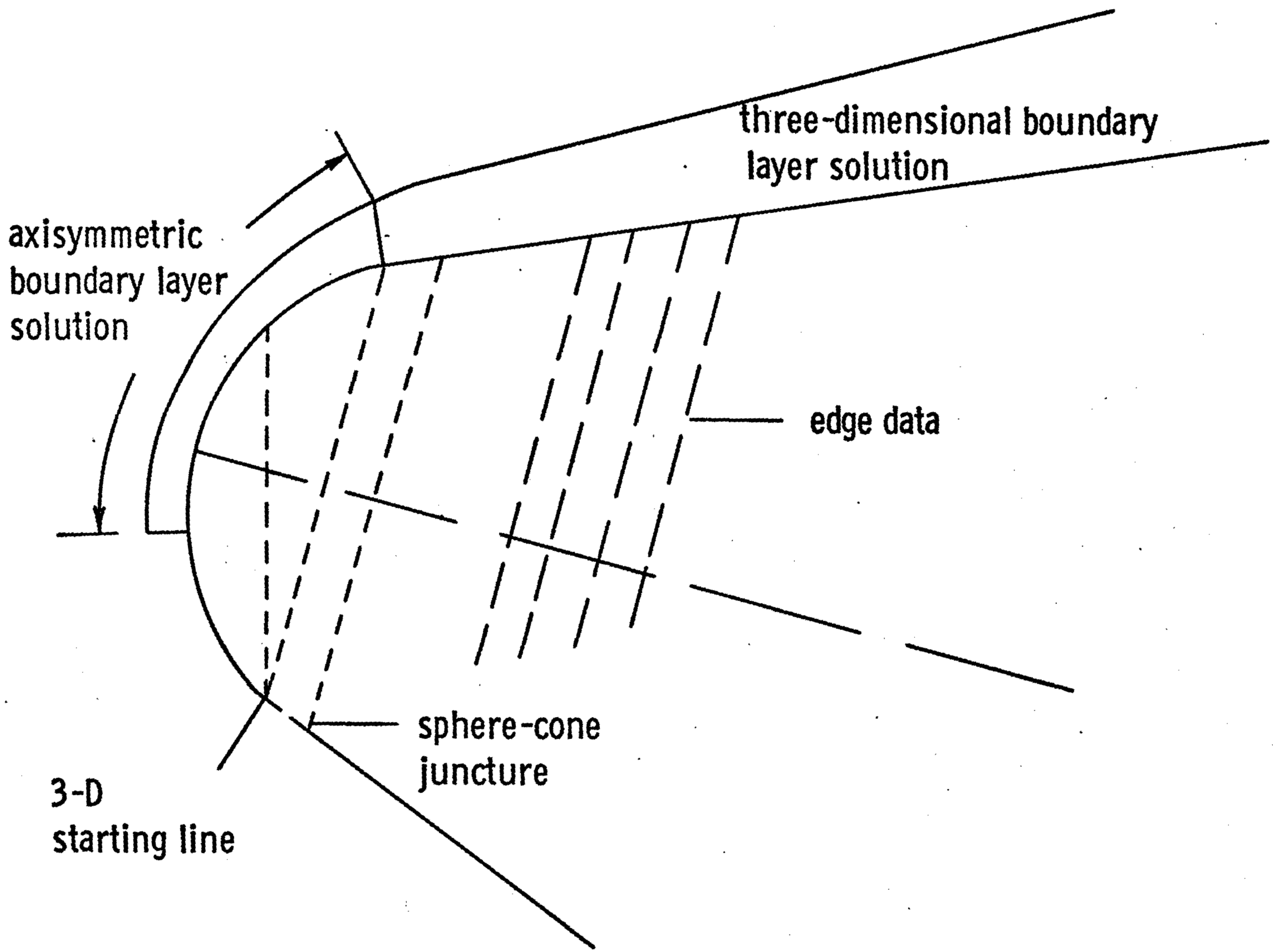

Figure 5. Solution Method for the Boundary Layer on a Blunt Cone

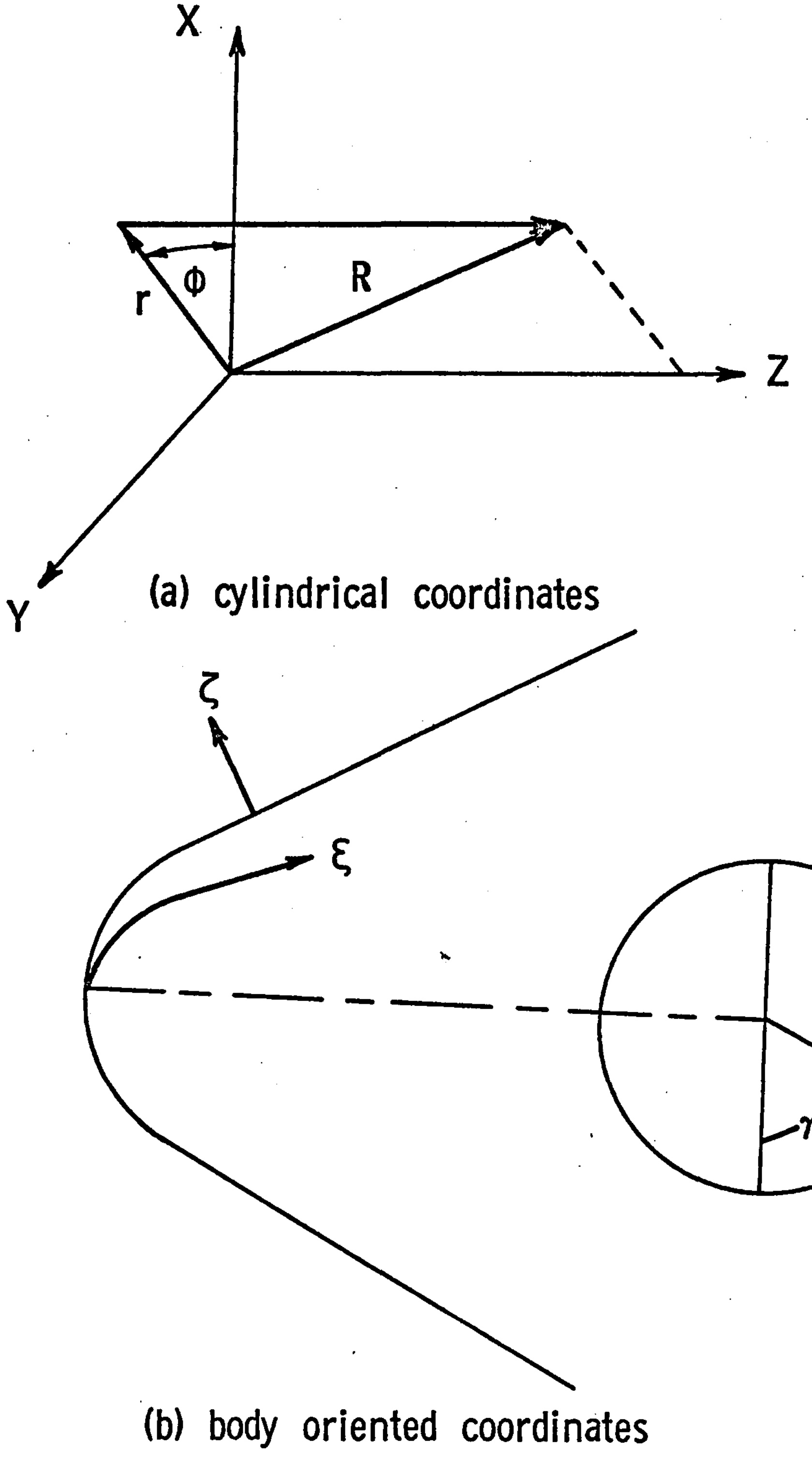

Figure 6. Body Oriented Coordinate System for Sharp and Blunt Cones Compared to a Cylindrical Coordinate System

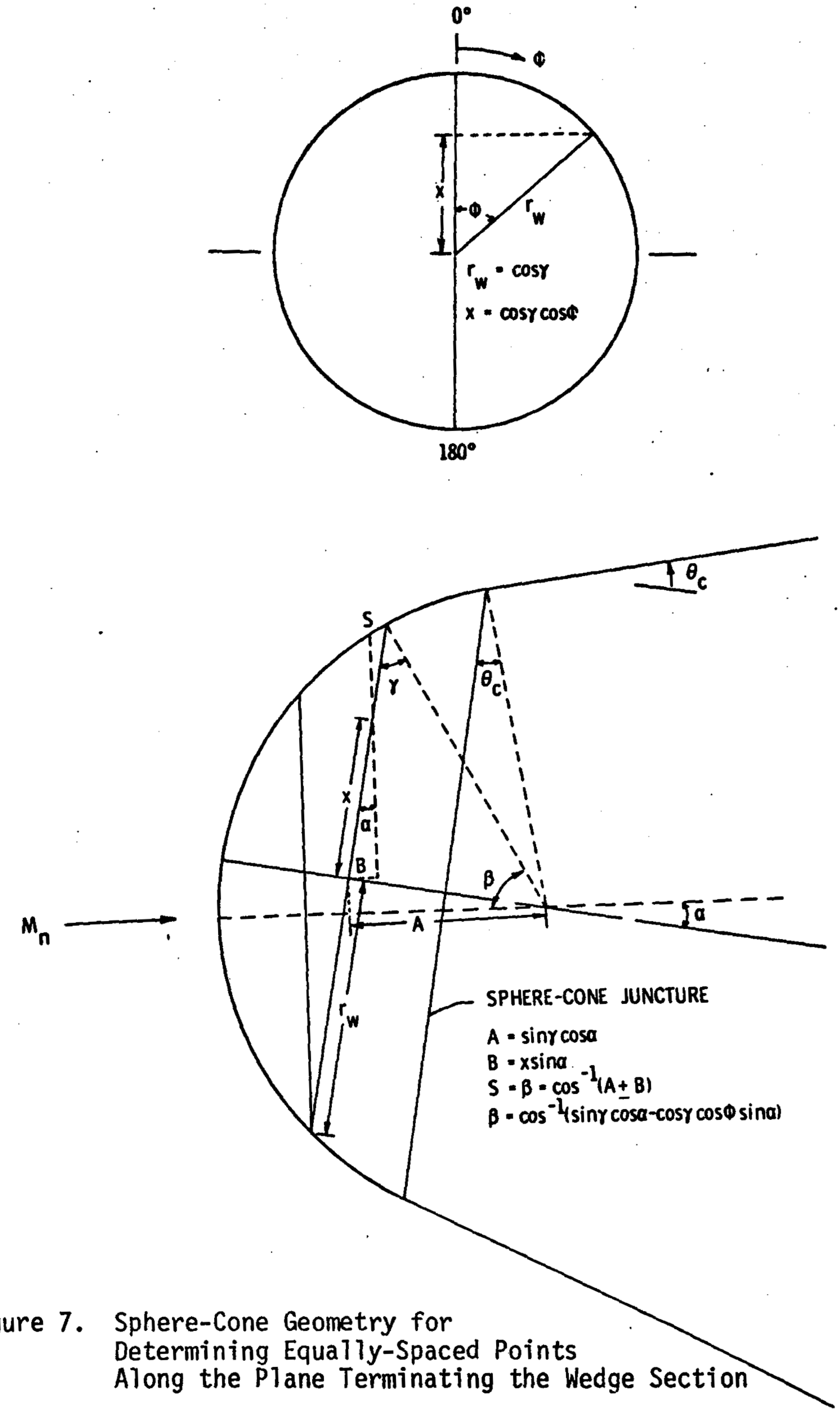

Figure 7. Sphere-Cone Geometry for Determining Equally-Spaced Points Along the Plane Terminating the Wedge Section

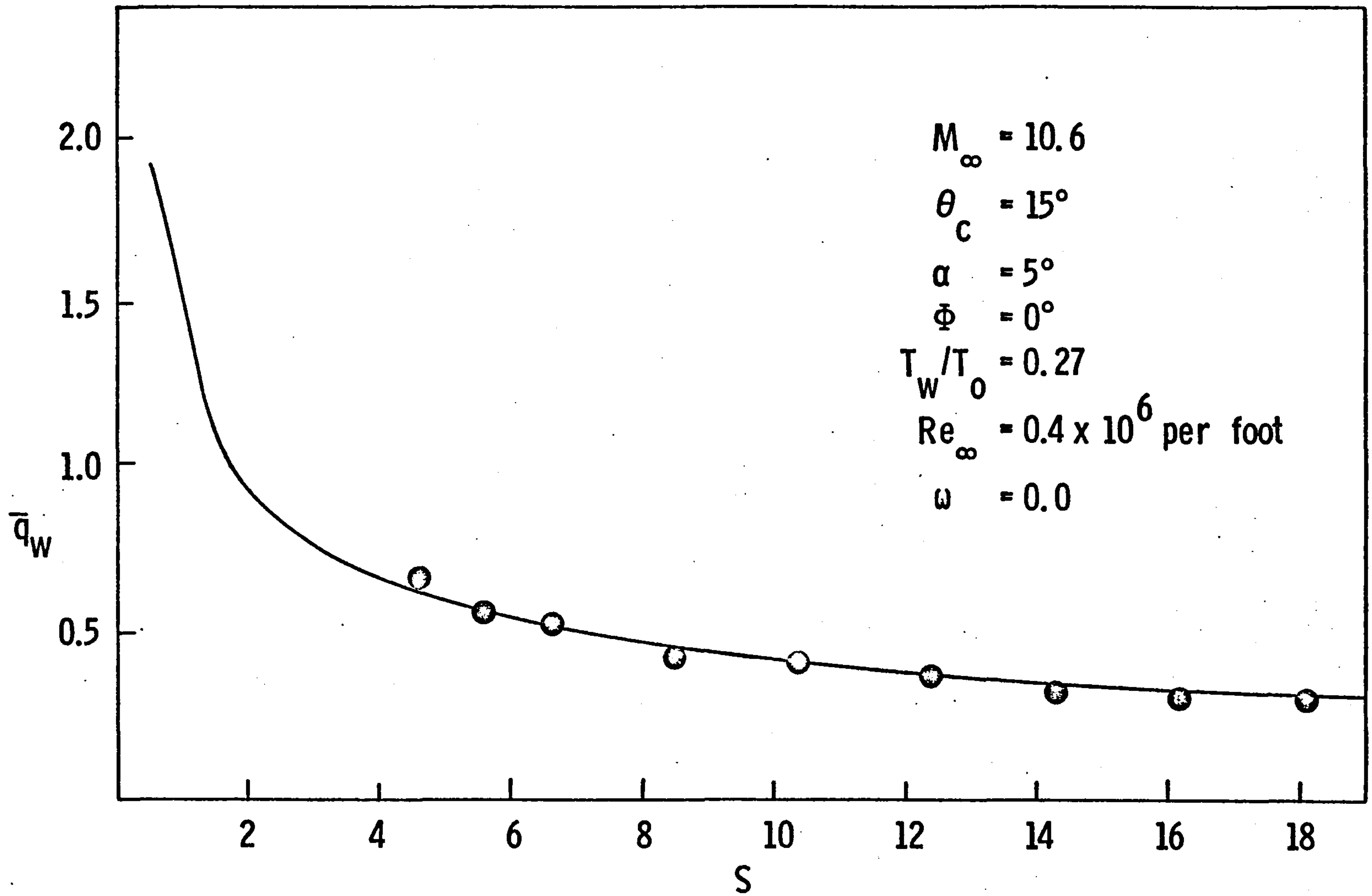

Figure 8. Heat Transfer Along the Windward Streamline of a Sharp Cone in Uniform Flow: Three-Dimensional Boundary-Layer Solution Compared to Experiment of Cleary

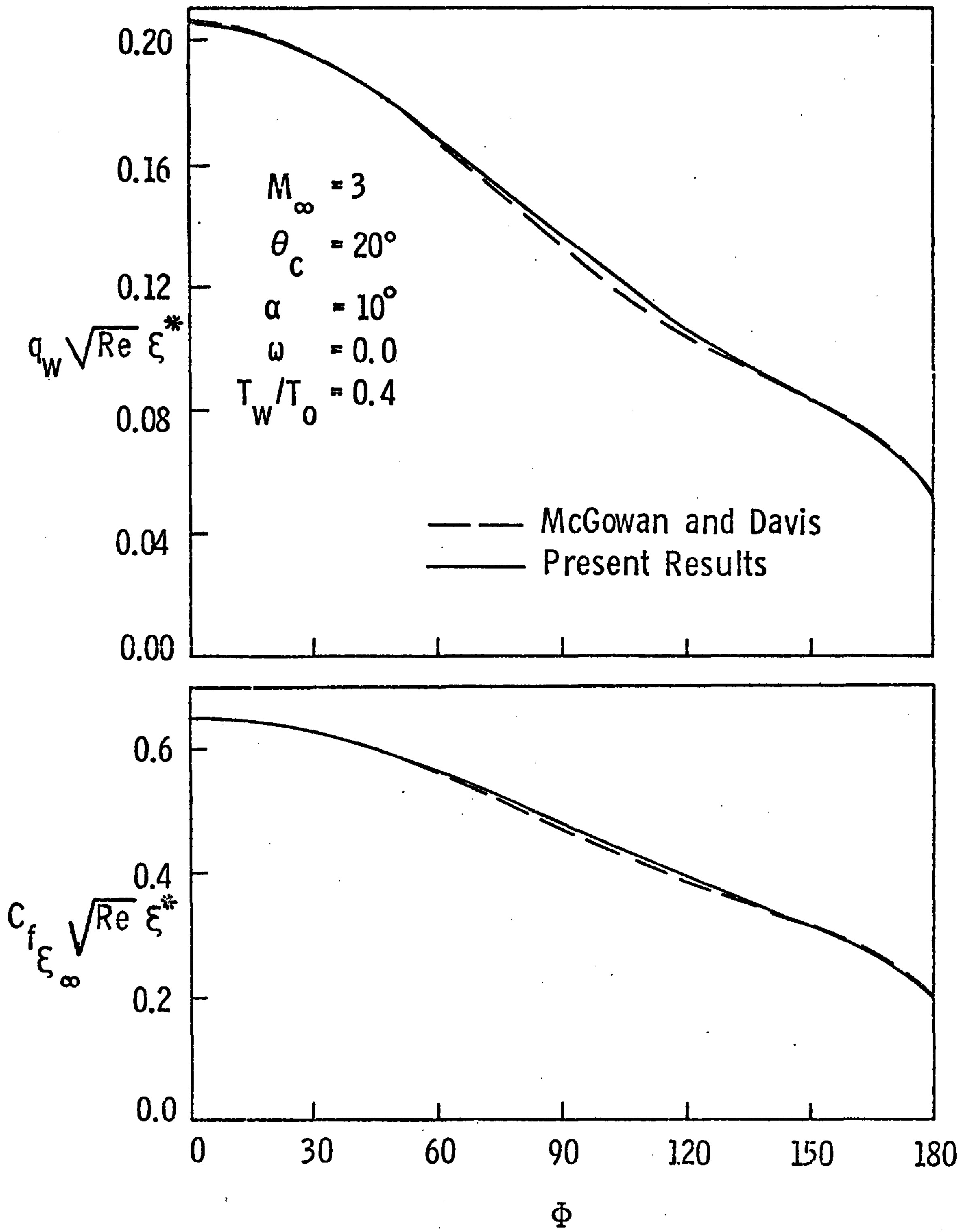

Figure 9. Transformed Heat Transfer and Skin Friction Coefficients Along the Windward Streamline of a Sharp Cone in Uniform Flow: Present Method Compared to Method of McGowan and Davis

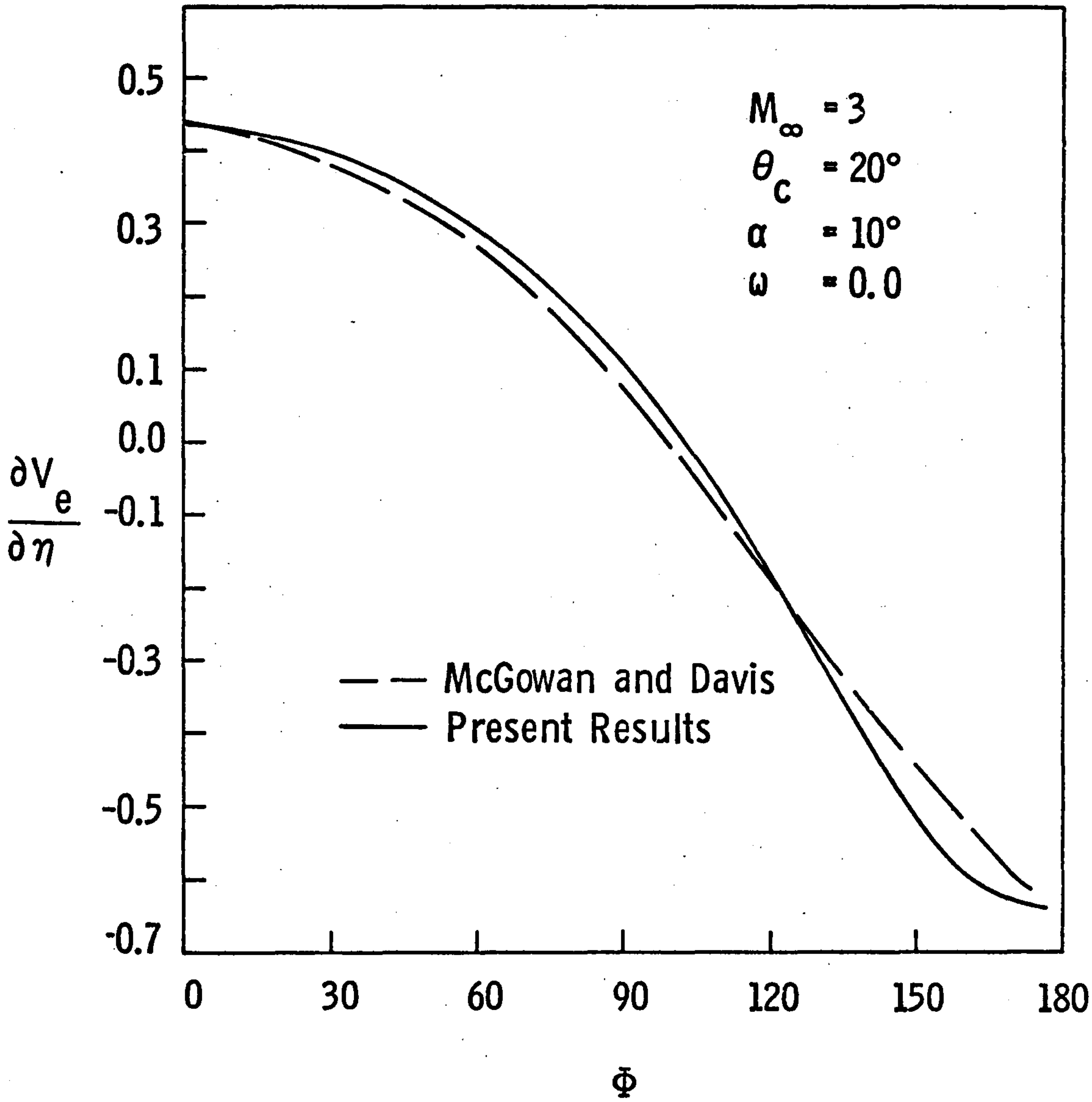

Figure 10. Transverse Cross Flow Derivative Around a Sharp Cone in Uniform Flow: Present Method Compared to Method of McGowan and Davis

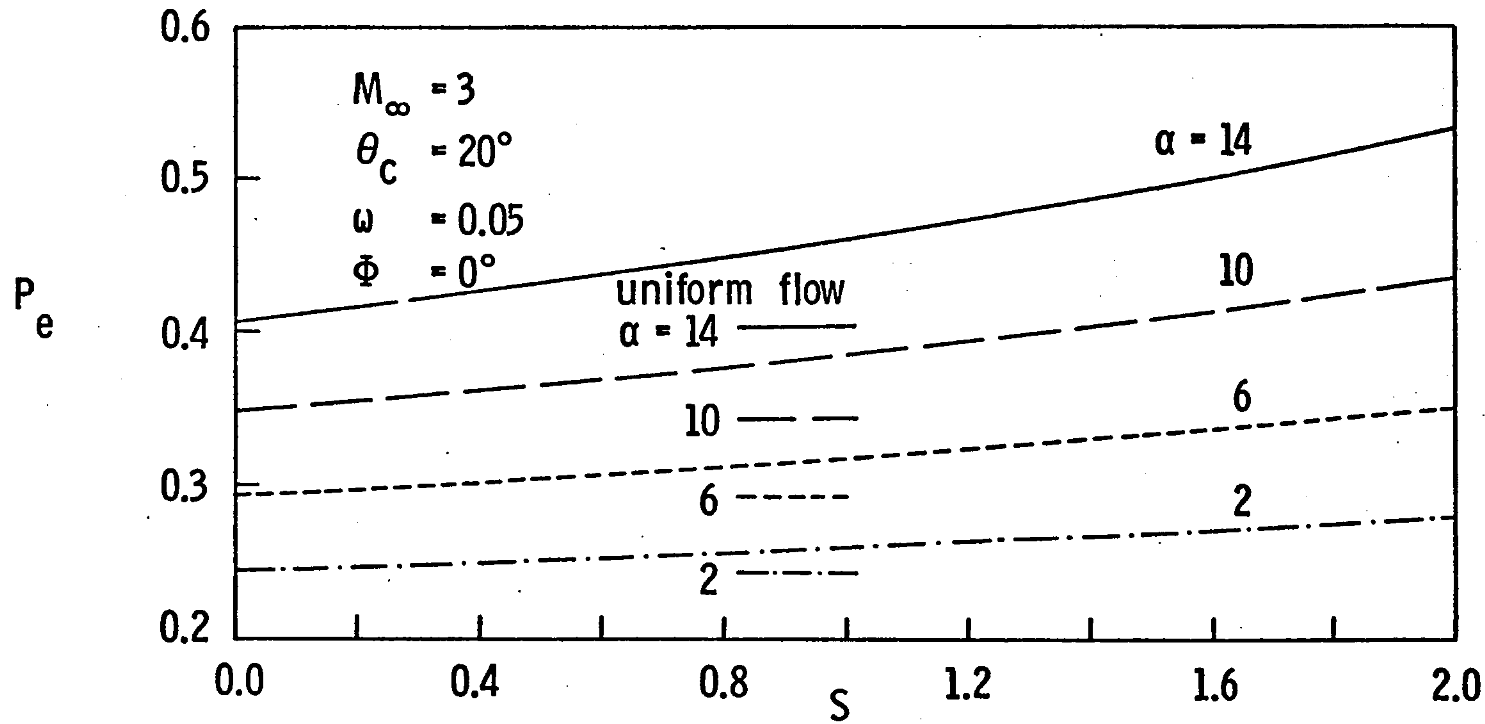

Figure 11. Pressure Distribution Along the Windward Streamline of a Sharp Cone at Varying Angle of Attack in Two-Dimensional Shear Flow

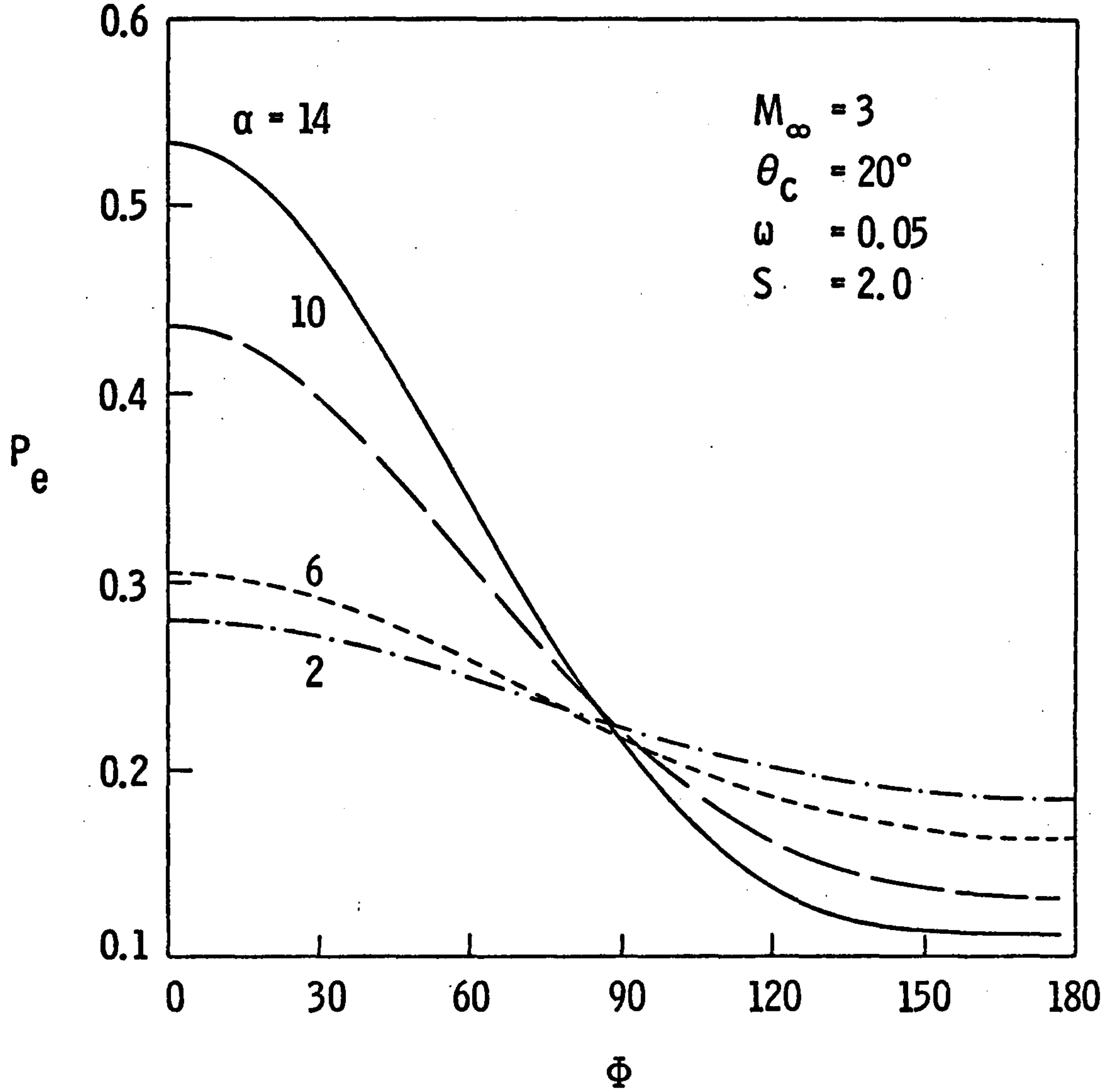

Figure 12. Pressure Distribution Around a Sharp Cone at Varying Angle of Attack in Two-Dimensional Shear Flow at S = 2

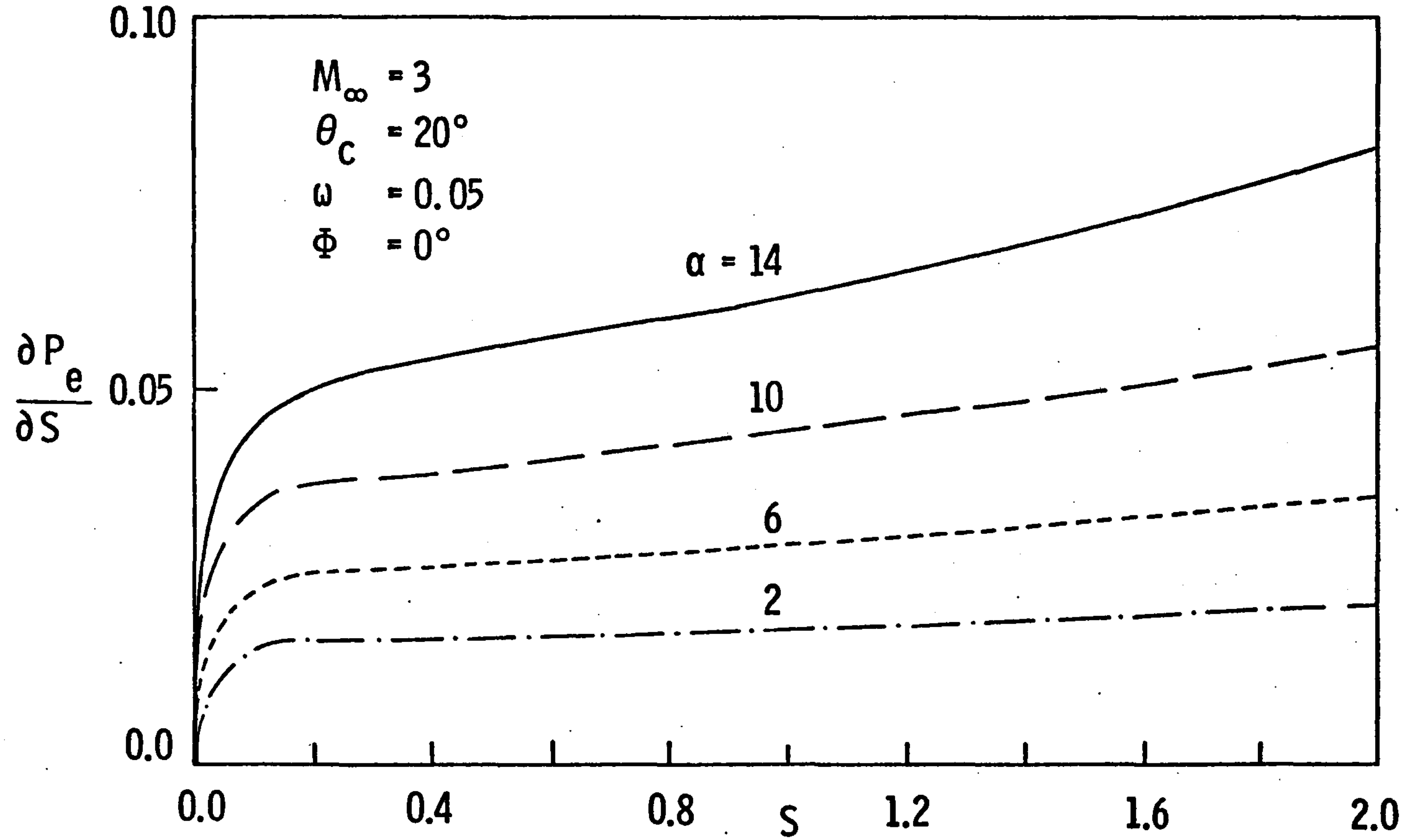

Figure 13. Streamwise Pressure Gradient Along the Windward Streamline of a Sharp Cone at Varying Angle of Attack in Two-Dimensional Shear Flow

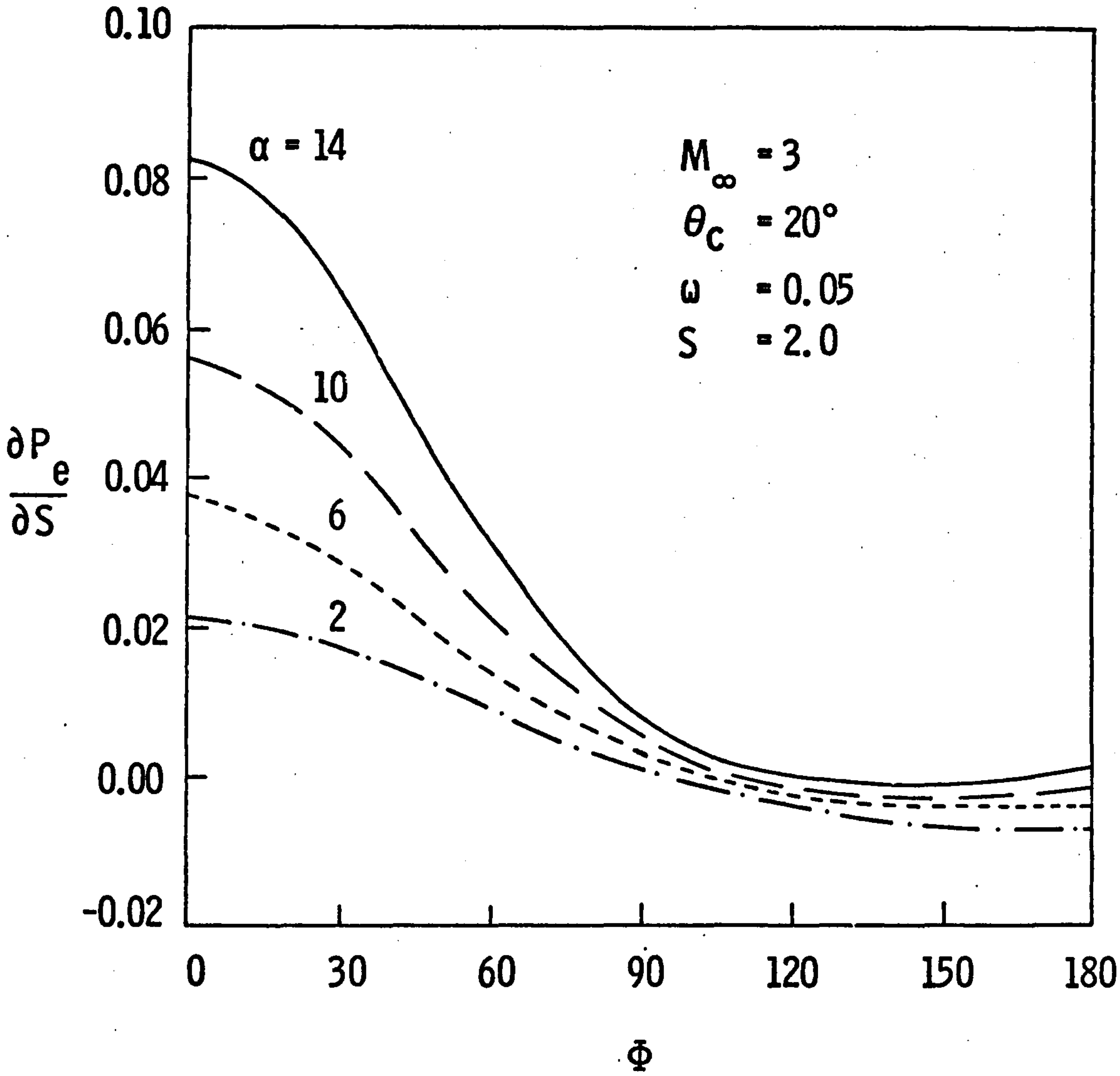

Figure 14. Streamwise Pressure Gradient Around a Sharp Cone at Varying Angle of Attack in Two-Dimensional Shear Flow at S = 2

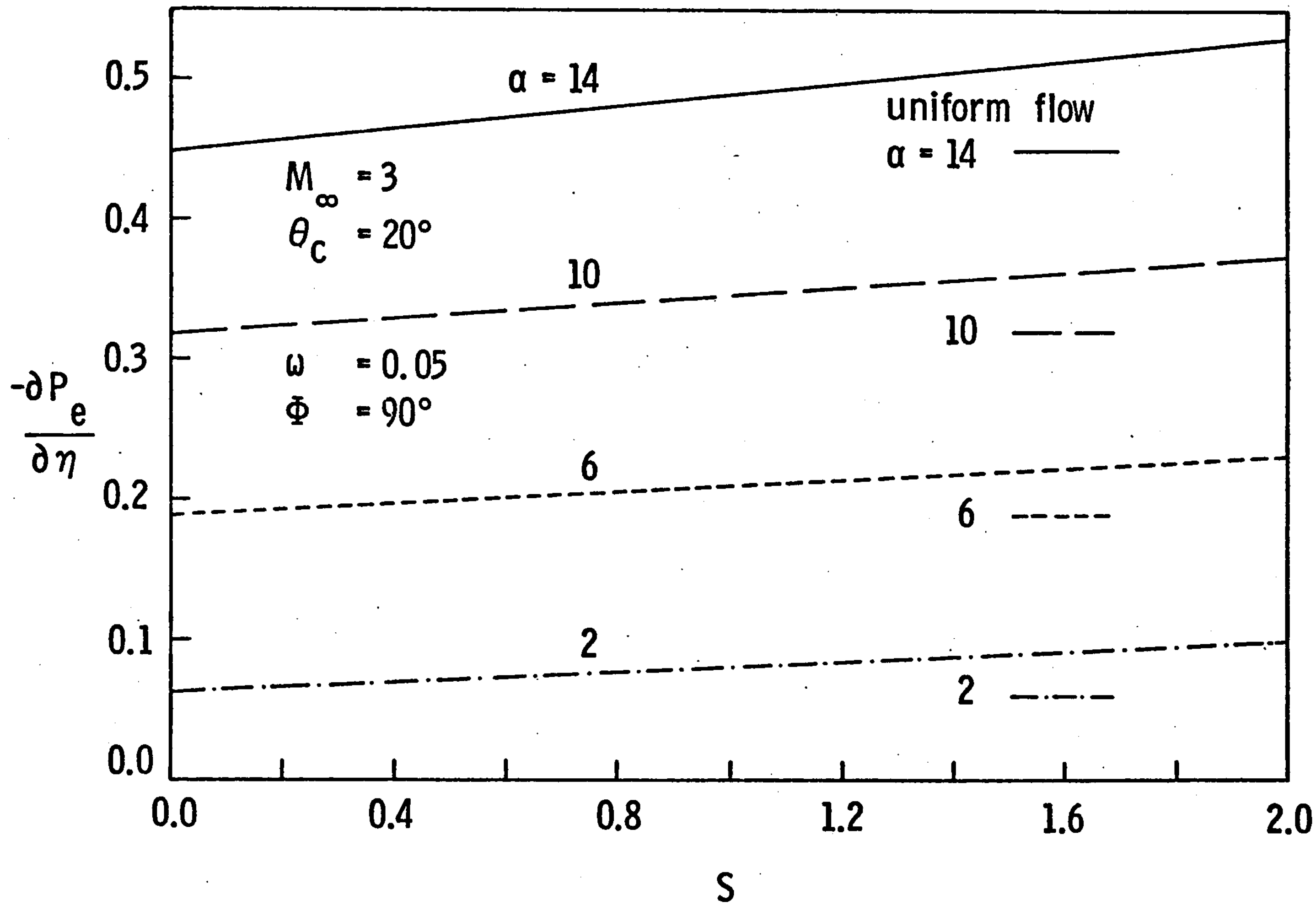

Figure 15. Transverse Pressure Gradient Along the Φ = 90° Streamline of a Sharp Cone at Varying Angle of Attack in Two-Dimensional Shear Flow

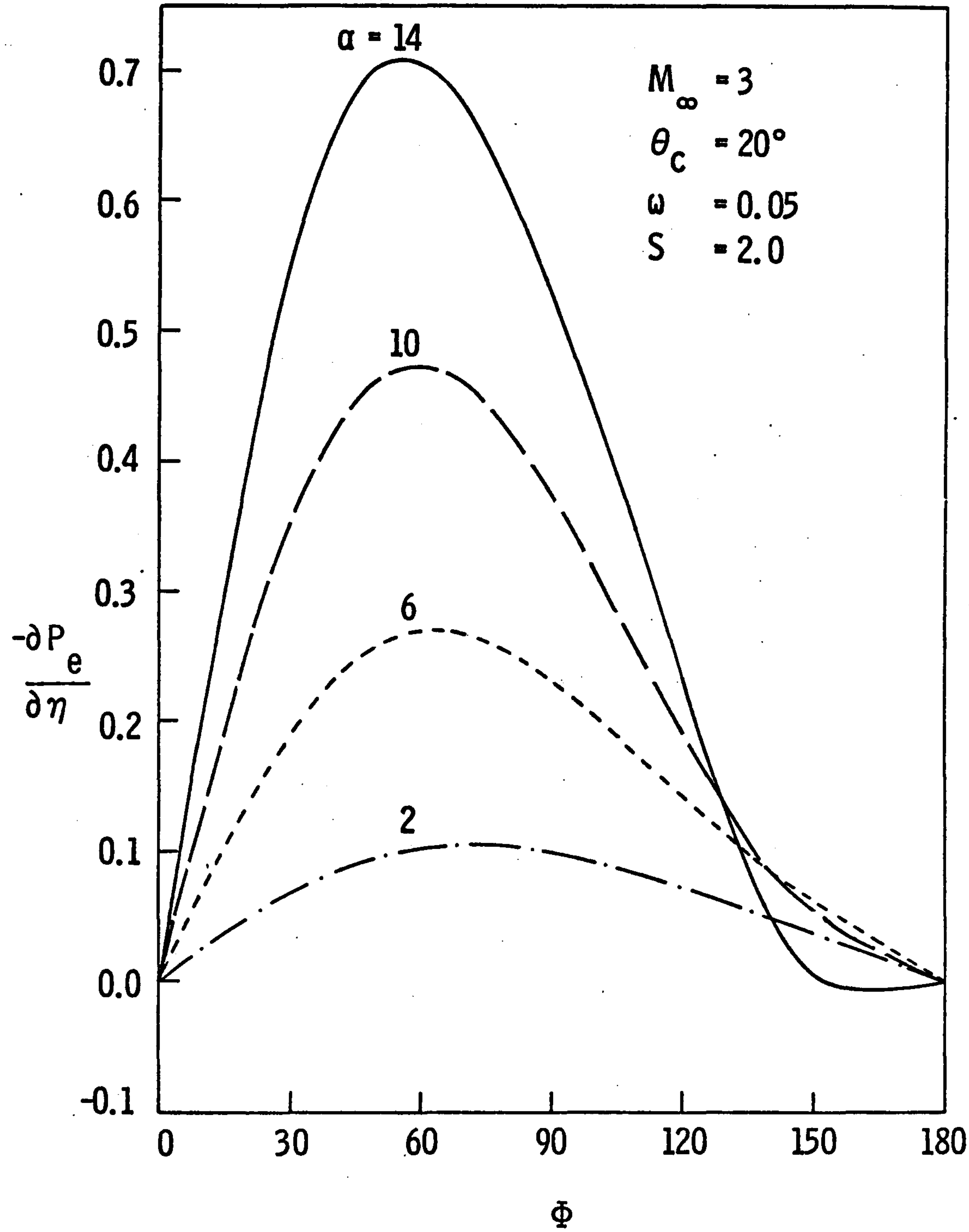

Figure 16. Transverse Pressure Gradient Around a Sharp Cone at Varying Angle of Attack in Two-Dimensional Shear Flow at S = 2

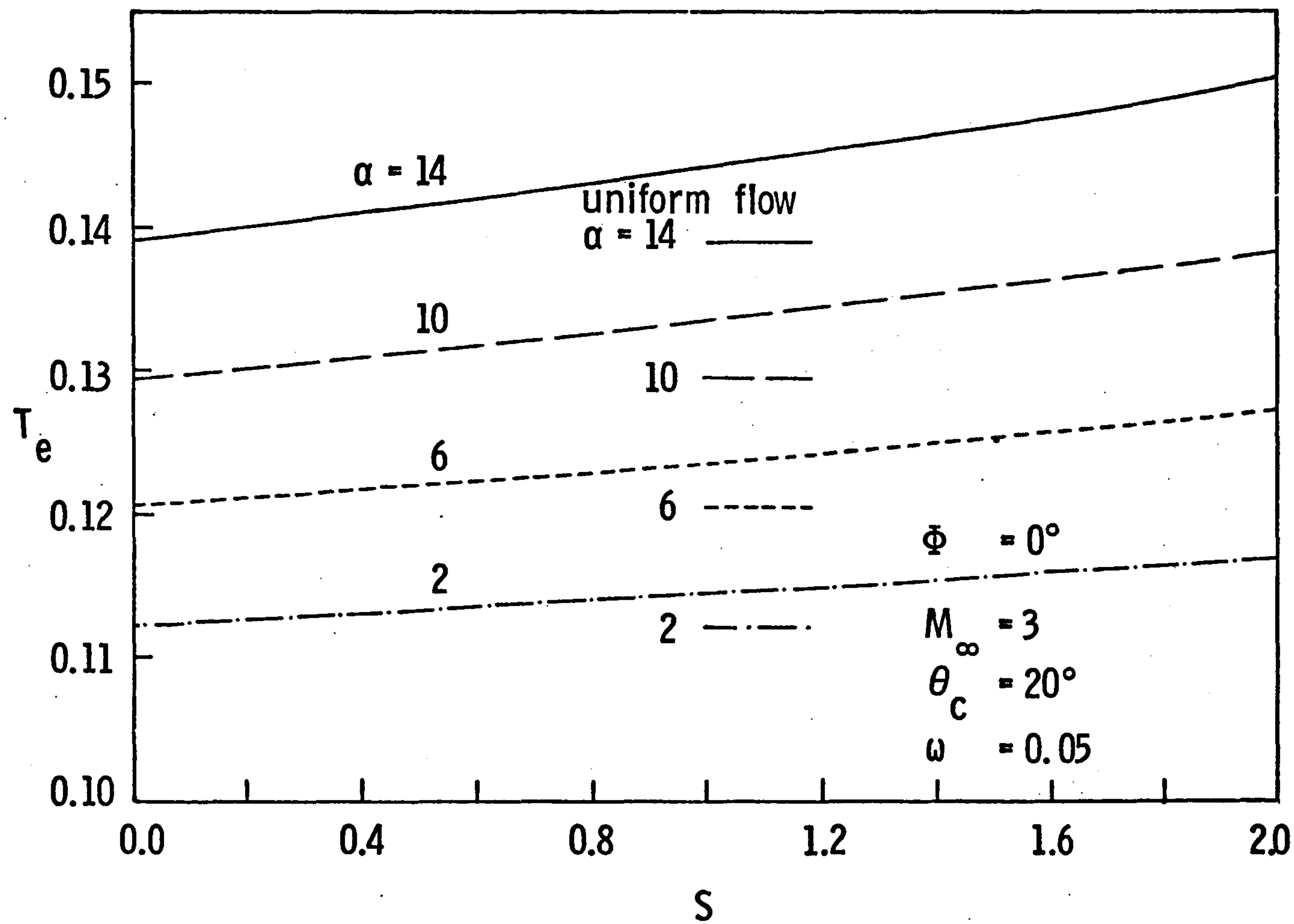

Figure 17. Temperature Distribution Along the Windward Streamline of a Sharp Cone at Varying Angle of Attack in Two-Dimensional Shear Flow

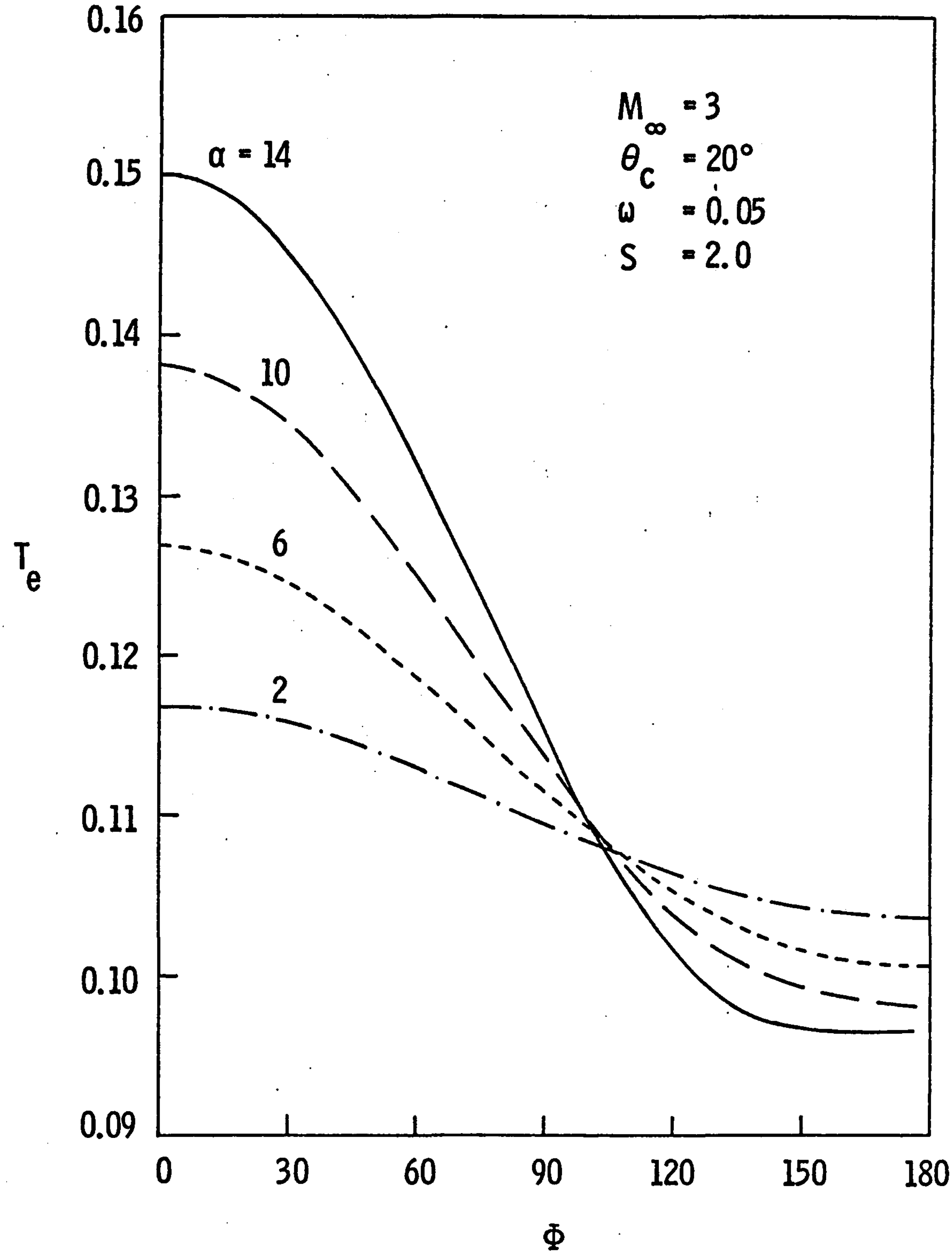

Figure 18. Temperature Distribution Around a Sharp Cone at Varying Angle of Attack in Two-Dimensional Shear Flow at S = 2

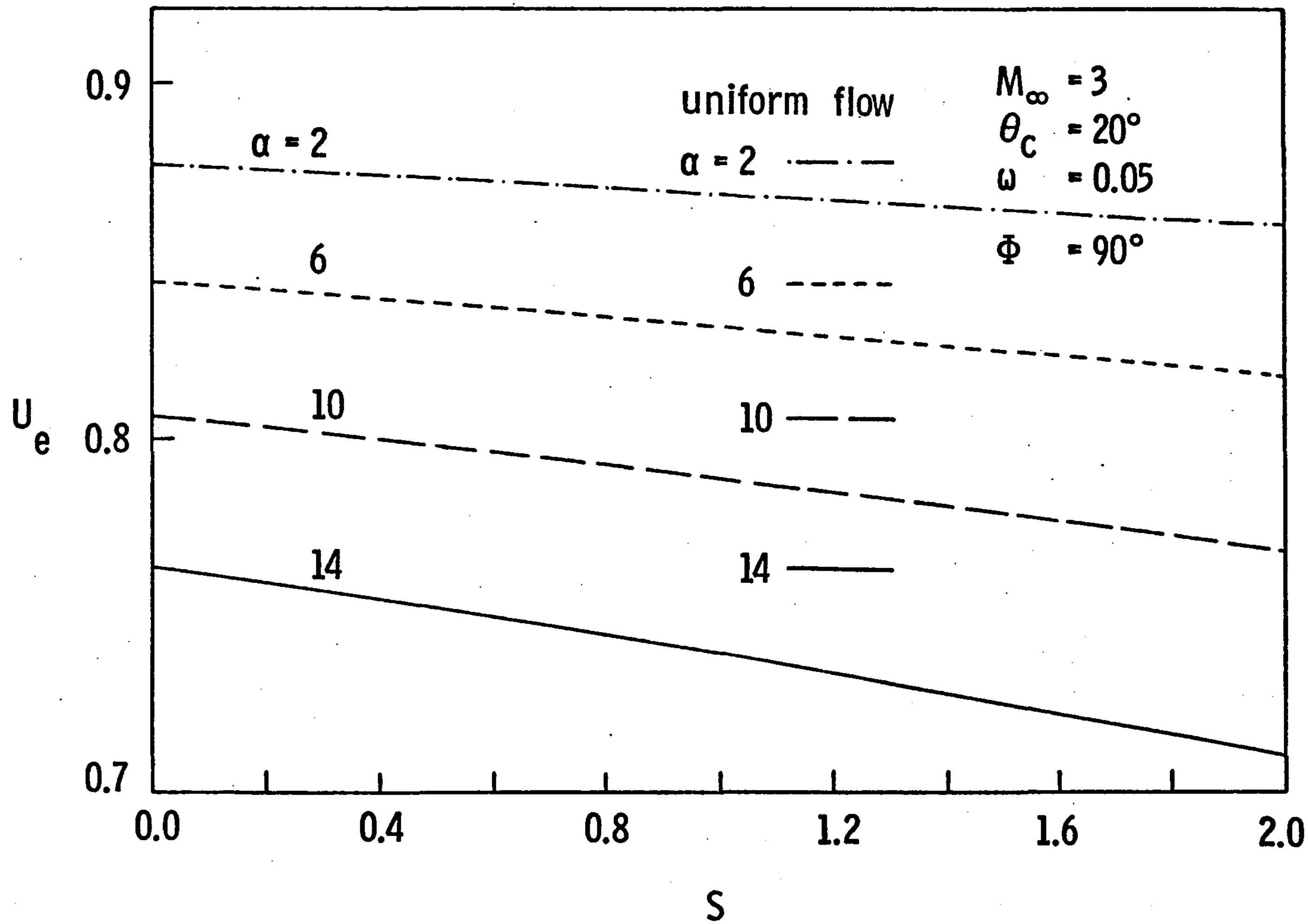

Figure 19. Longitudinal Velocity Distribution Along the Windward Streamline of a Sharp Cone at Varying Angle of Attack in Two-Dimensional Shear Flow

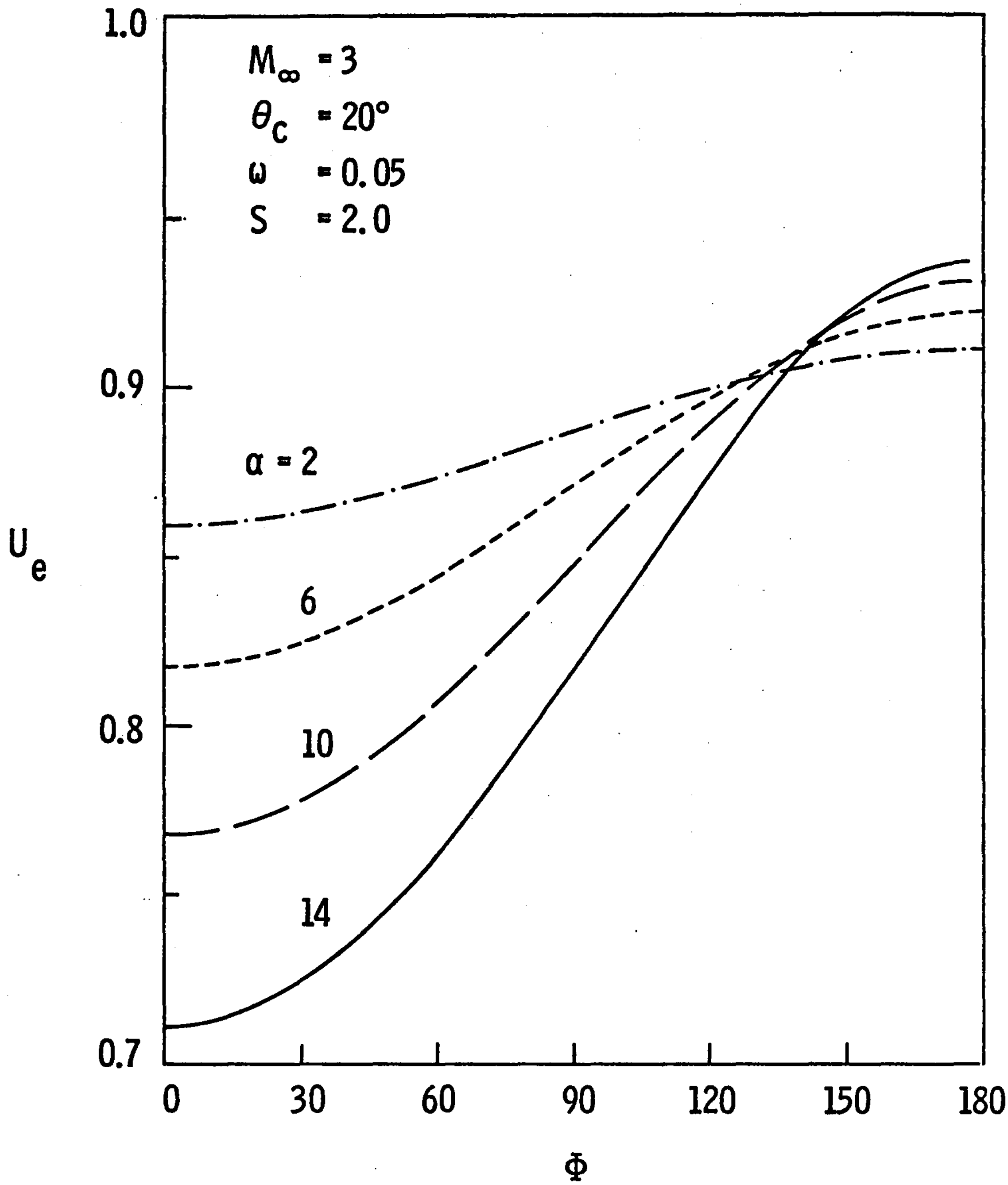

Figure 20. Longitudinal Velocity Distribution Around a Sharp Cone at Varying Angle of Attack in Two-Dimensional Shear Flow at S = 2

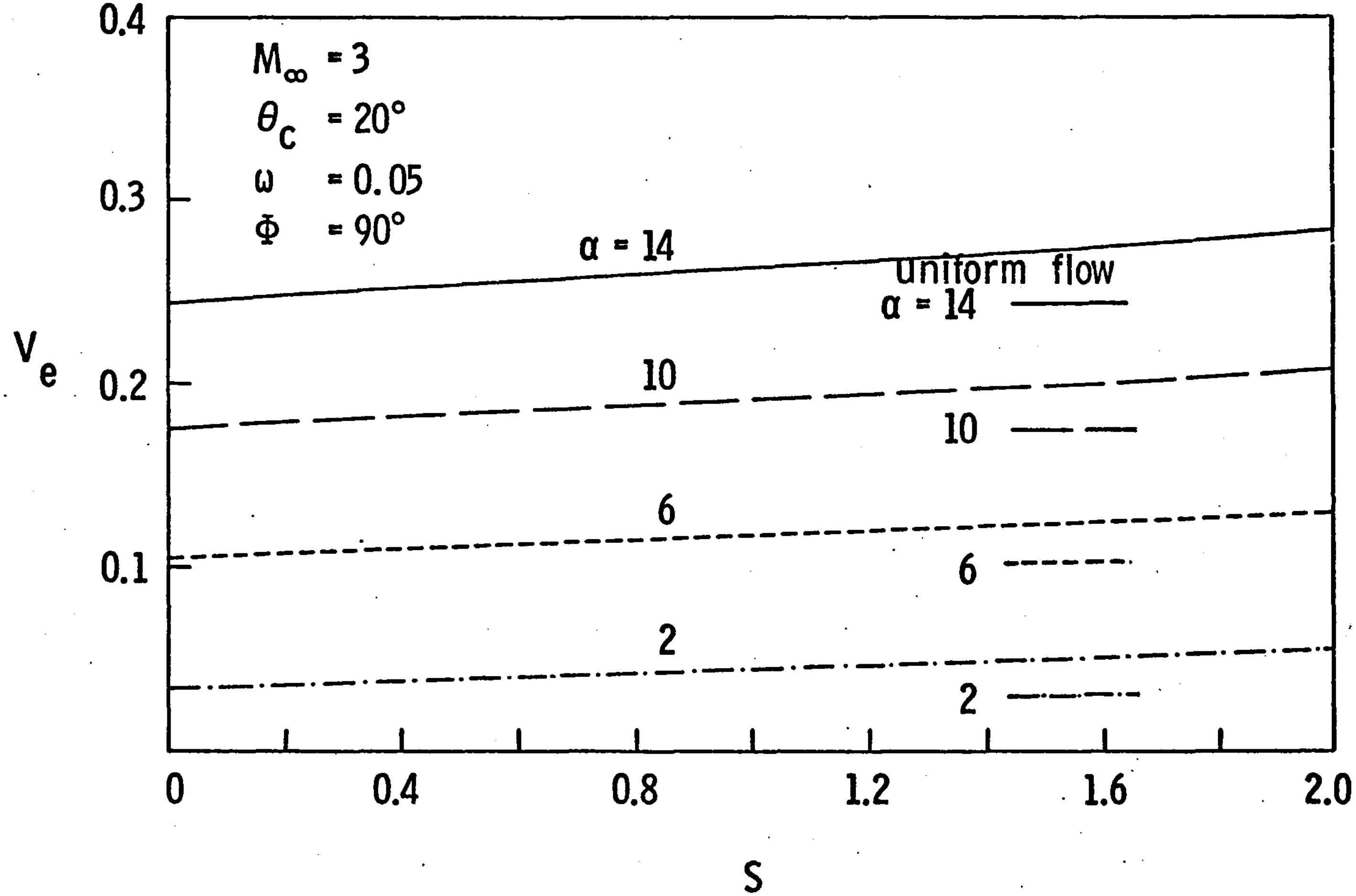

Figure 21. Cross Flow Velocity Distribution Along the Φ = 90° Streamline of a Sharp Cone at Varying Angle of Attack in Two-Dimensional Shear Flow

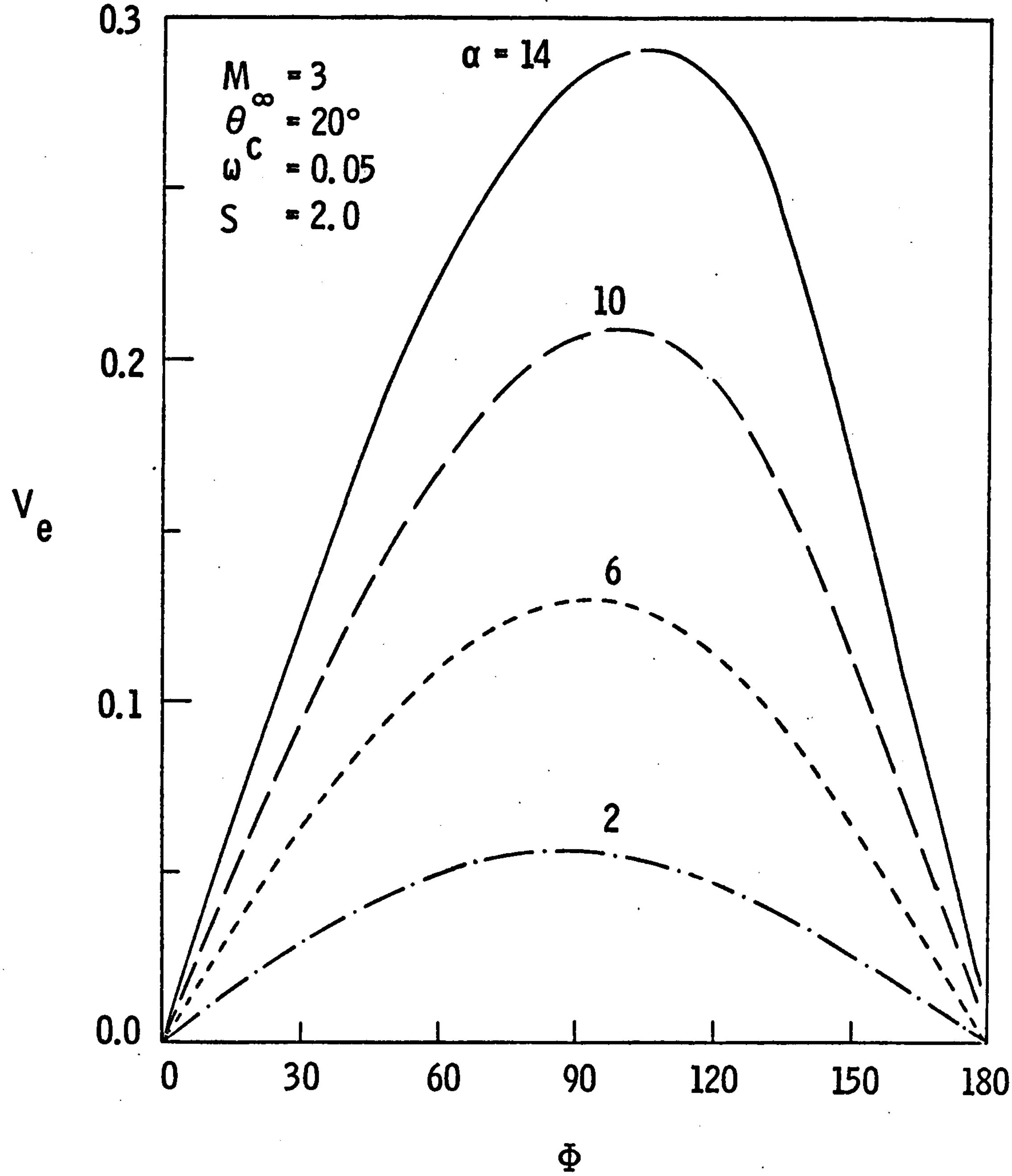

Figure 22. Cross Flow Velocity Distribution Around a Sharp Cone at Varying Angle of Attack in Two-Dimensional Shear Flow at S = 2

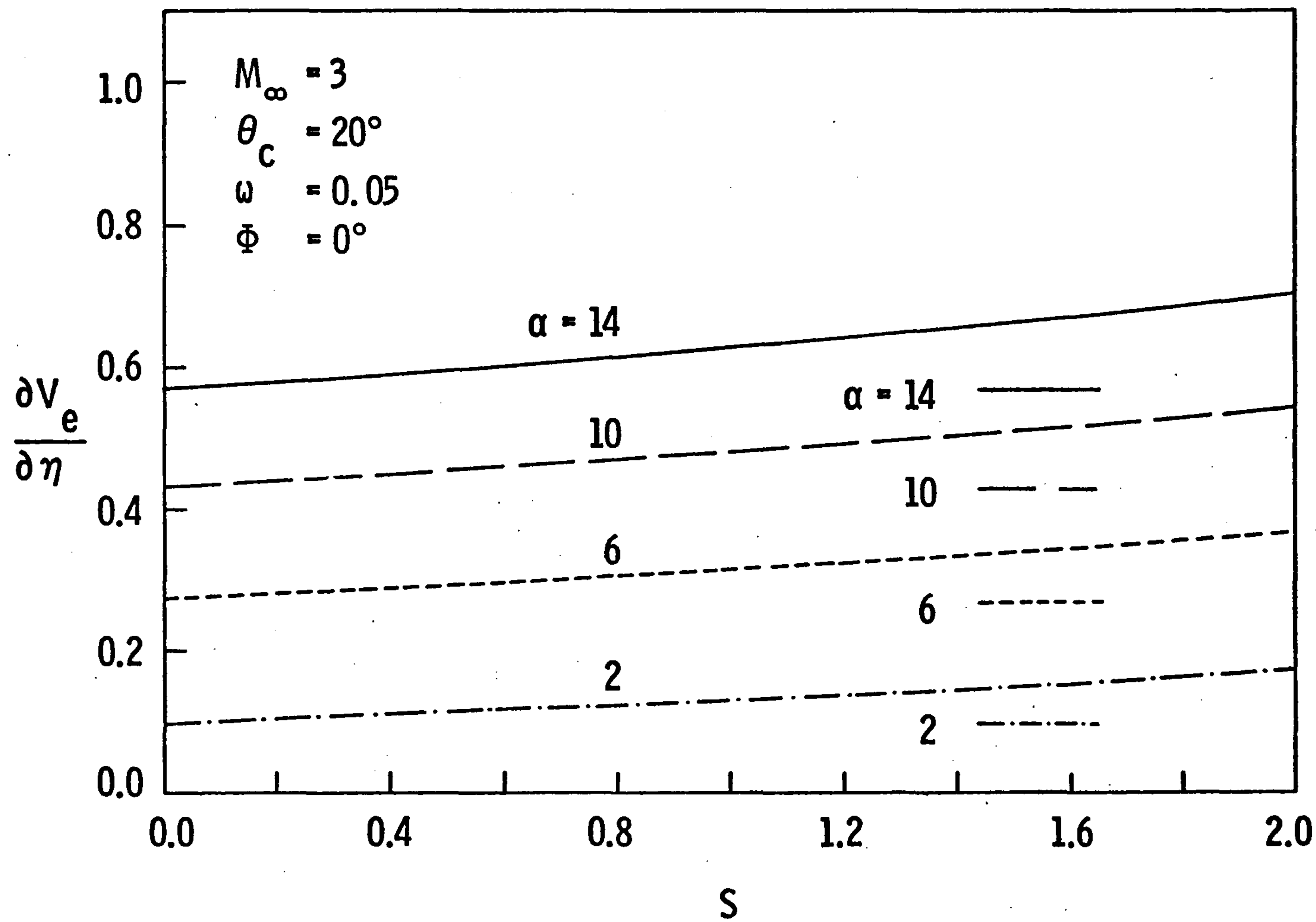

Figure 23. Transverse Cross Flow Derivative Along the Windward Streamline of a Sharp Cone at Varying Angle of Attack in Two-Dimensional Shear Flow

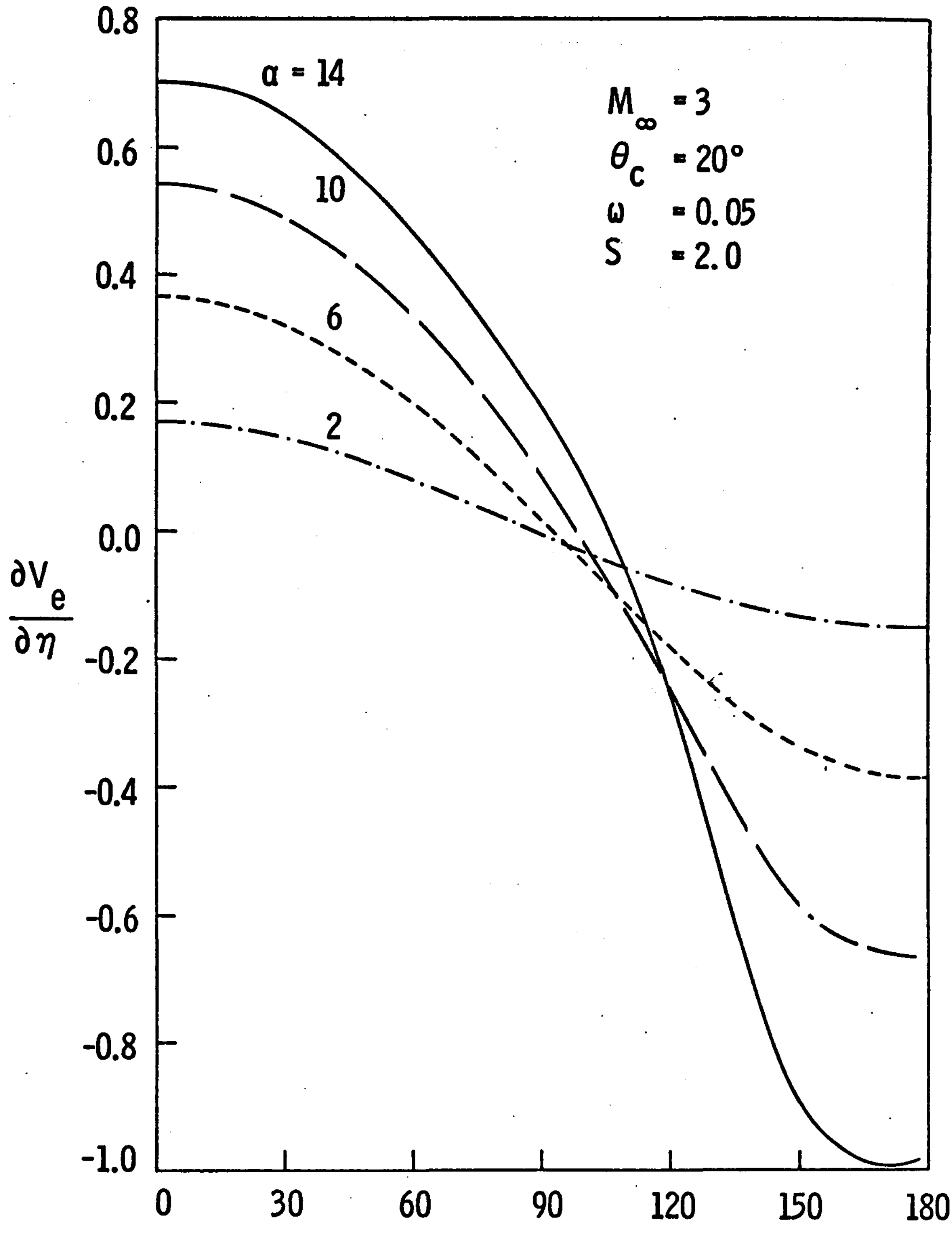

Figure 24. Transverse Cross Flow Derivative Around a Sharp Cone at Varying Angle of Attack in Two-Dimensional Shear Flow at S = 2

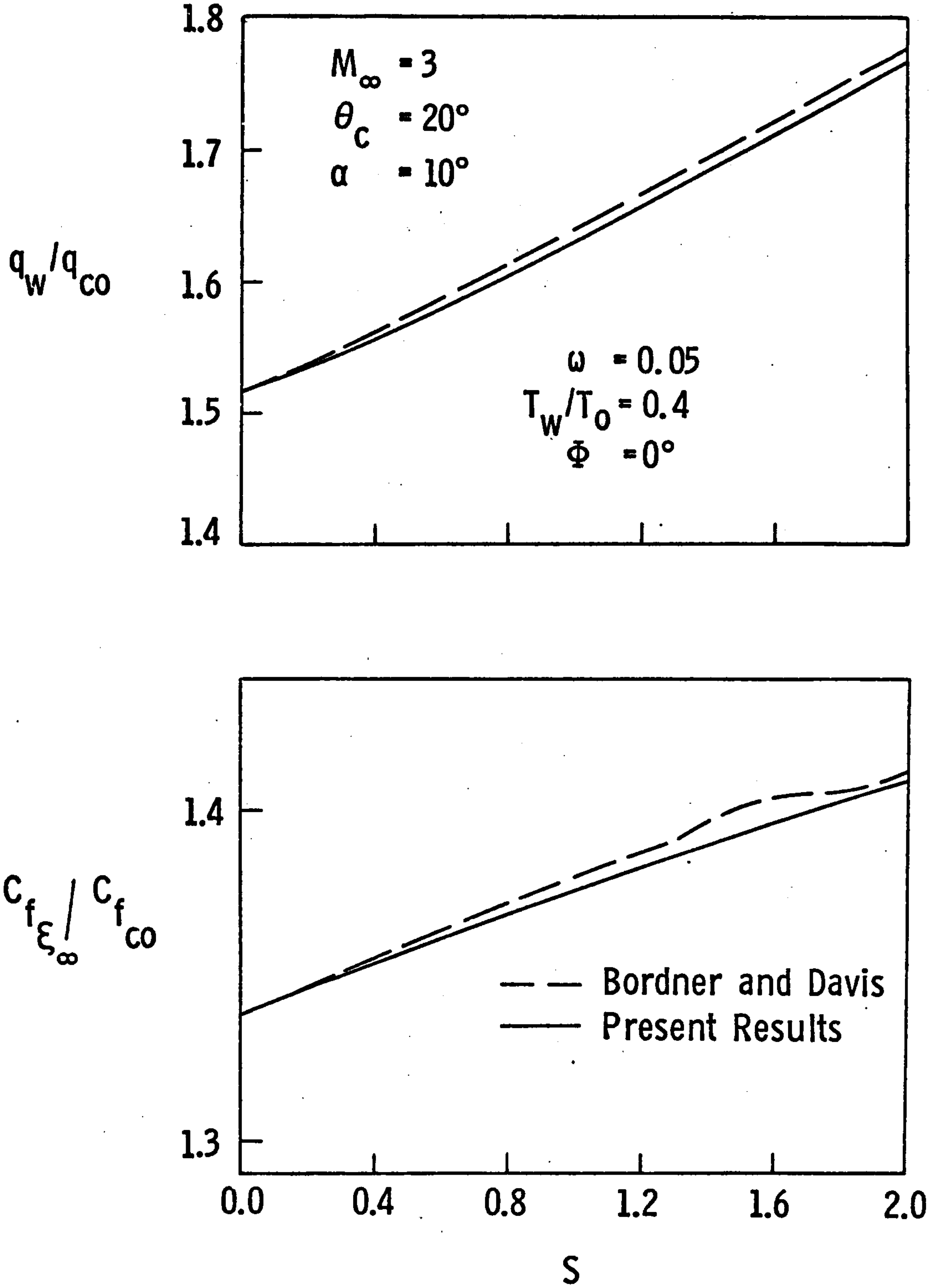

Figure 25. Normalized Heat Transfer and Skin Friction Coefficients Along the Windward Streamline of a Sharp Cone at 10° Angle of Attack in Two-Dimensional Shear Flow: Present Method Compared to Method of Bordner and Davis

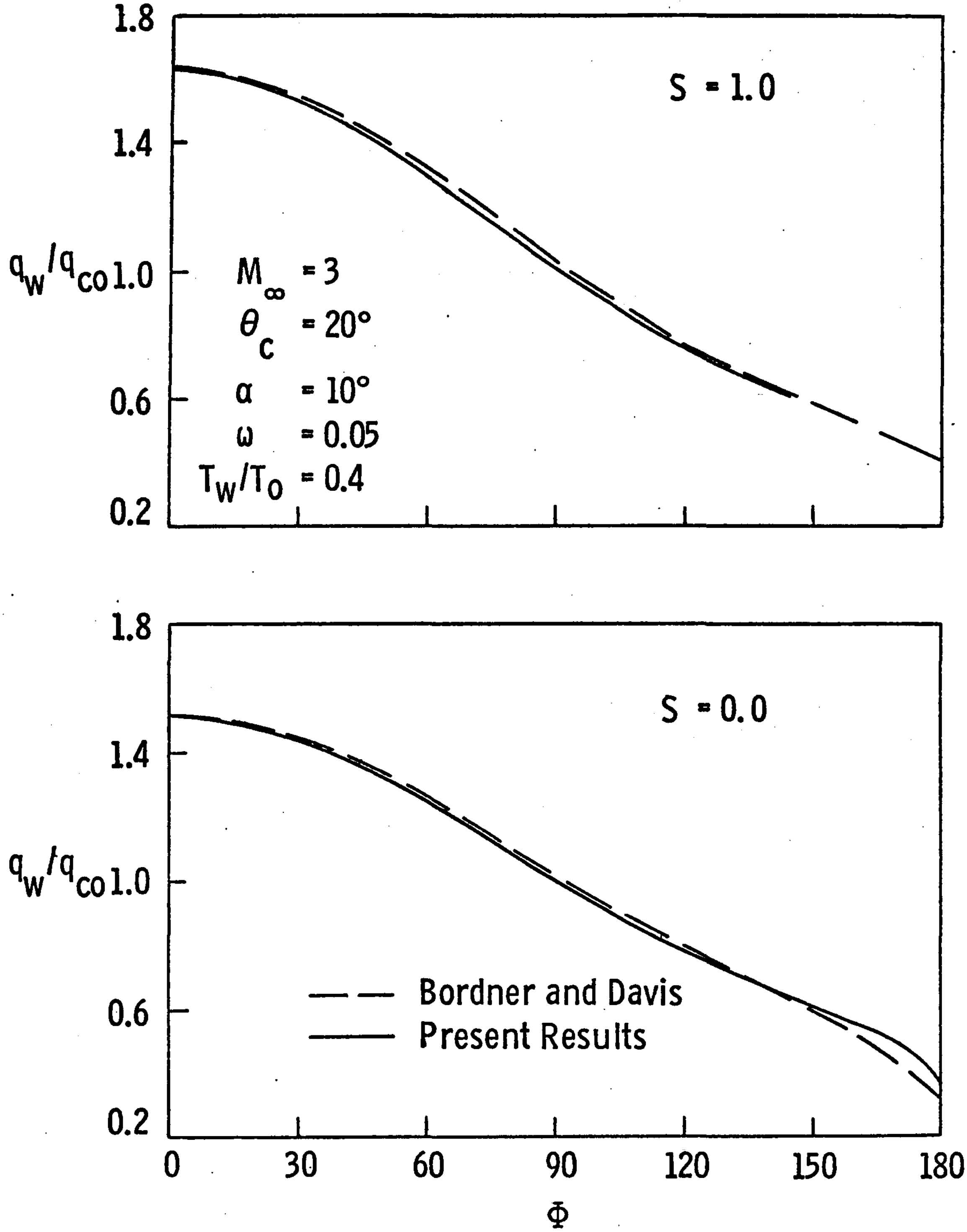

Figure 26. Normalized Heat Transfer Coefficient Around a Sharp Cone at 10^0 Angle of Attack in Two-Dimensional Shear Flow at S = 0 and 1: Present Method Compared to Method of Bordner and Davis

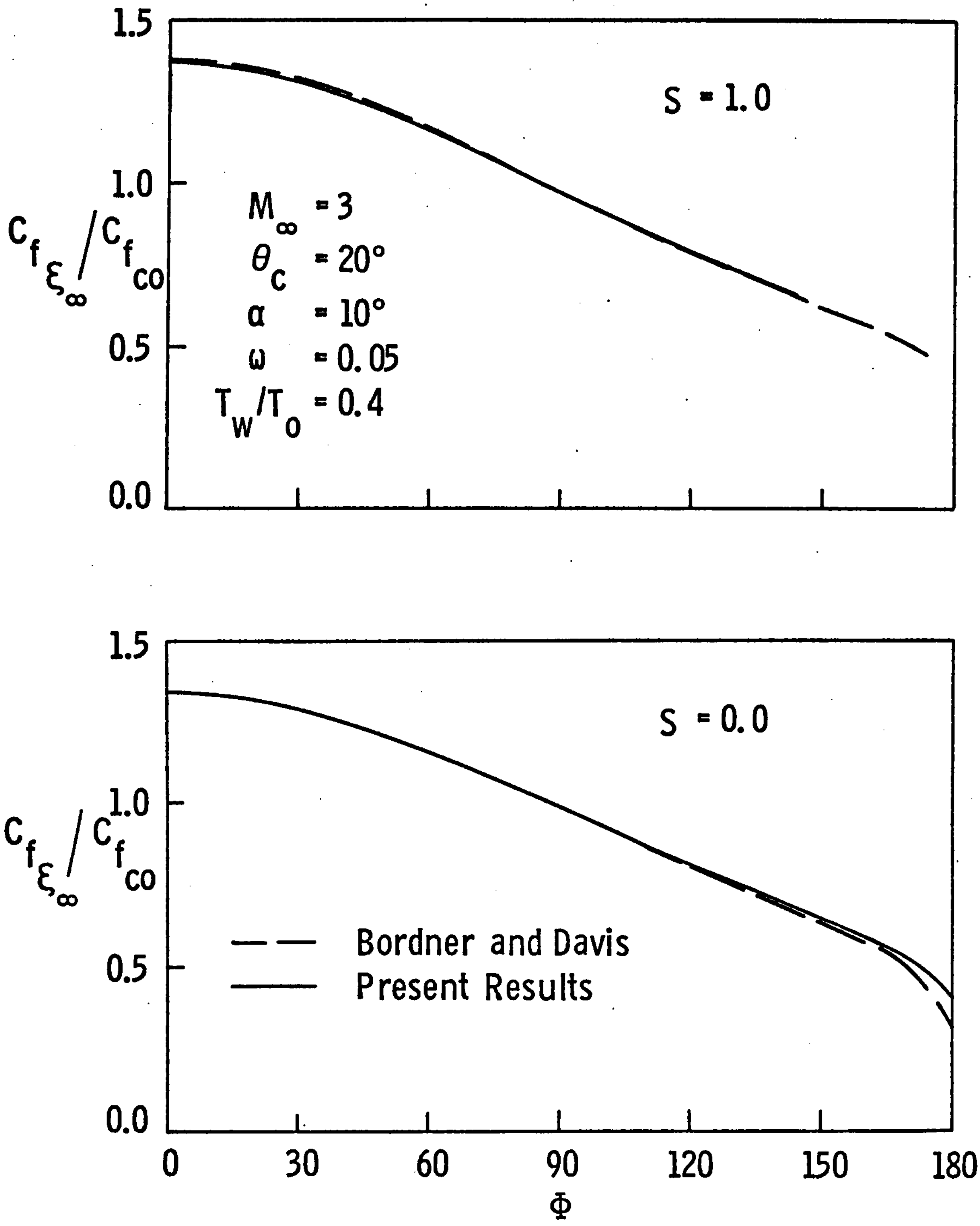

Figure 27. Normalized Skin Friction Coefficient Around a Sharp Cone at 10^{o} Angle of Attack in Two-Dimensional Shear Flow at S = 0 and 1: Present Method Compared to Method of Bordner and Davis

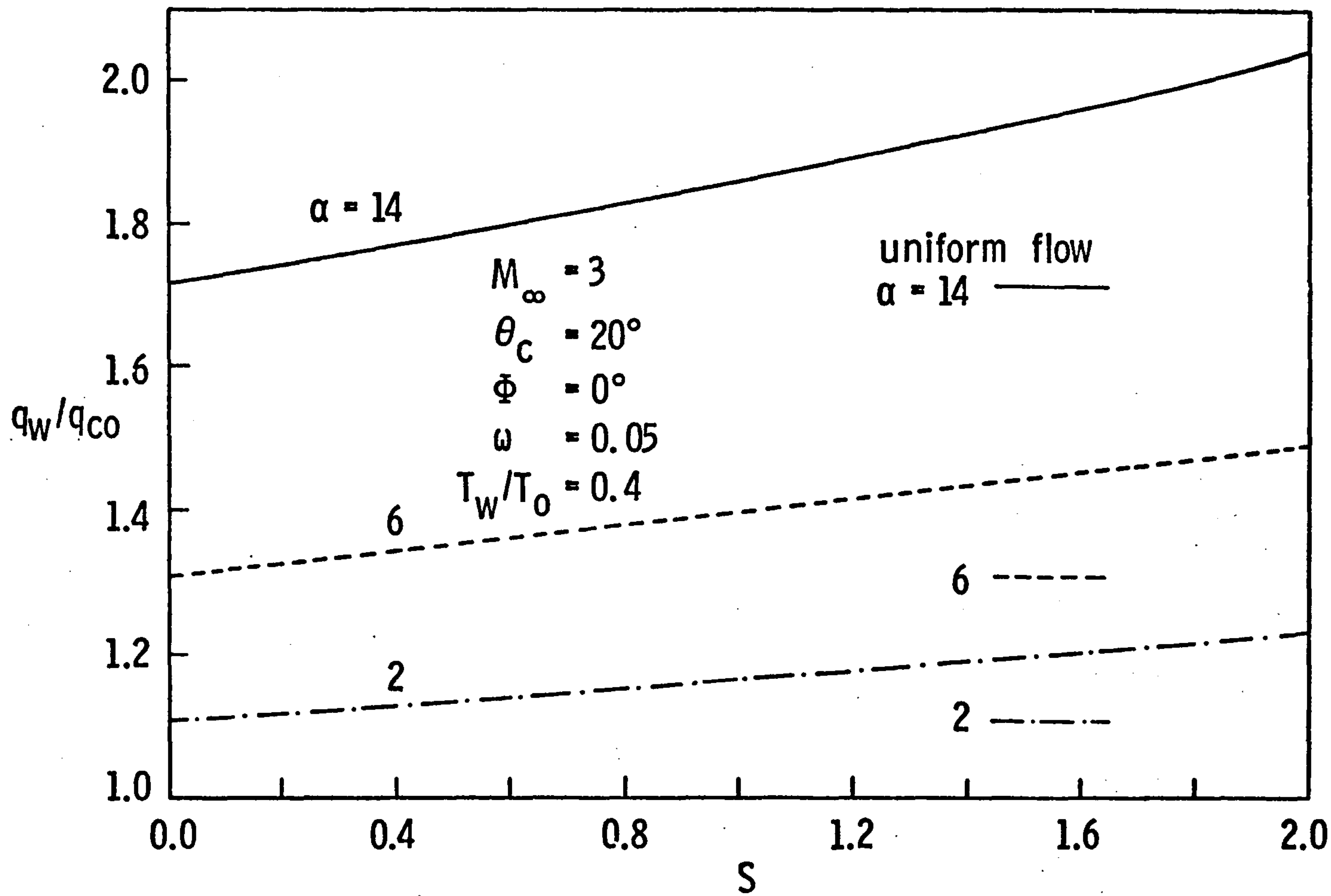

Figure 28. Normalized Heat Transfer Coefficient Along the Windward Streamline of a Sharp Cone at Varying Angle of Attack in Two-Dimensional Shear Flow

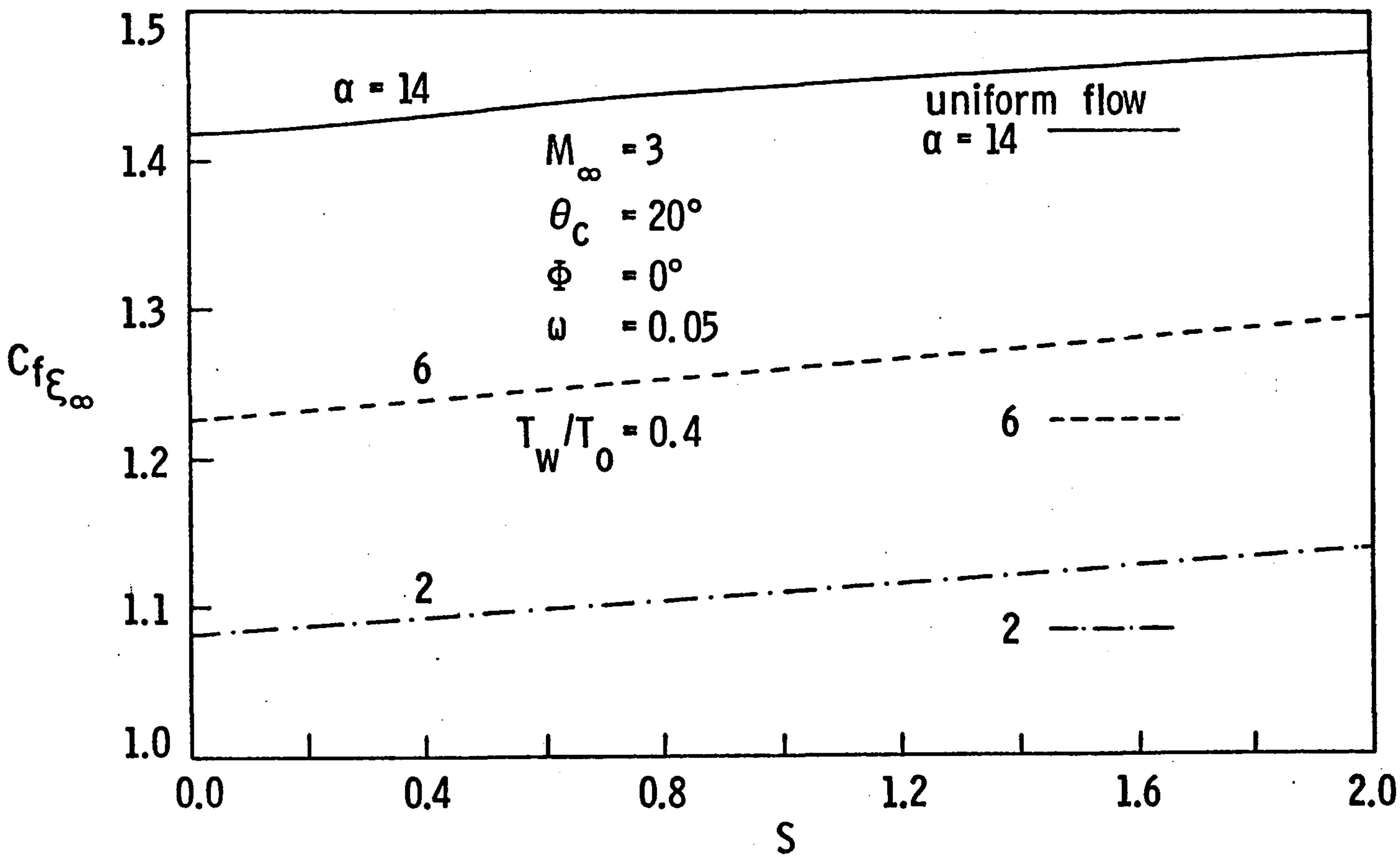

Figure 29. Normalized Skin Friction Coefficient Along the Windward Streamline of a Sharp Cone at Varying Angle of Attack in Two-Dimensional Shear Flow

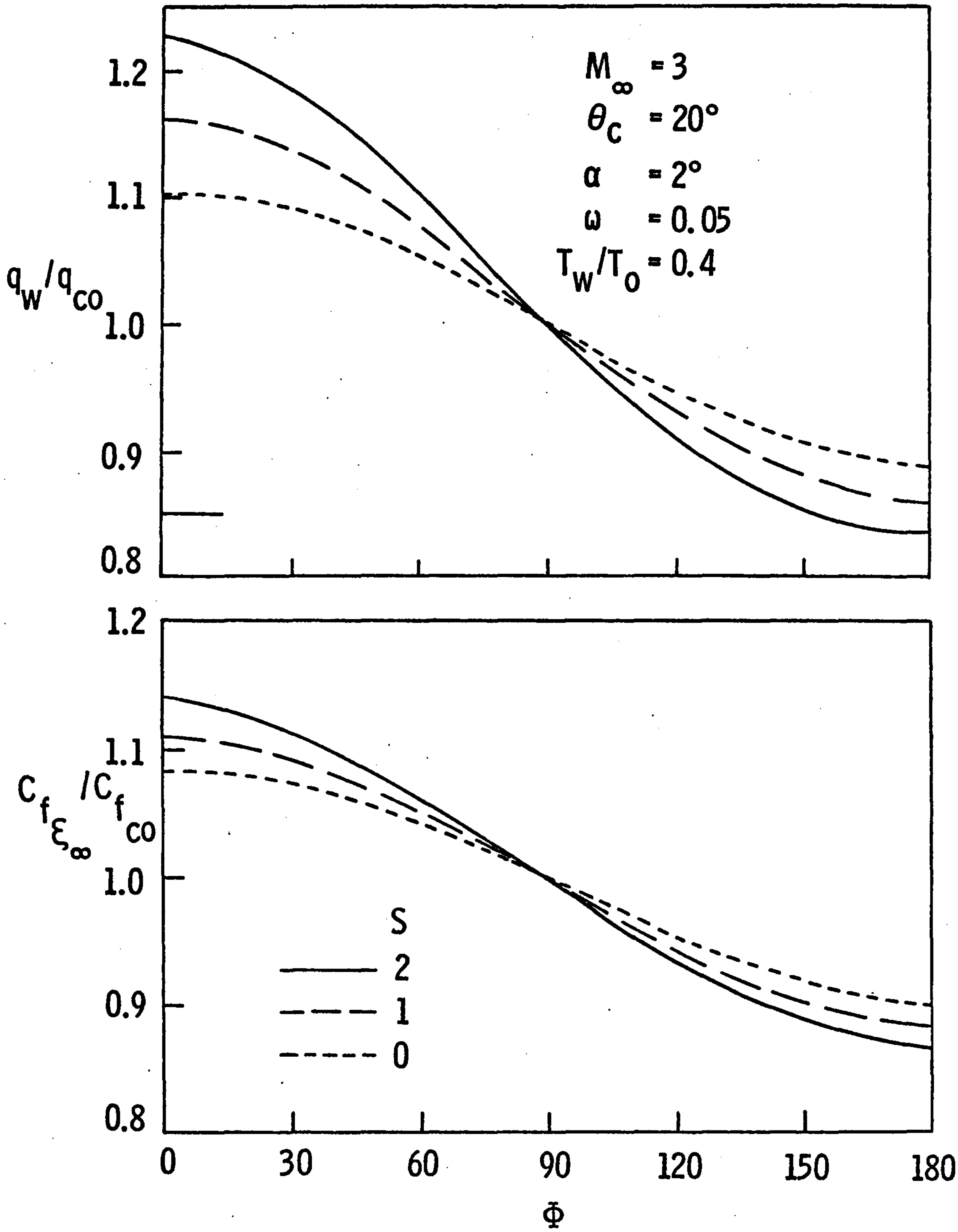

Figure 30. Normalized Heat Transfer and Skin Friction Coefficients Around a Sharp Cone at 2° Angle of Attack in Two-Dimensional Shear Flow at S = 0, 1 and 2

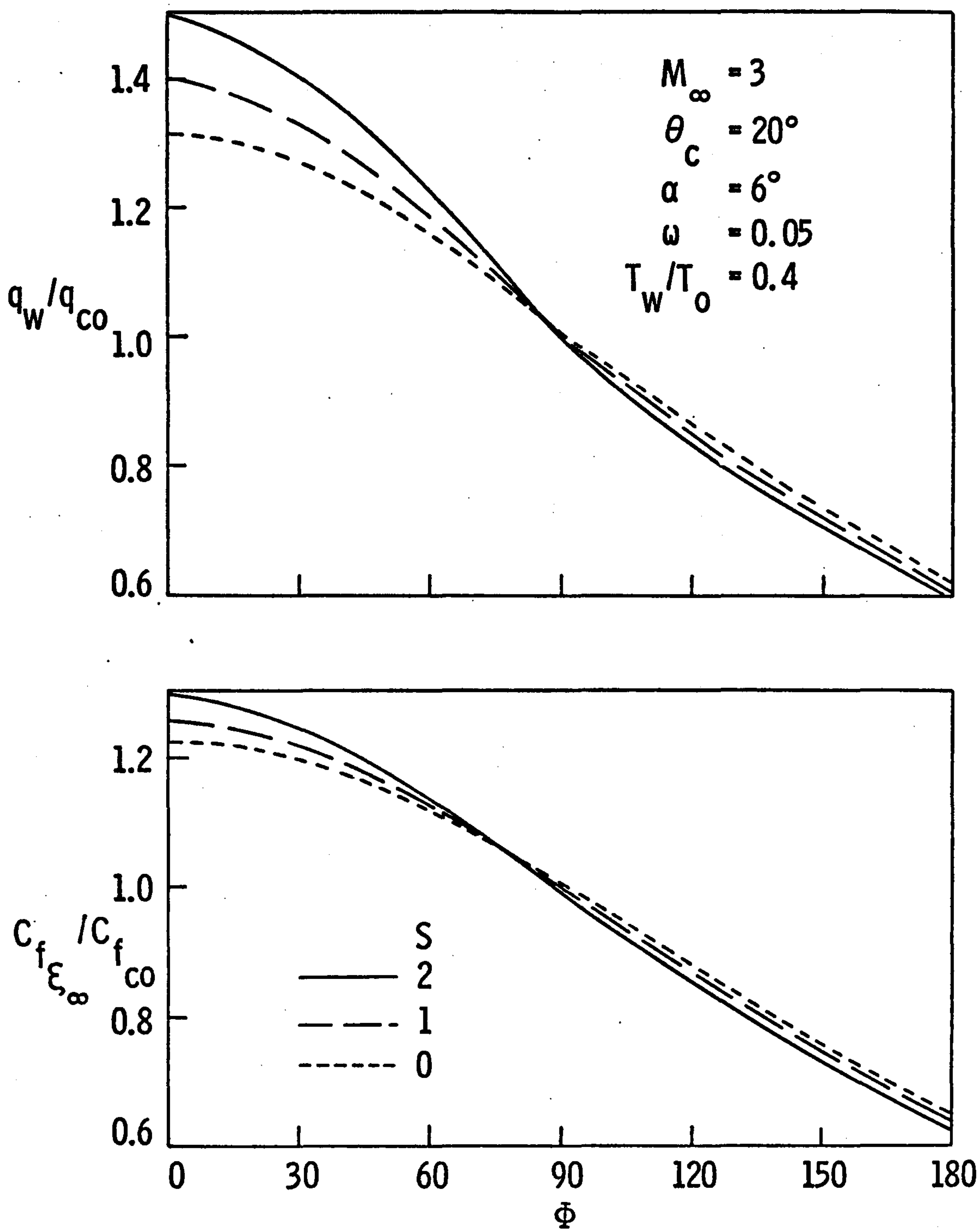

Figure 31. Normalized Heat Transfer and Skin Friction Coefficients Around a Sharp Cone at 6^{o} Angle of Attack in Two-Dimensional Shear Flow at S = 0, 1 and 2

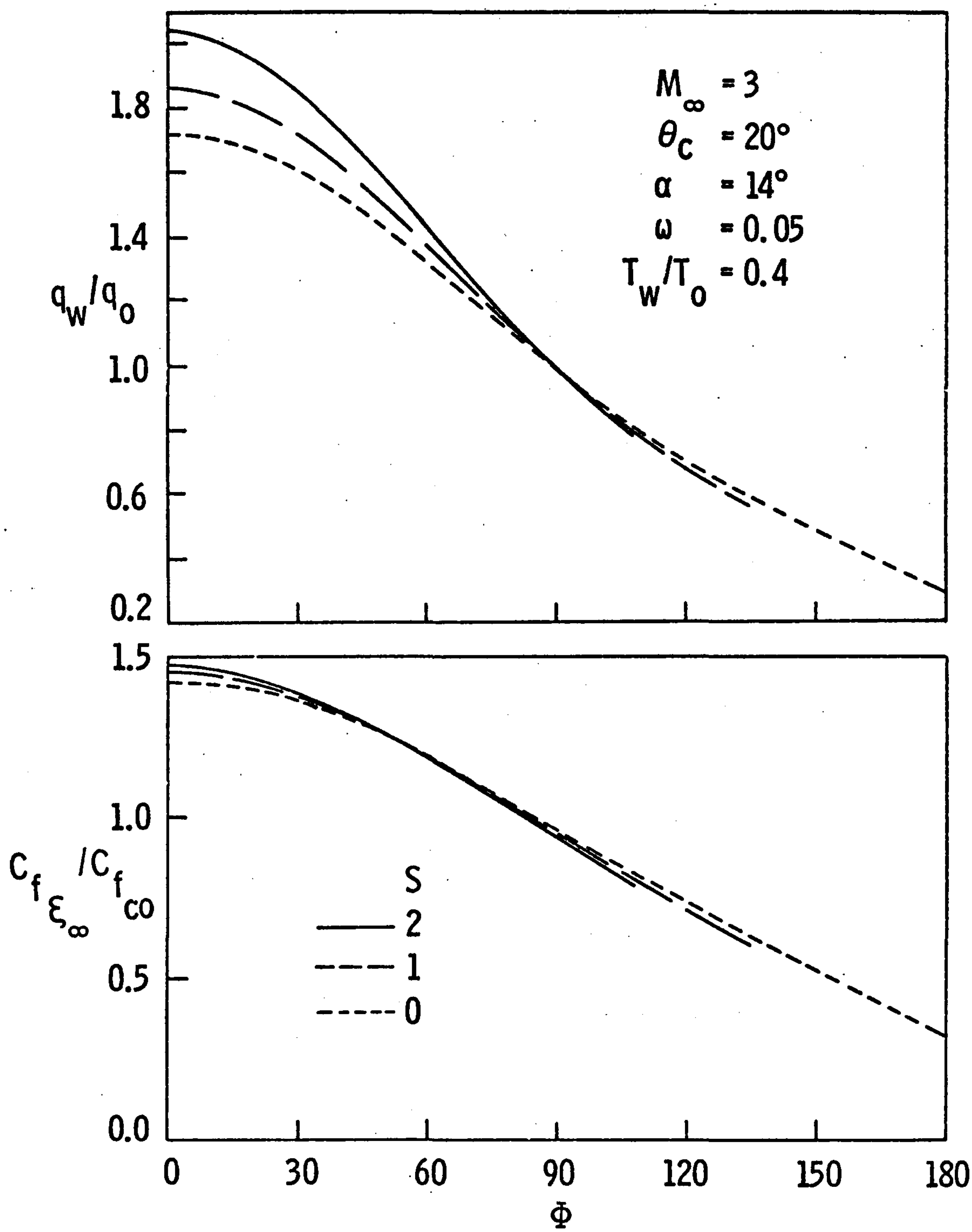

Figure 32. Normalized Heat Transfer and Skin Friction Coefficients Around a Sharp Cone at 14° Angle of Attack in Two-Dimensional Shear Flow at S = 0, 1 and 2

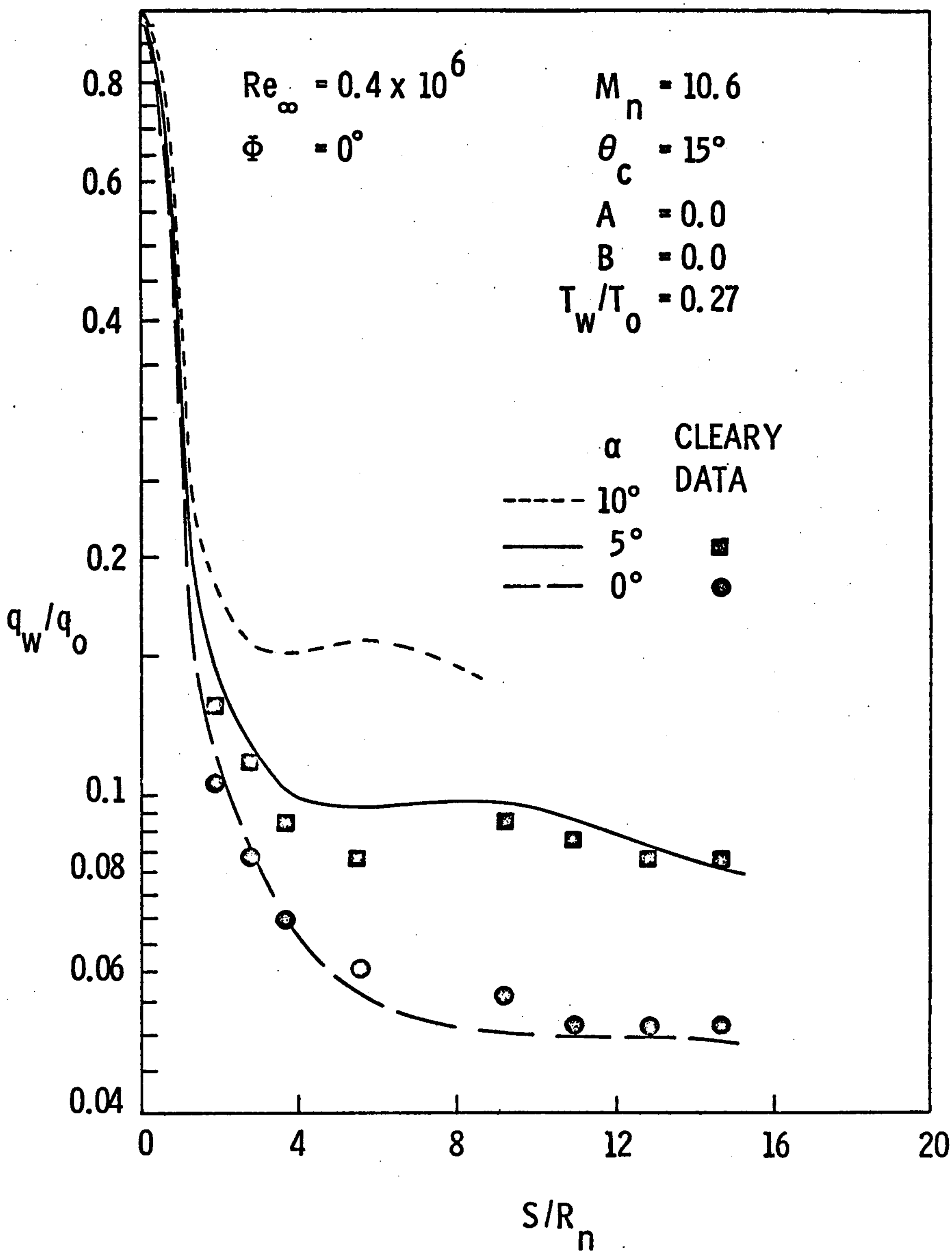

Figure 33. Nondimensional Heat Transfer Rate Along the Windward Streamline of a Blunt Cone at Varying Angle of Attack in Uniform Flow: Present Method Compared to Experiment of Cleary

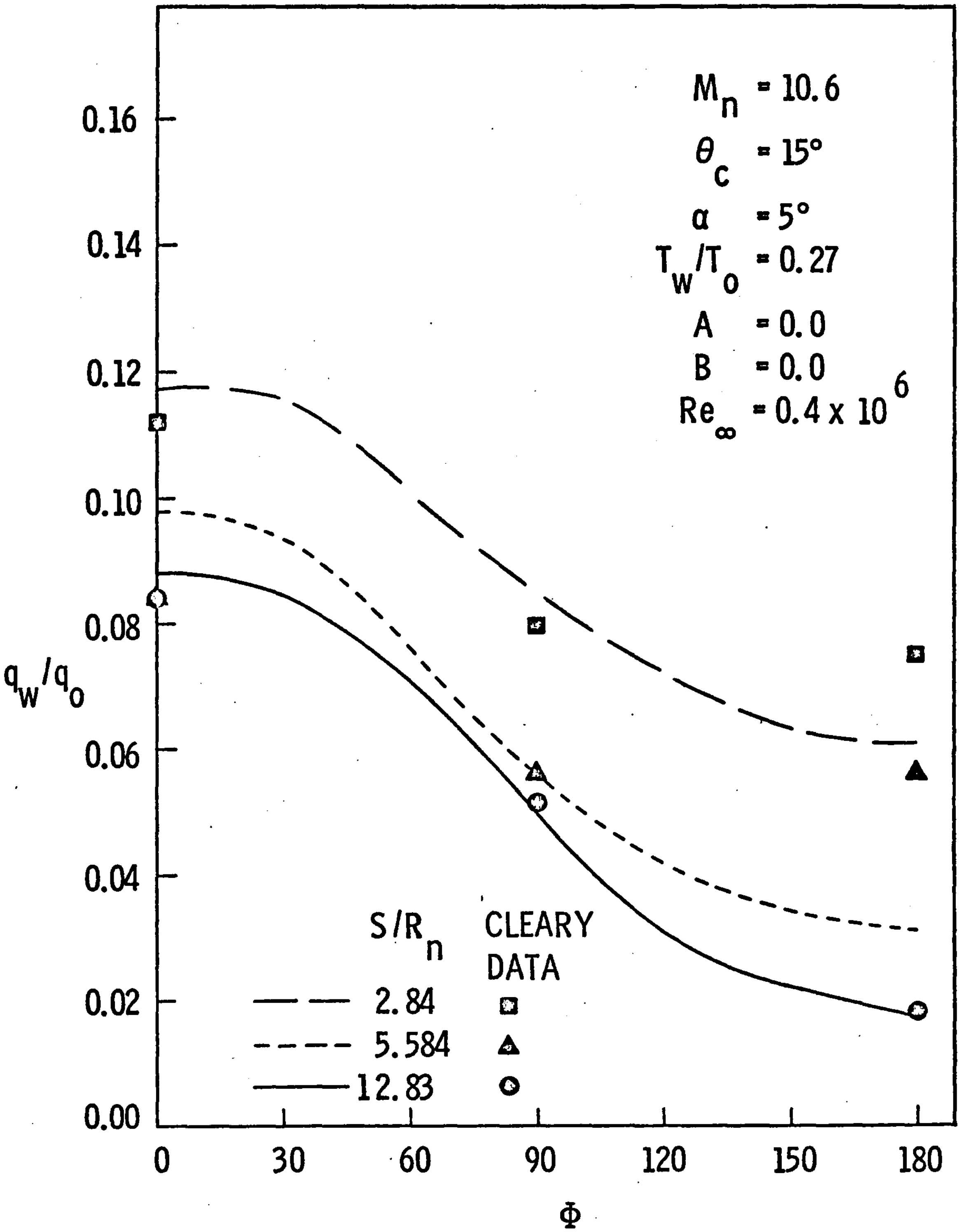

Figure 34. Nondimensional Heat Transfer Rate Around a Blunt Cone at 5° Angle of Attack in Uniform Flow at S/R_n = 2.84, 5.58 and 12.83: Present Method Compared to Experiment of Cleary

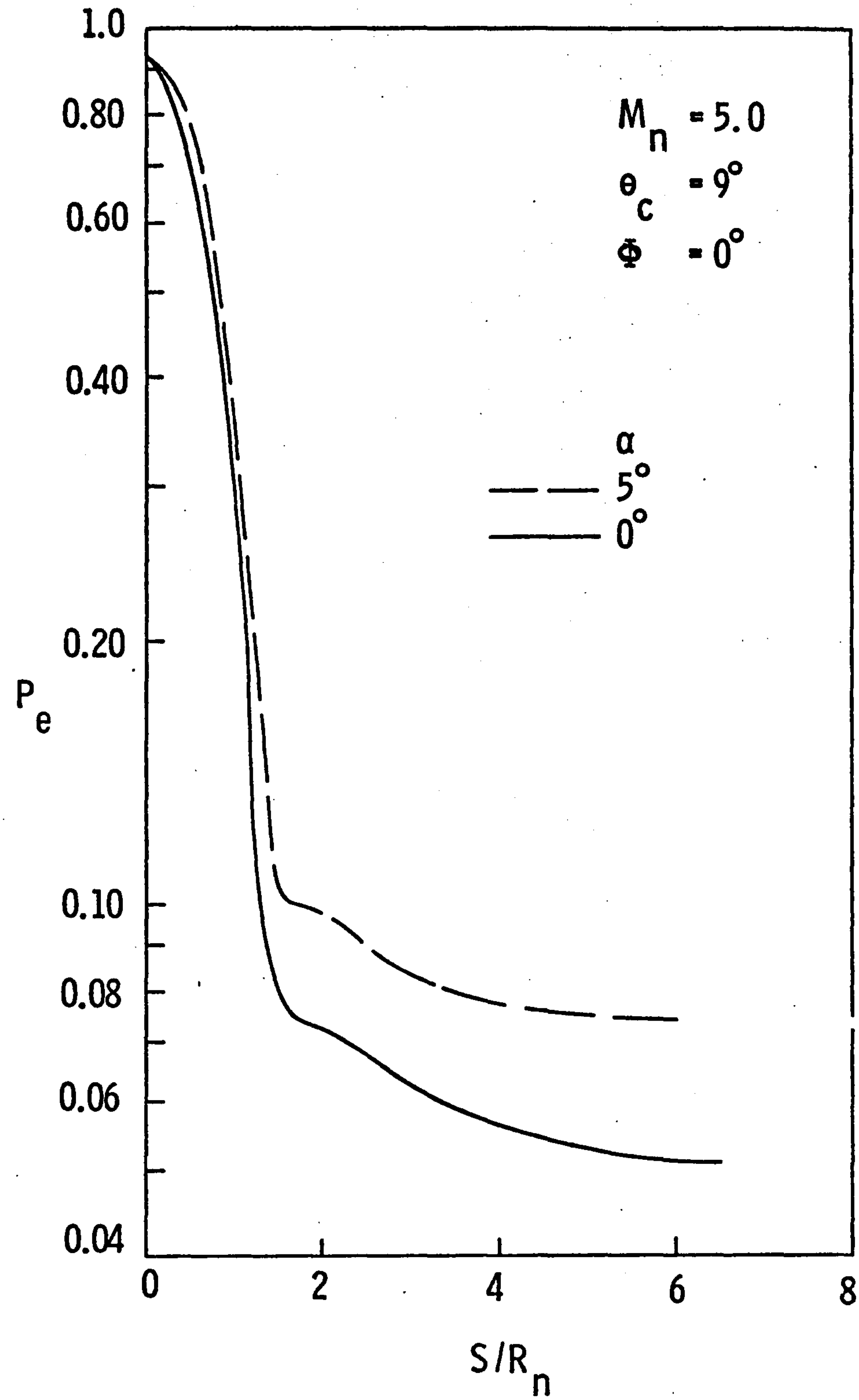

Figure 35. Pressure Distribution Along the Windward Streamline of a Blunt Cone in Uniform Flow at 0° and 5° Angles of Attack

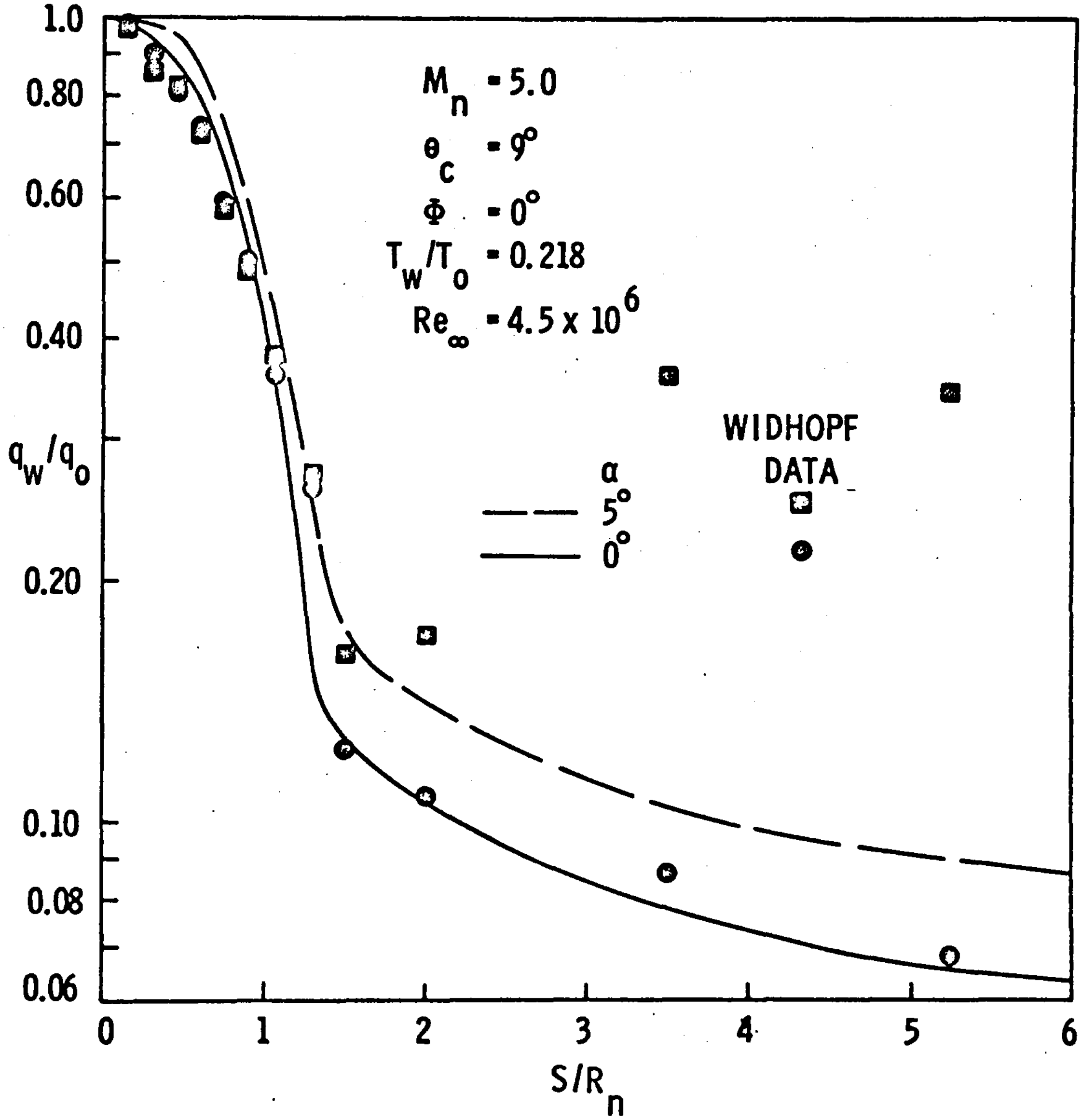

Figure 36. Nondimensional Heat Transfer Rate Along the Windward Streamline of a Blunt Cone at Varying Angle of Attack in Uniform Flow: Present Method Compared to Experiment of Widhopf

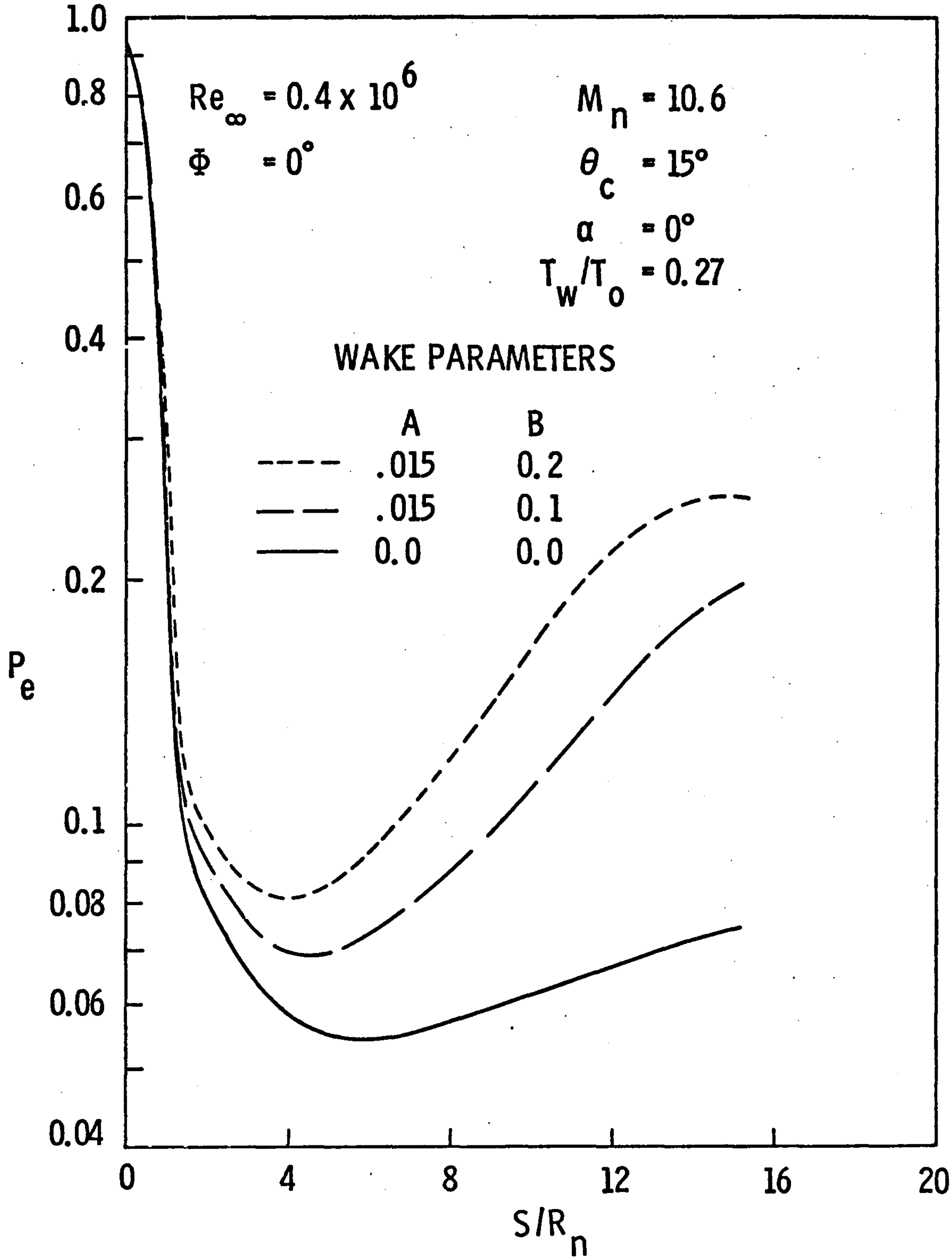

Figure 37. Pressure Distribution Along the Windward Streamline of a Blunt Cone at 0° Angle of Attack in Uniform Flow and Axisymmetric Wake Flows

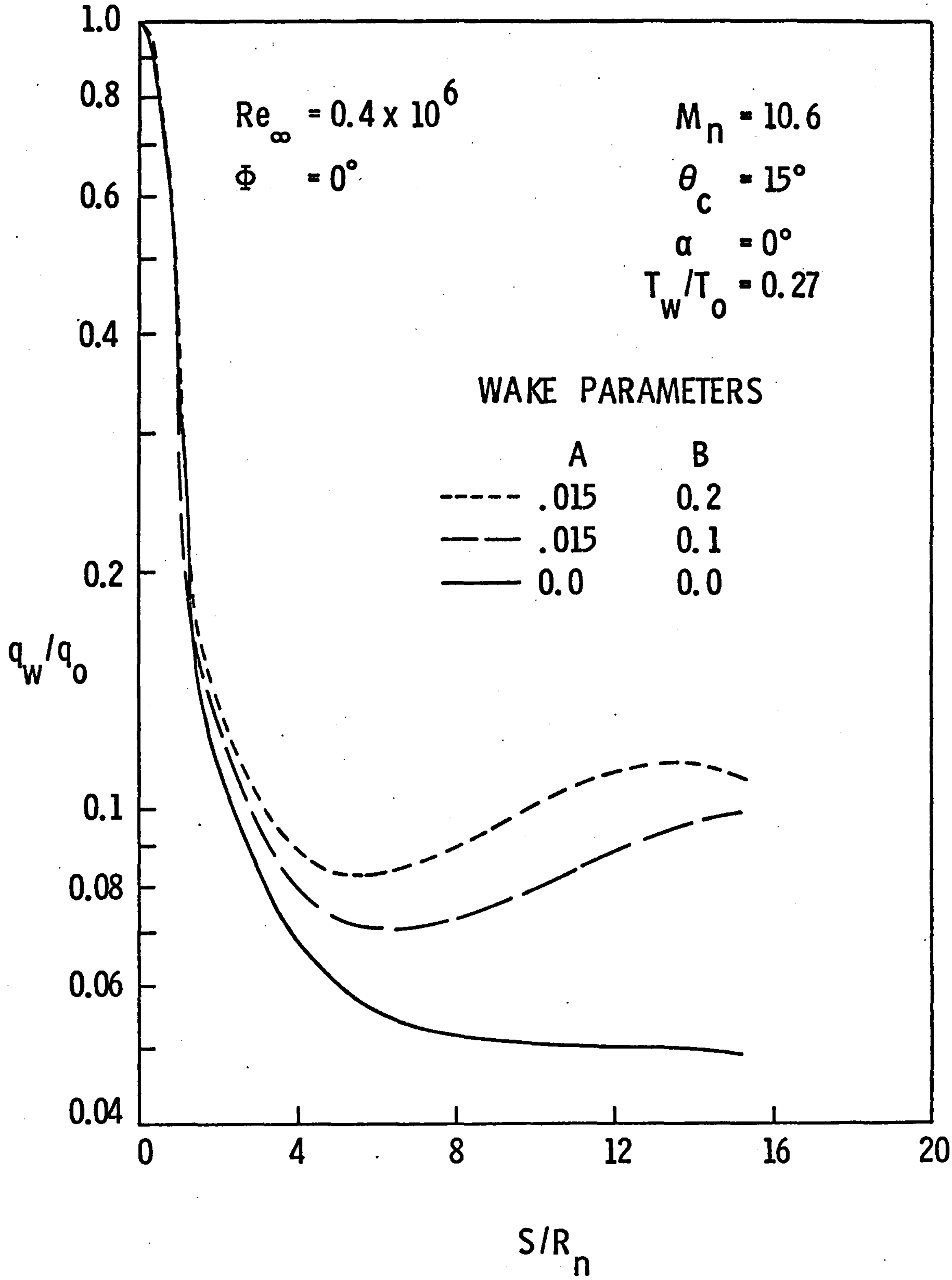

Figure 38. Nondimensional Heat Transfer Rate Along the Windward Streamline of a Blunt Cone at 0° Angle of Attack in Uniform Flow and Axisymmetric Wake Flows

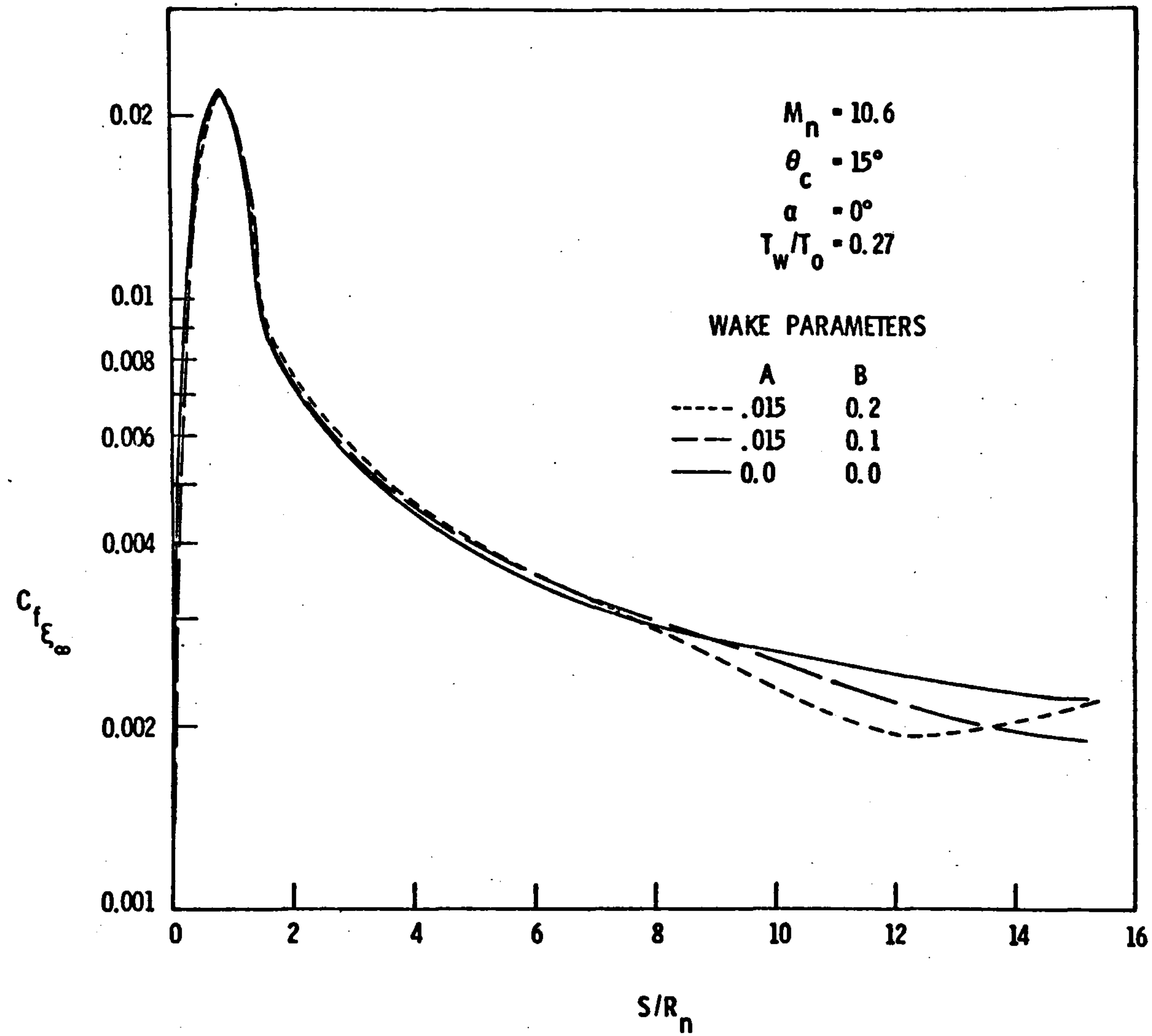

Figure 39. Longitudinal Skin Friction Coefficient Along the Windward Streamline of a Blunt Cone at 0° Angle of Attack in Uniform Flow and Axisymmetric Wake Flows

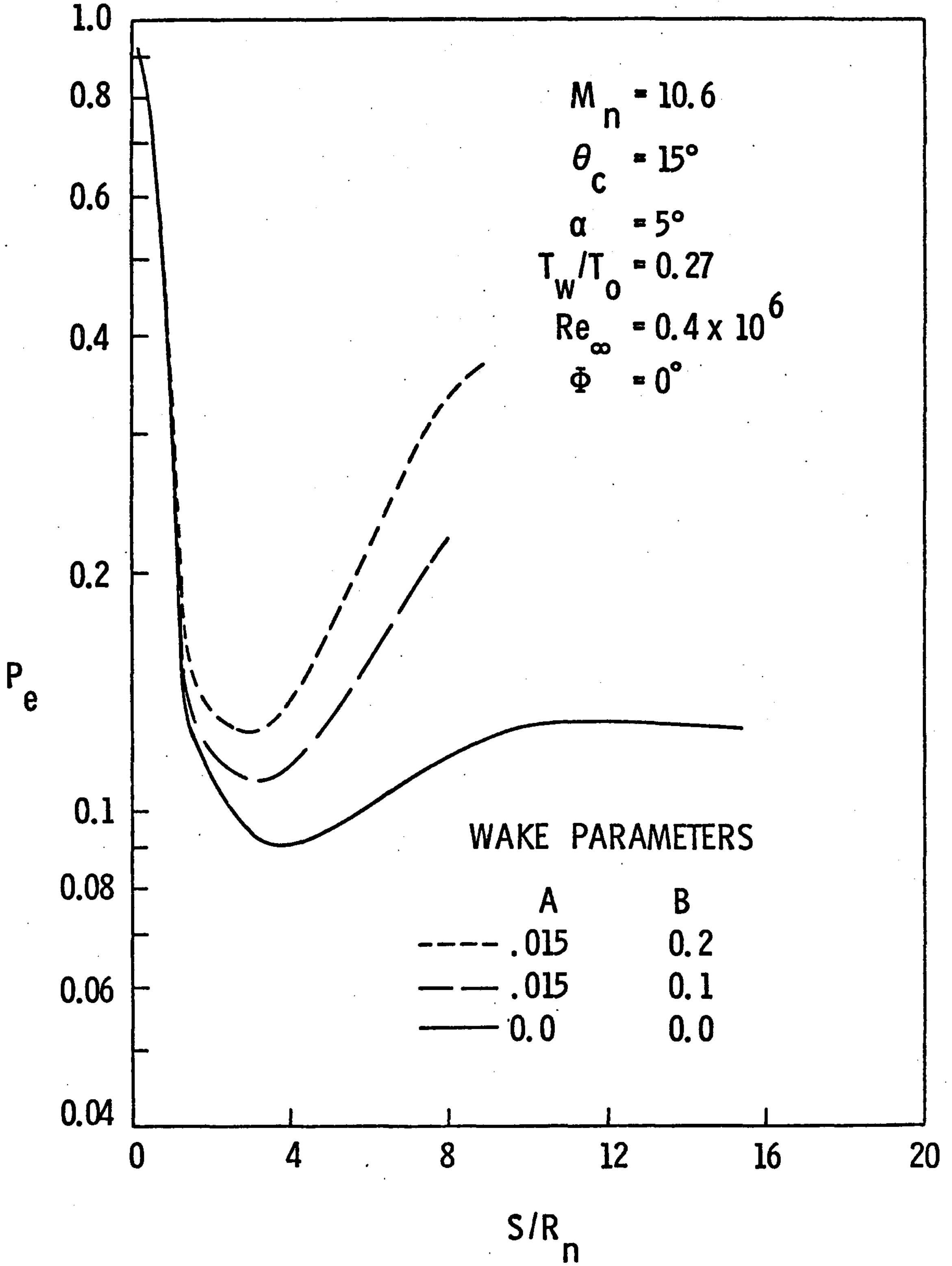

Figure 40. Pressure Distribution Along the Windward Streamline of a Blunt Cone at 5° Angle of Attack in Uniform Flow and Axisymmetric Wake Flows

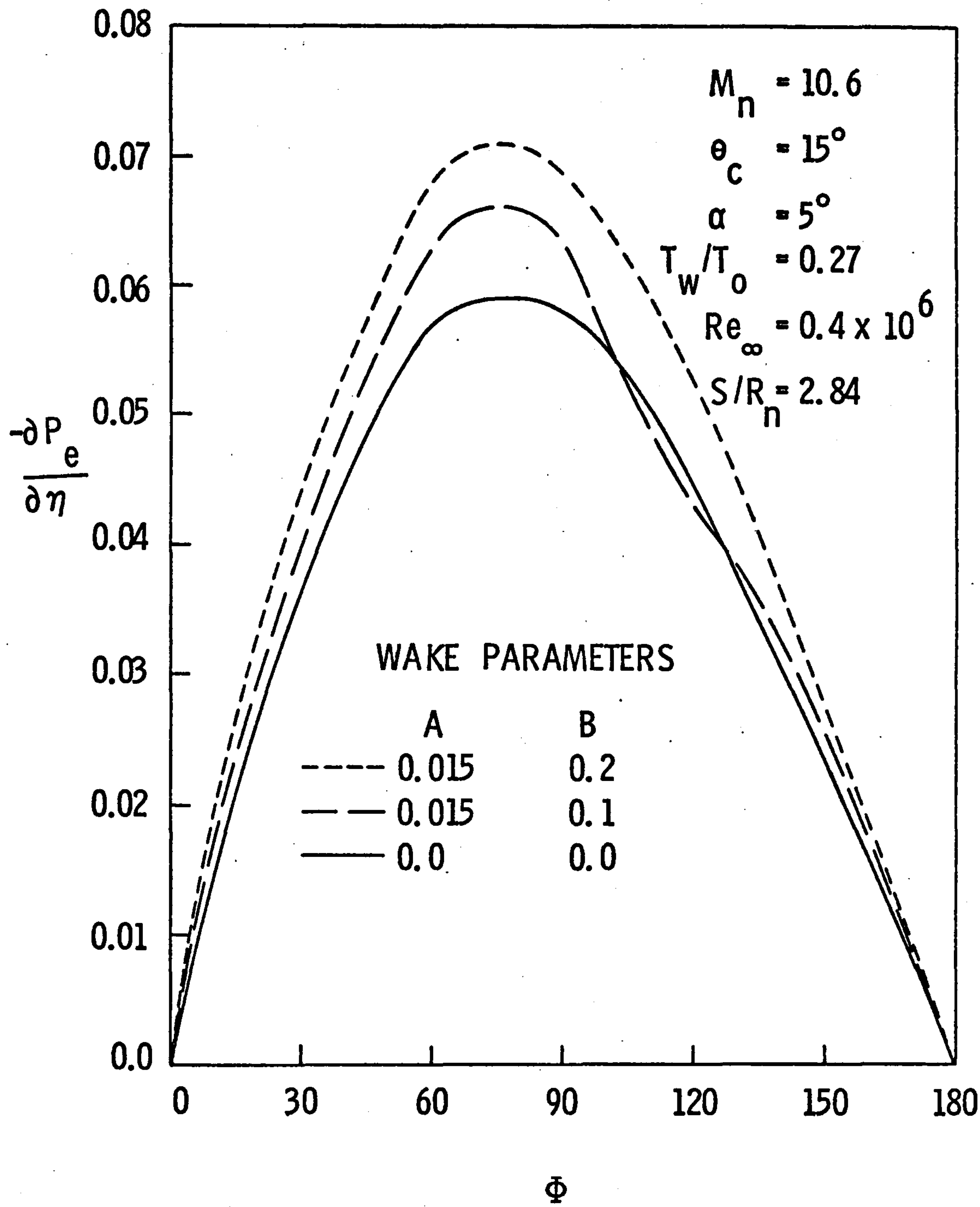

Figure 41. Transverse Pressure Gradient Around a Blunt Cone at 5° Angle of Attack in Uniform Flow and Axisymmetric Wake Flows at S/R_n = 2.84

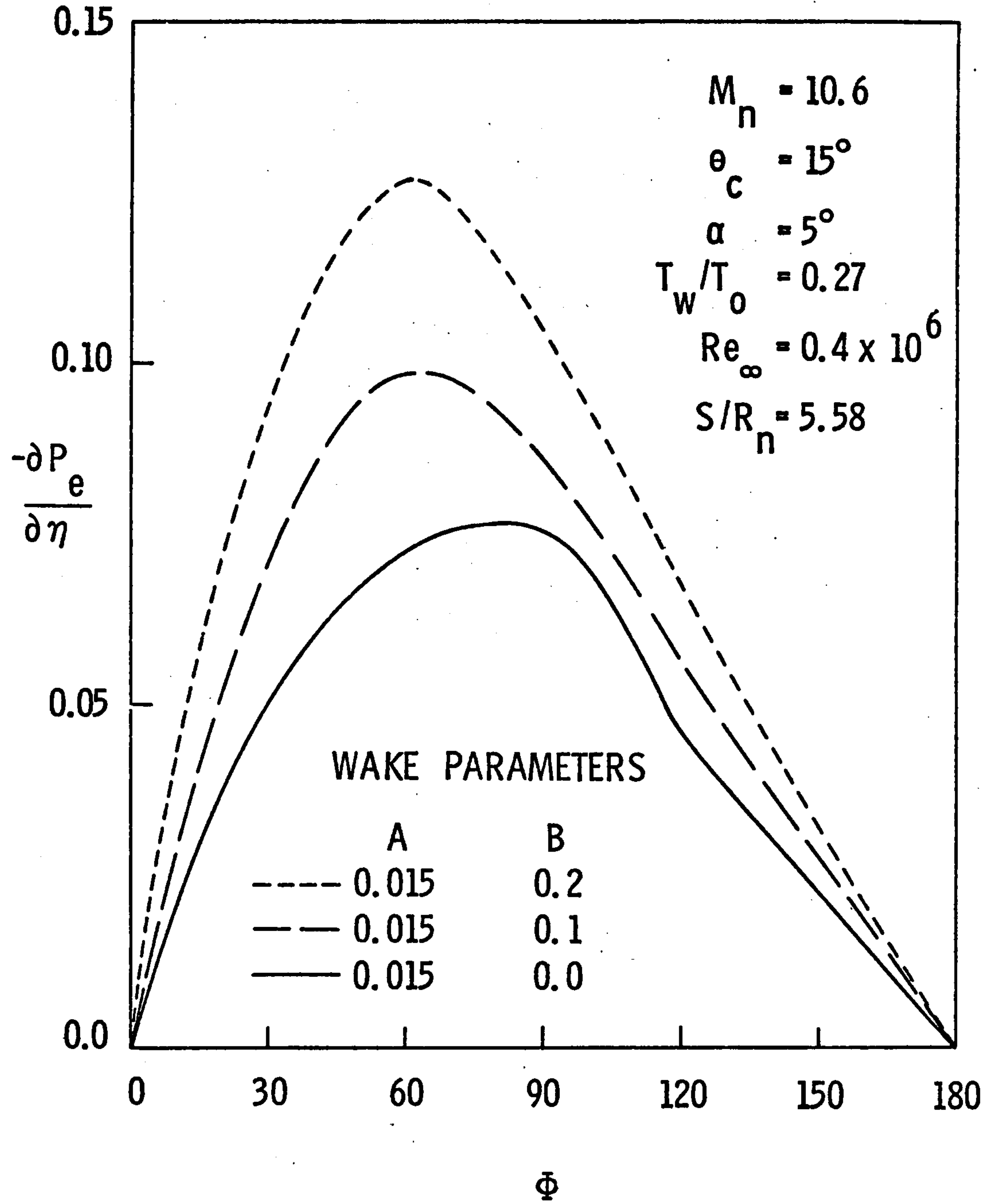

Figure 42. Transverse Pressure Gradient Around a Blunt Cone at 5° Angle of Attack in Uniform Flow and Axisymmetric Wake Flows at $S/R_n = 5.58$

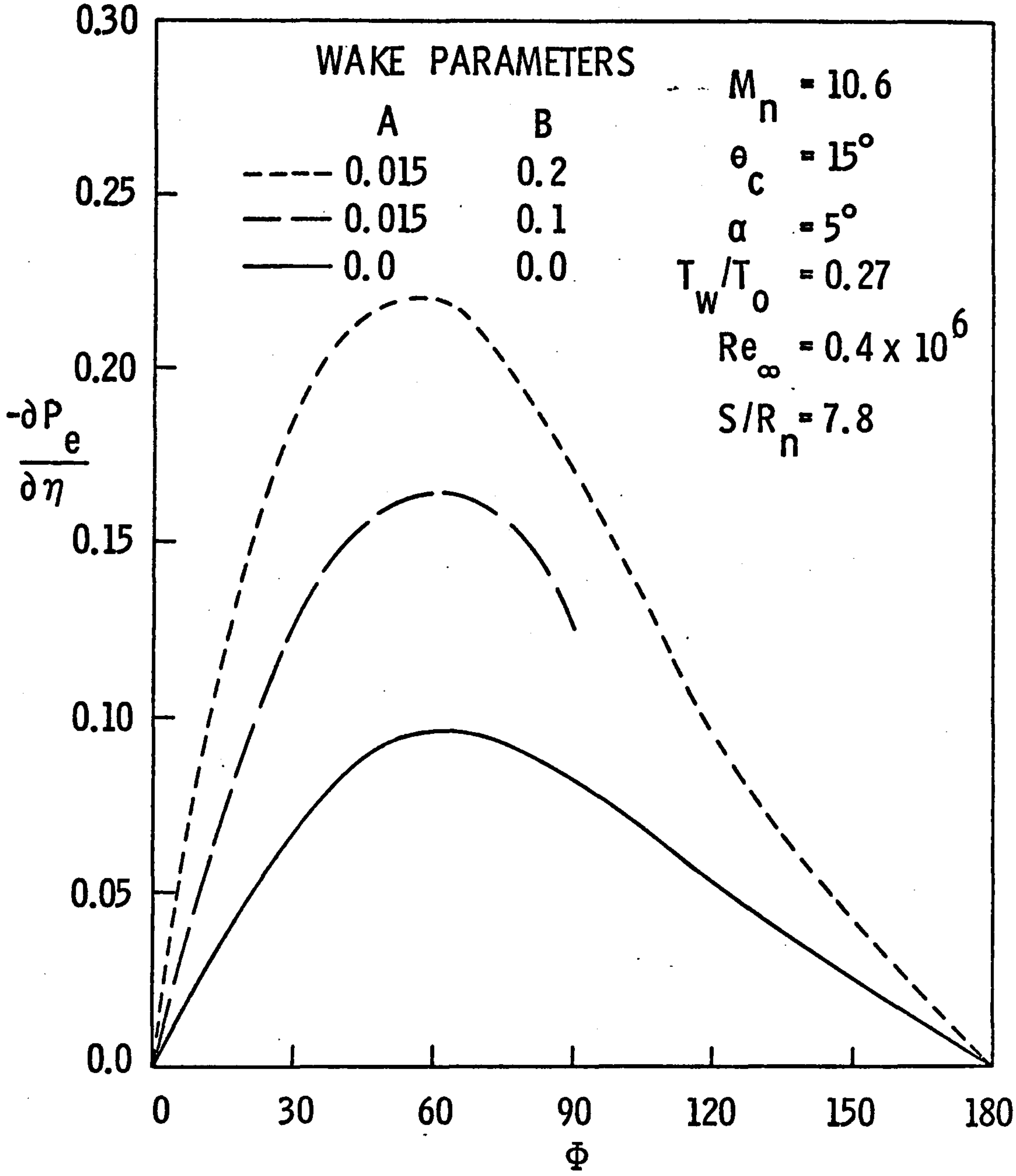

Figure 43. Transverse Pressure Gradient Around a Blunt Cone at 5° Angle of Attack in Uniform Flow and Axisymmetric Wake Flows at S/R_n = 7.8

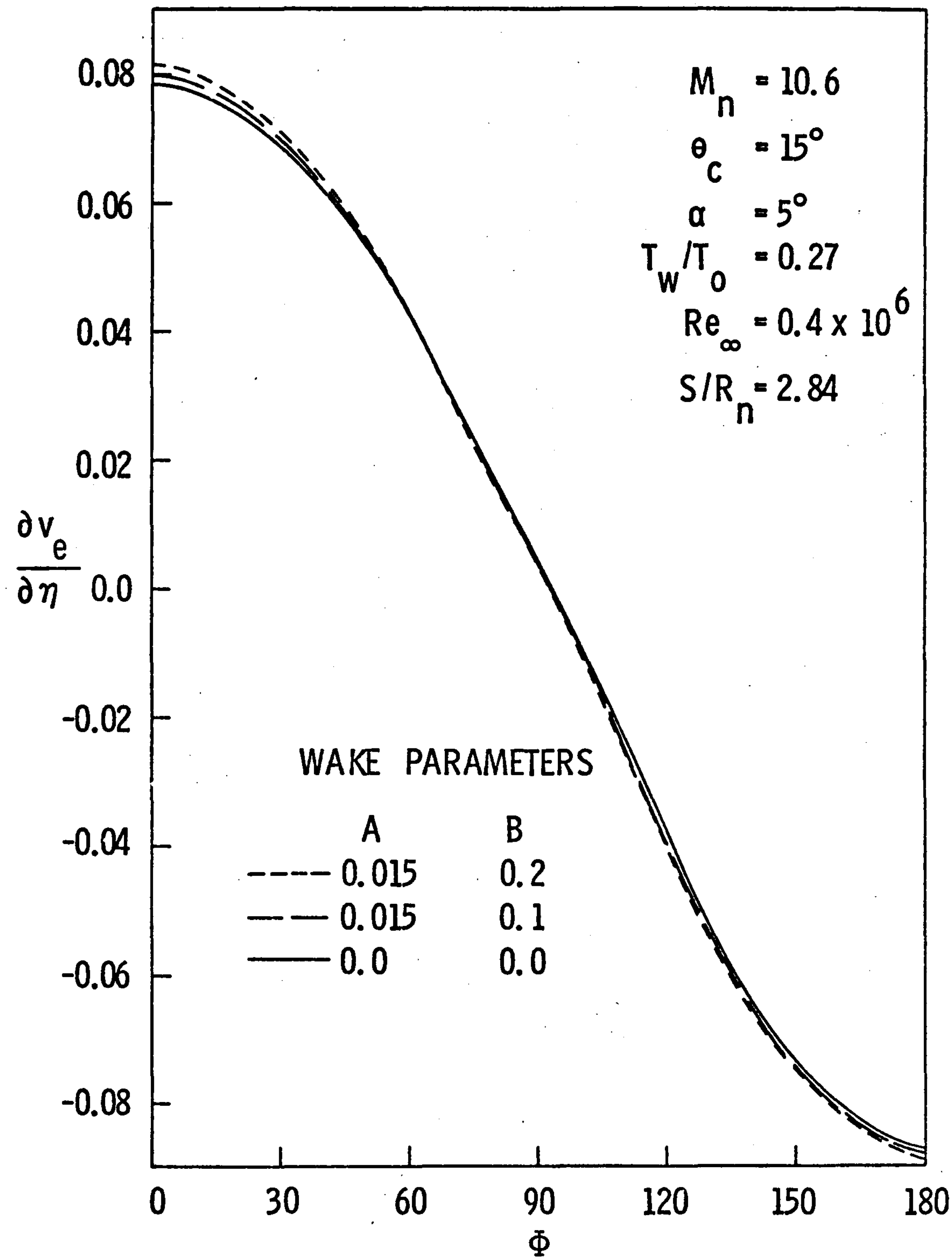

Figure 44. Cross Flow Velocity Derivative Around a Blunt Cone at 5° Angle of Attack in Uniform Flow and Axisymmetric Wake Flows at S/R_n = 2.84

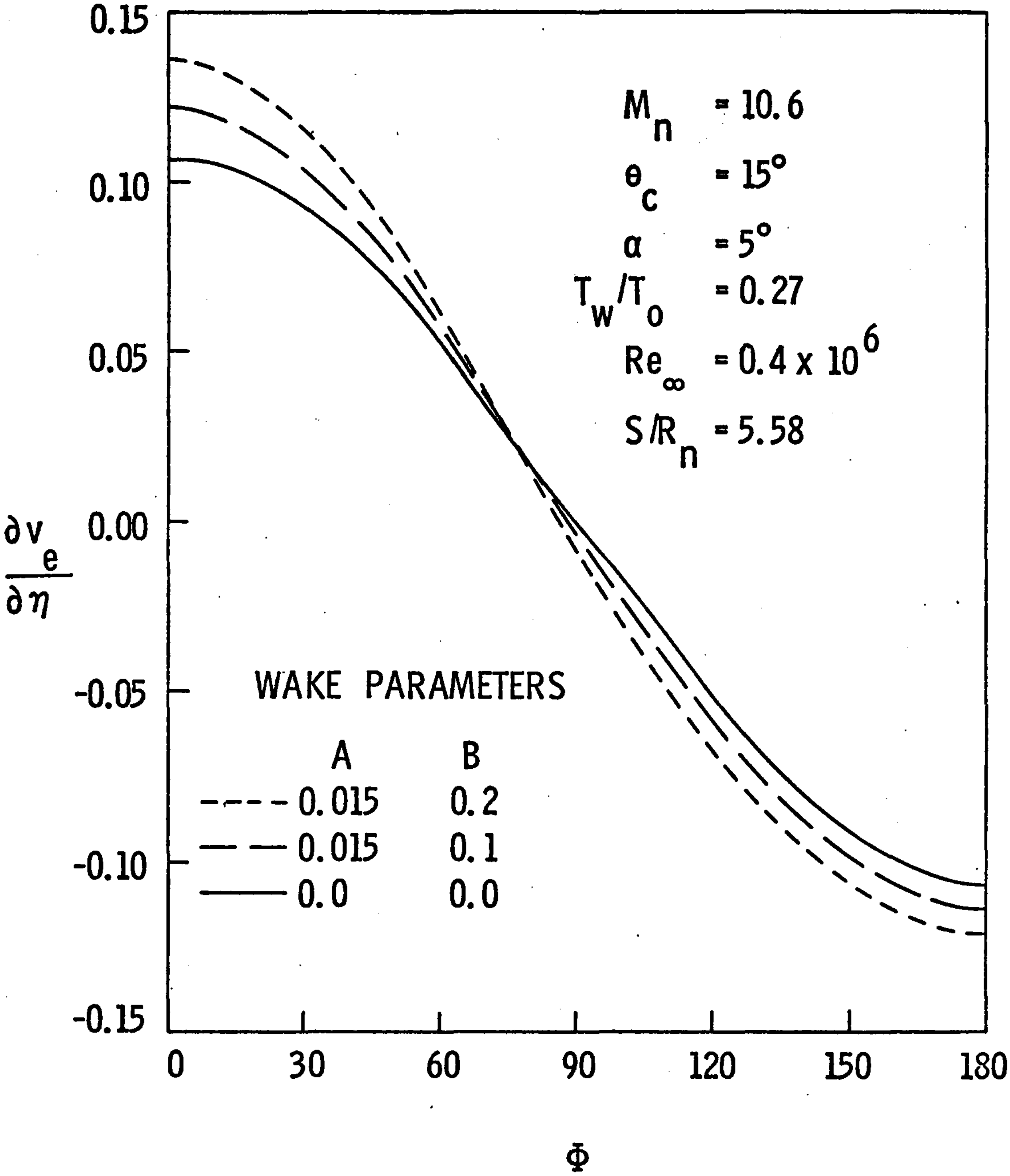

Figure 45. Cross Flow Velocity Derivative Around a Blunt Cone at 5° Angle of Attack in Uniform Flow and Axisymmetric Wake Flows at S/R_n = 5.58

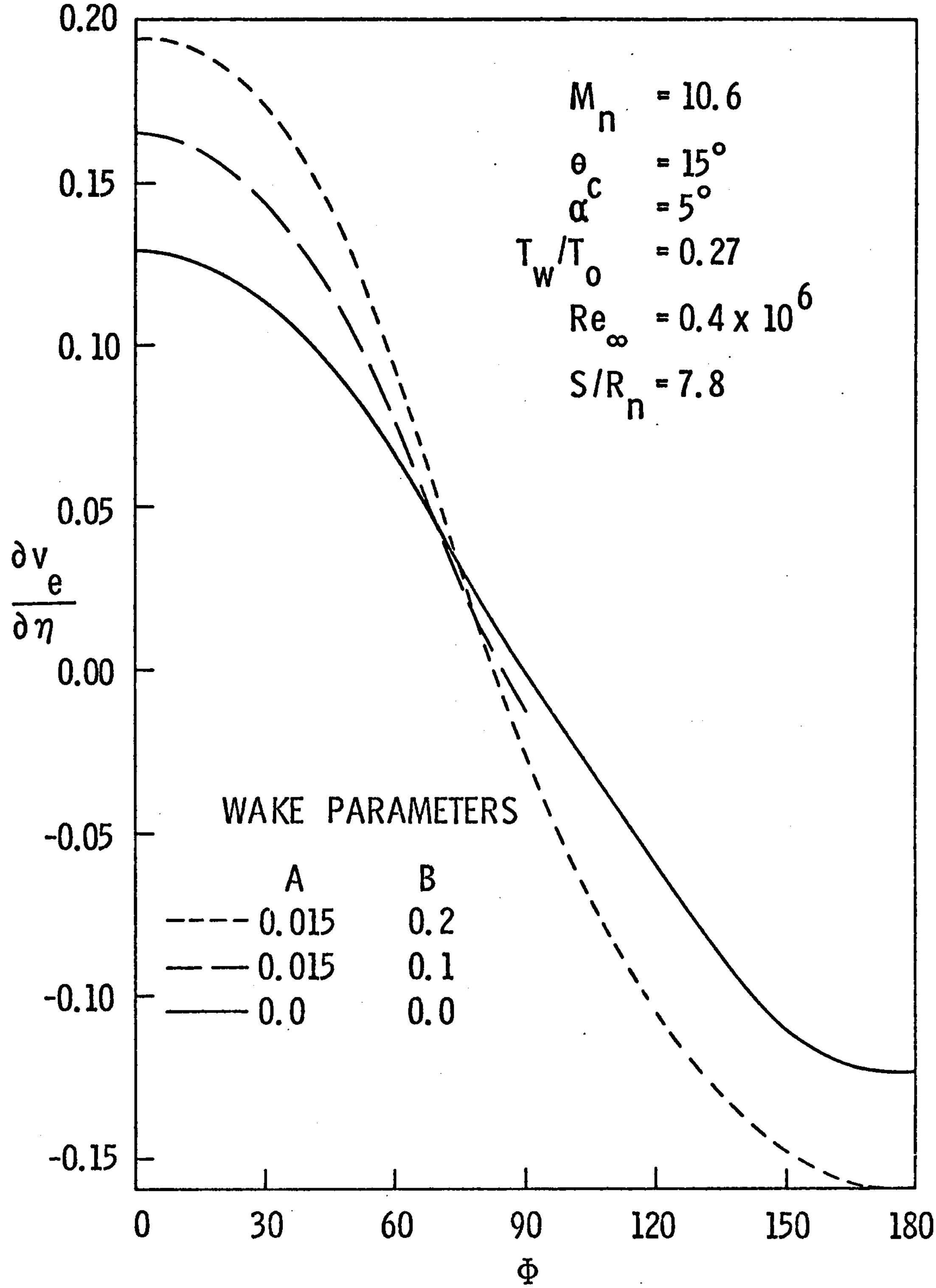

Figure 46. Cross Flow Velocity Derivative Around a Blunt Cone at 5° Angle of Attack in Uniform Flow and Axisymmetric Wake Flows at S/R_n = 7.8

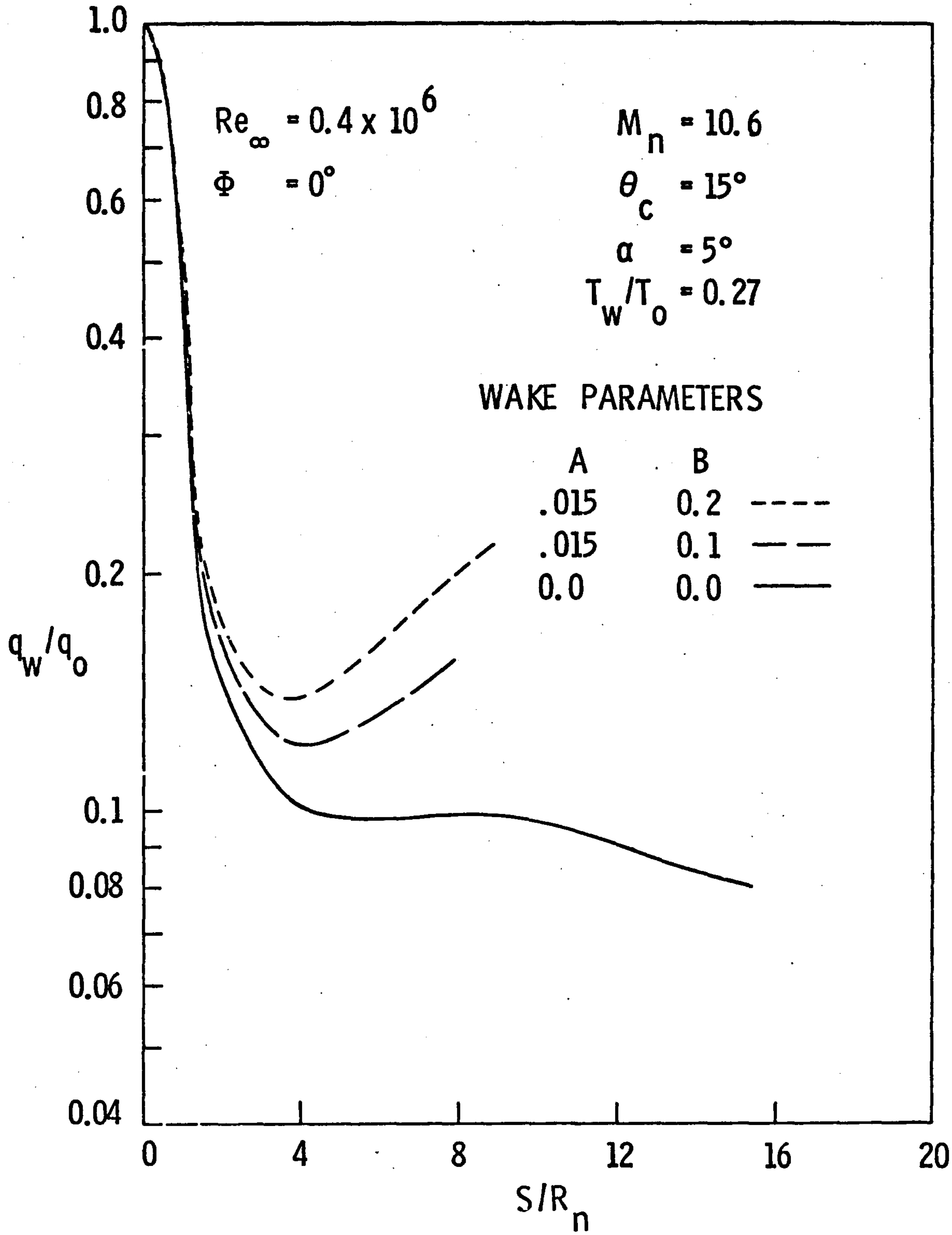

Figure 47. Nondimensional Heat Transfer Rate Along the Windward Streamline of a Blunt Cone at 5° Angle of Attack in Uniform Flow and Axisymmetric Wake Flows

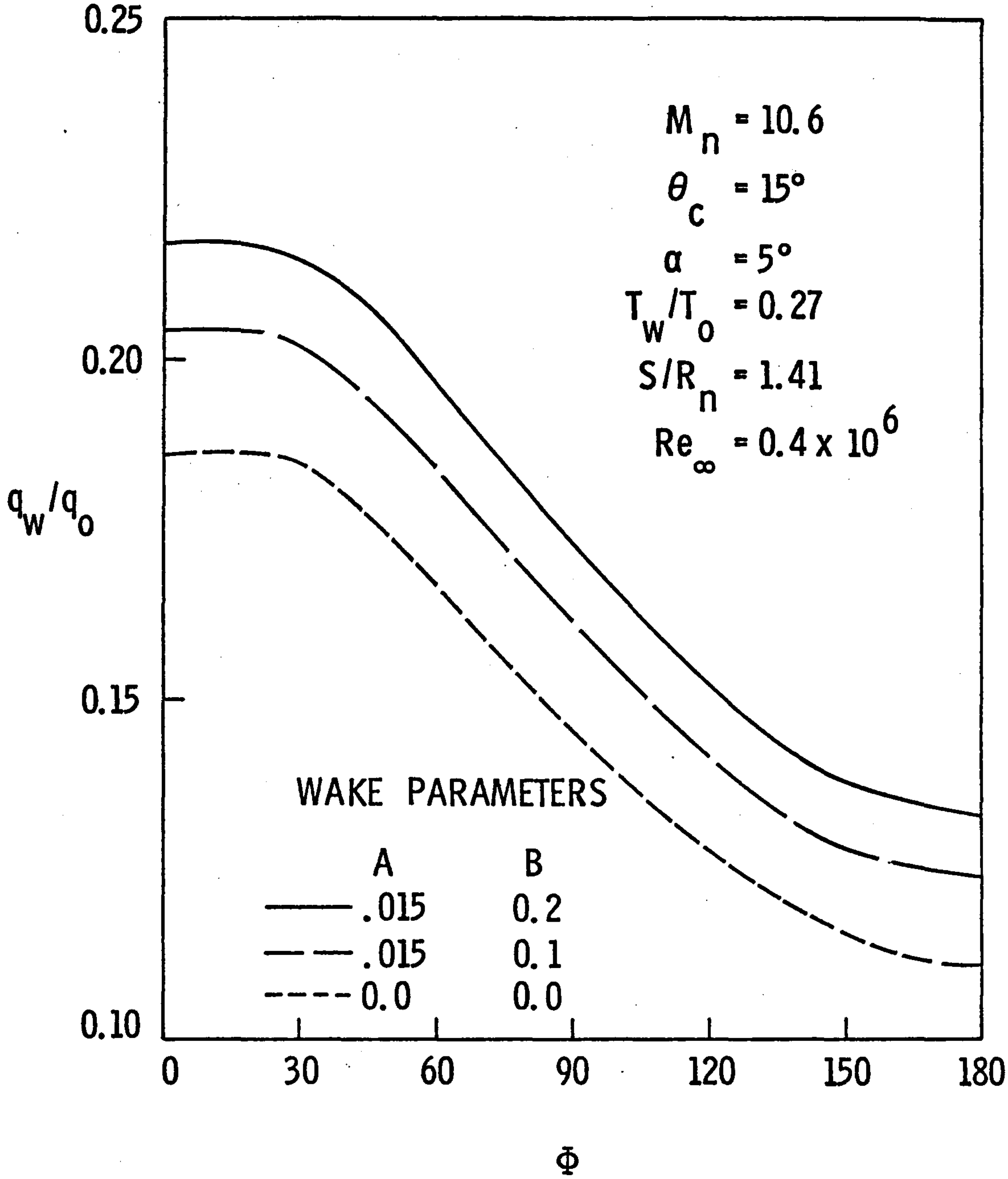

Figure 48. Nondimensional Heat Transfer Rate Around a Blunt Cone at 5^o Angle of Attack in Uniform Flow and Axisymmetric Wake Flows at S/R_n = 1.41

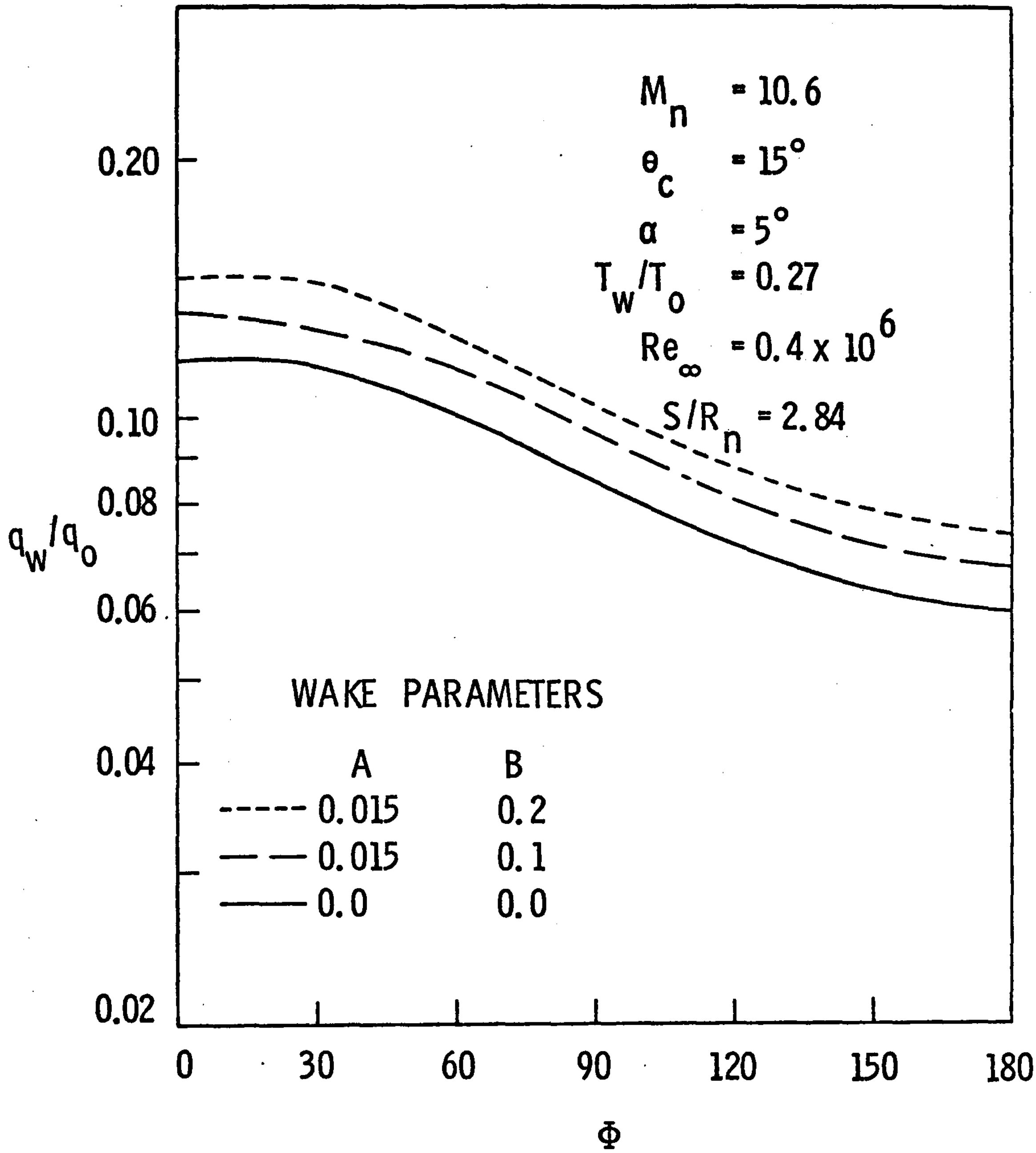

Figure 49. Nondimensional Heat Transfer Rate Around a Blunt Cone at 5° Angle of Attack in Uniform Flow and Axisymmetric Wake Flows at S/R_n = 2.84

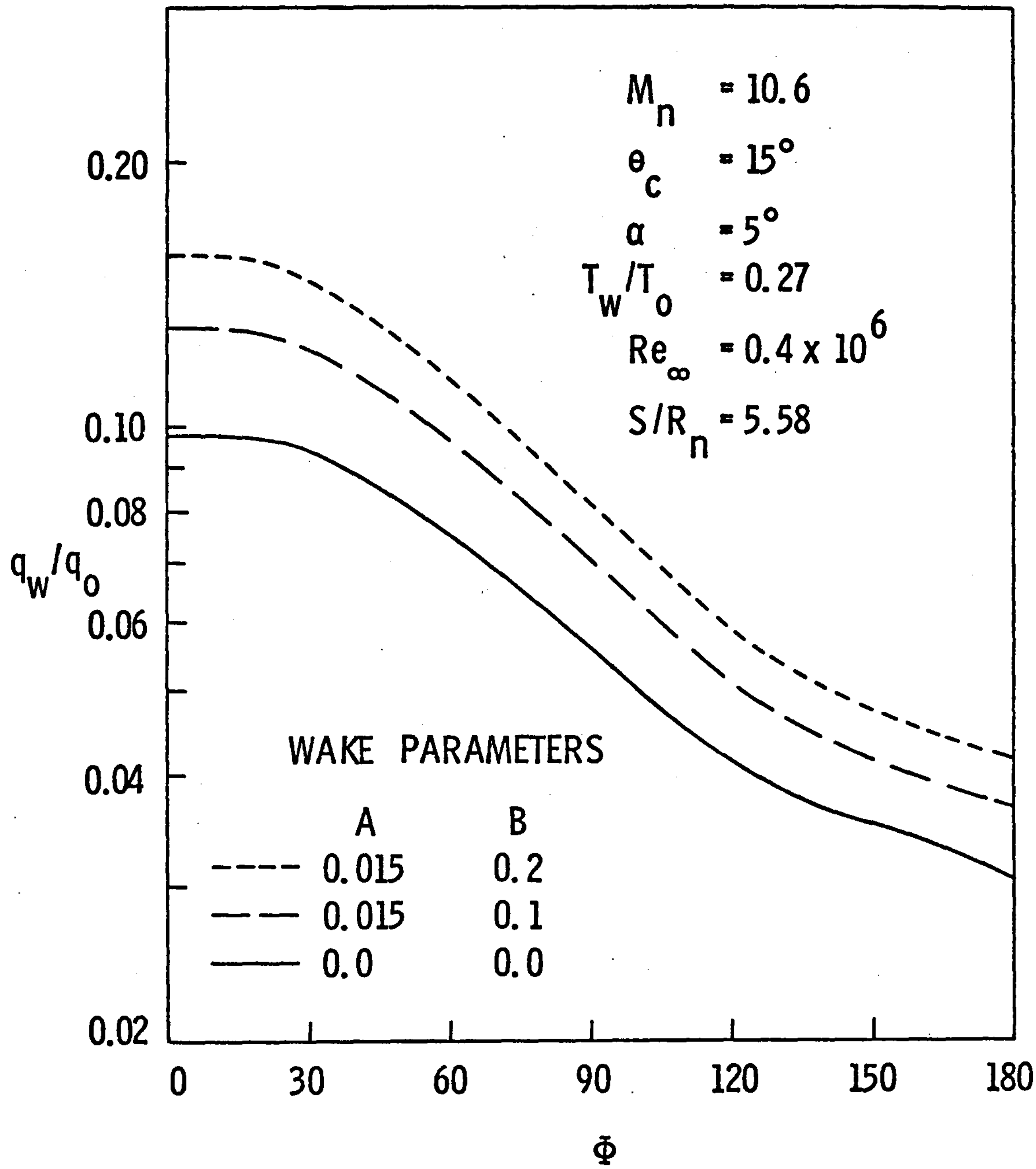

Figure 50. Nondimensional Heat Transfer Rate Around a Blunt Cone at 5° Angle of Attack in Uniform Flow and Axisymmetric Wake Flows at S/R_n = 5.58

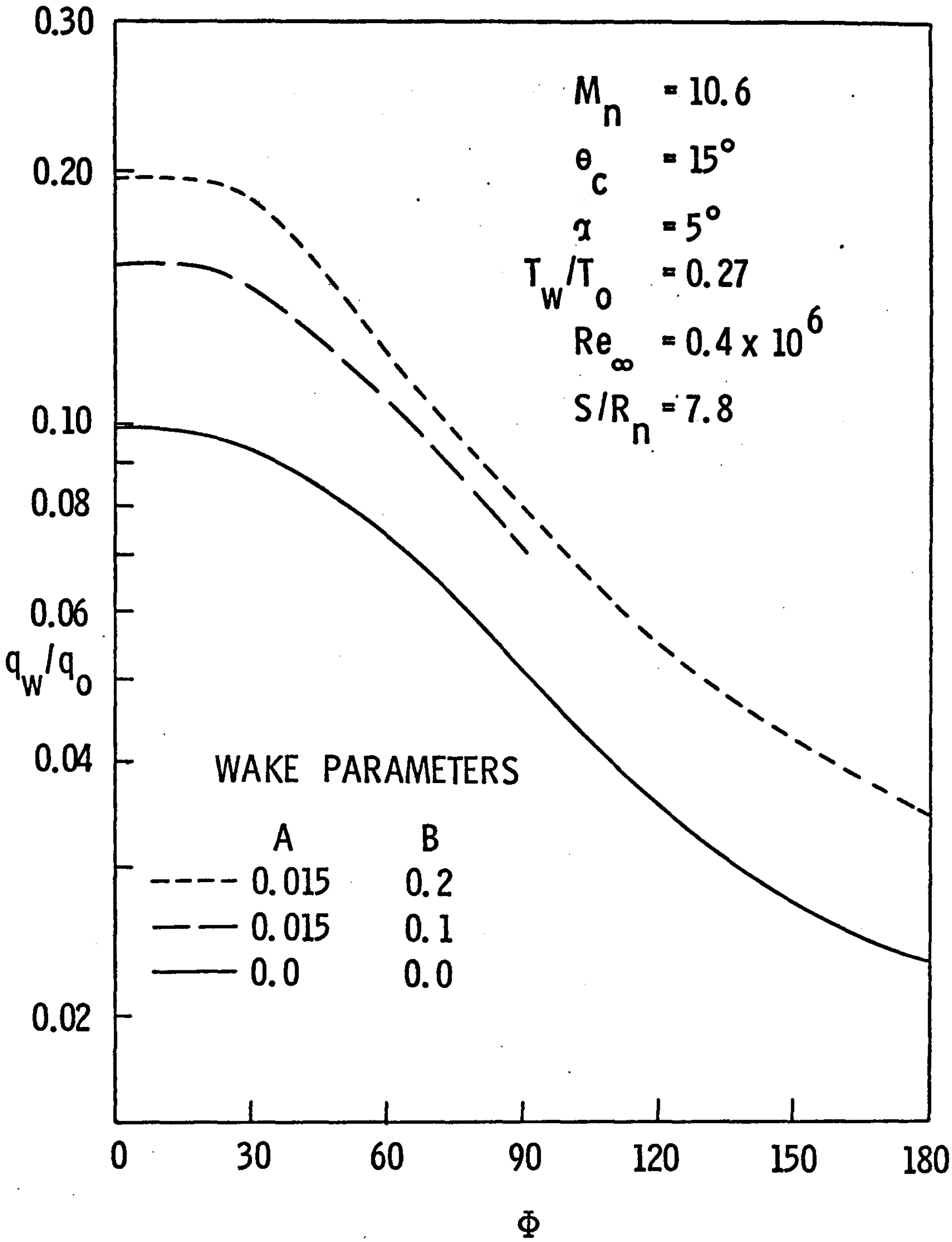

Figure 51. Nondimensional Heat Transfer Rate Around a Blunt Cone at 5° Angle of Attack in Uniform Flow and Axisymmetric Wake Flows at S/R_n = 7.8

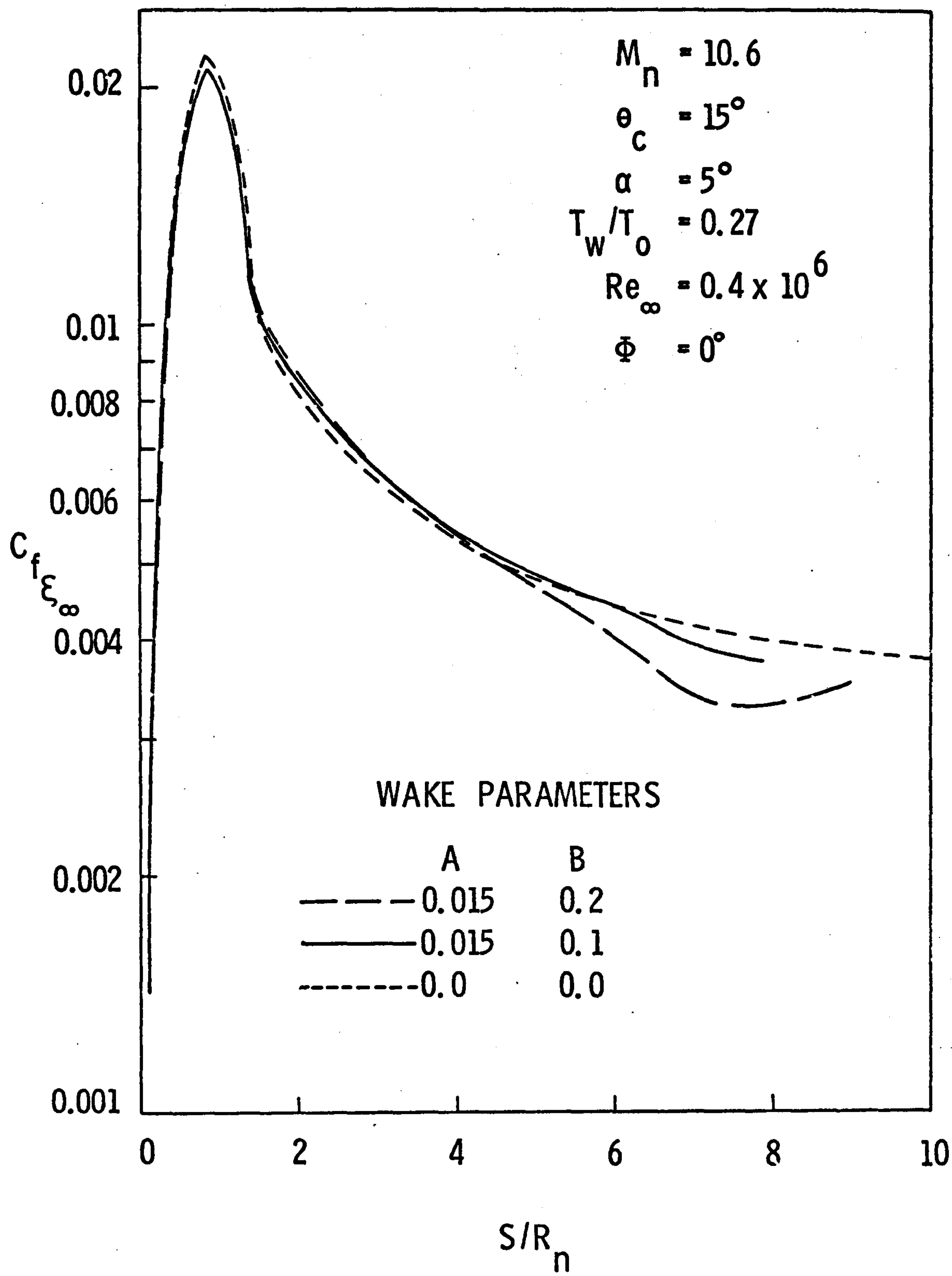

Figure 52. Lontitudinal Skin Friction Coefficient Along the Windward Streamline of a Blunt Cone at 5° Angle of Attack in Uniform Flow and Axisymmetric Wake Flows

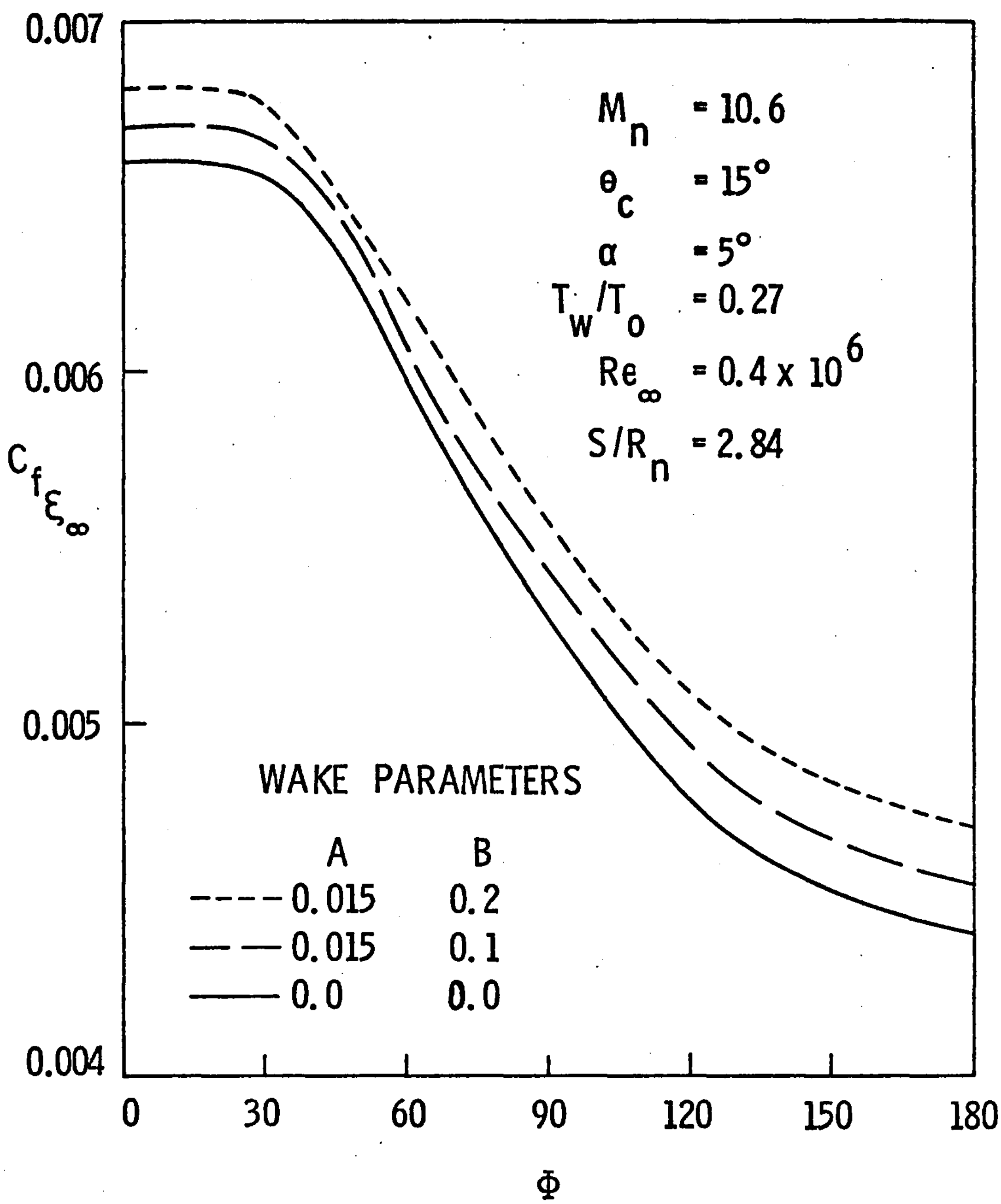

Figure 53. Longitudinal Skin Friction Coefficient Around a Blunt Cone at 5° Angle of Attack in Uniform Flow and Axisymmetric Wake Flows at S/R_n = 2.84

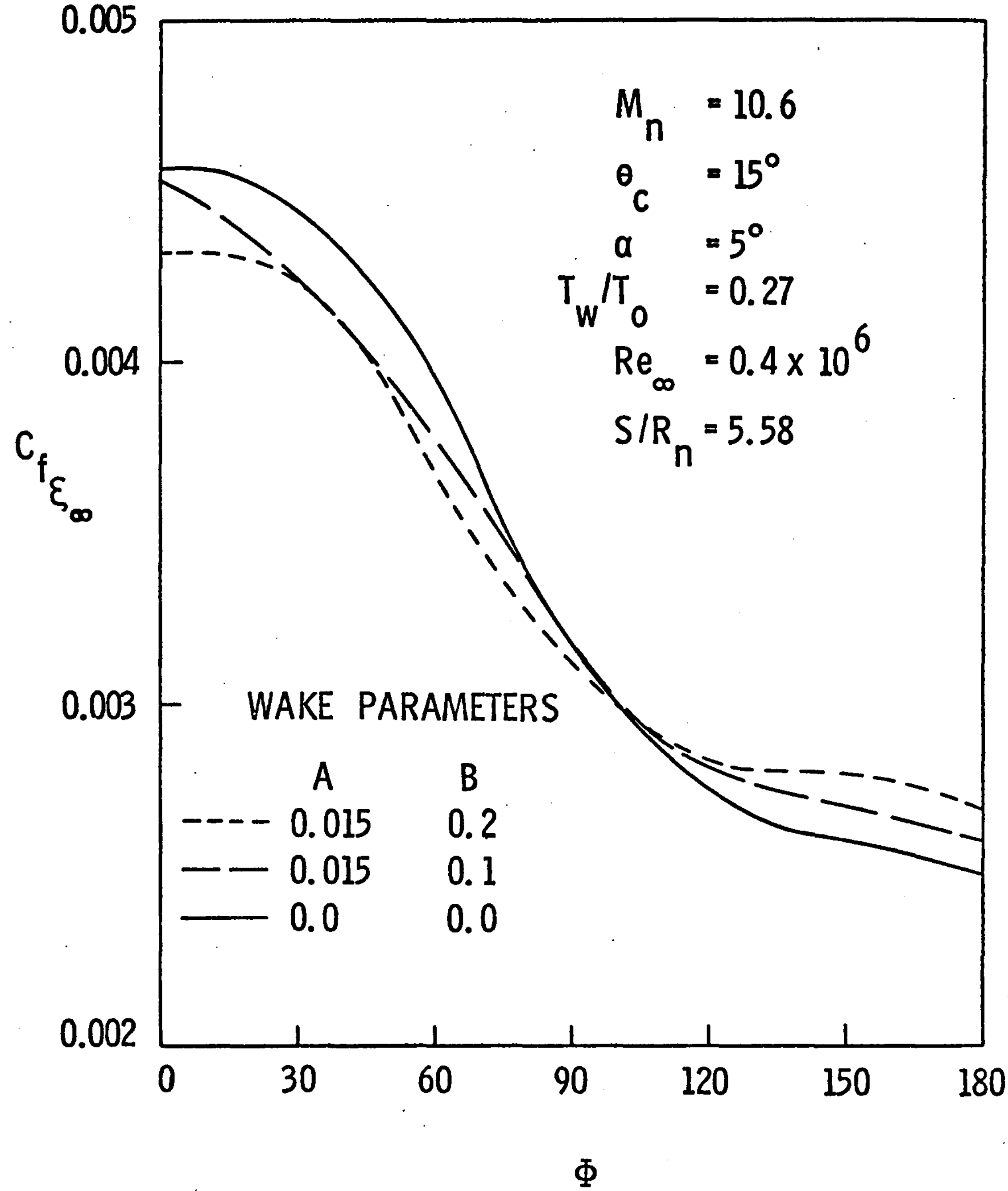

Figure 54. Longitudinal Skin Friction Coefficient Around a Blunt Cone at 5° Angle of Attack in Uniform Flow and Axisymmetric Wake Flows at $S/R_n = 5.58$

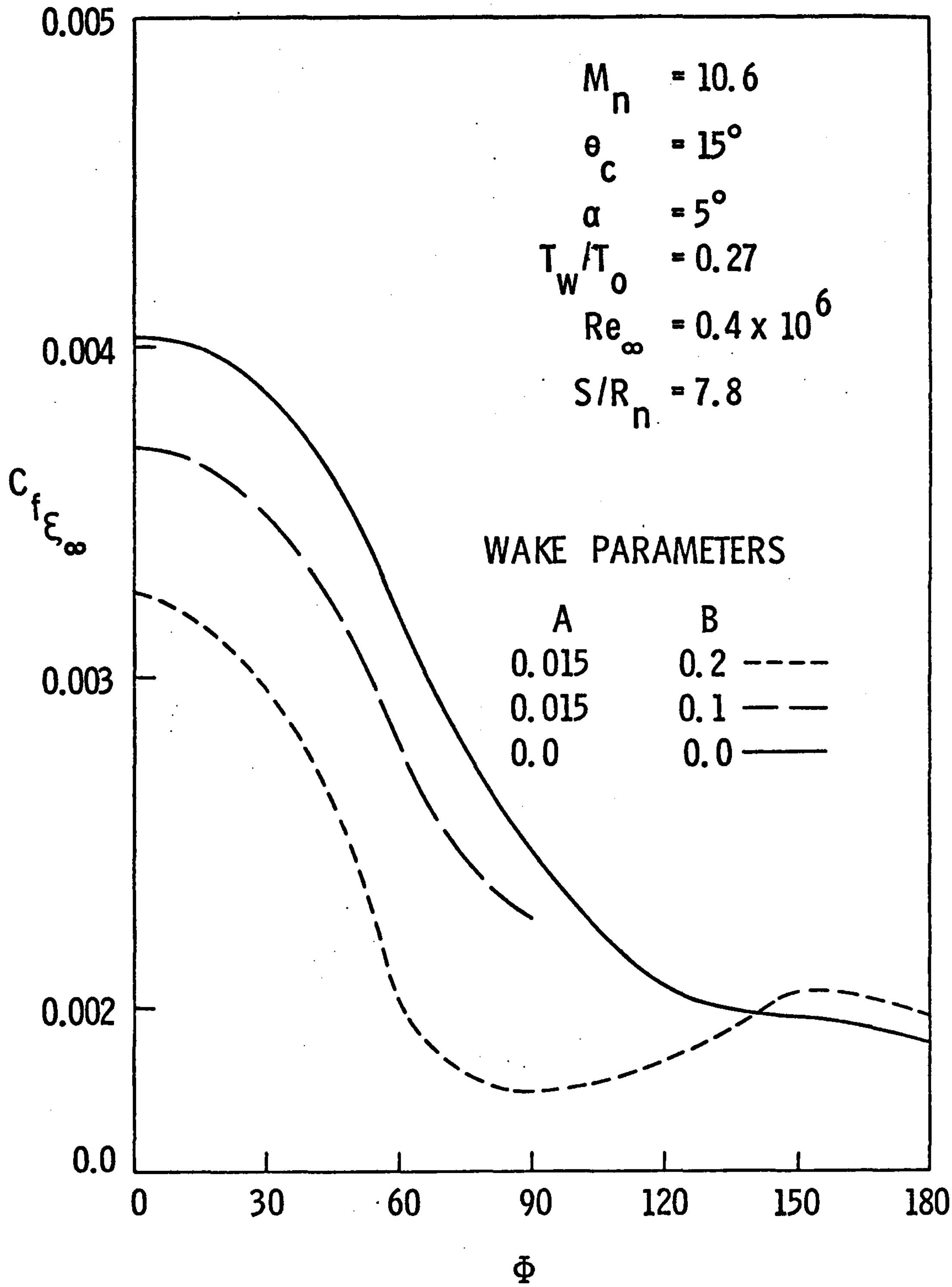

Figure 55. Longitudinal Skin Friction Coefficient Around a Blunt Cone at 5° Angle of Attack in Uniform Flow and Axisymmetric Wake Flows at S/R_n = 7.8

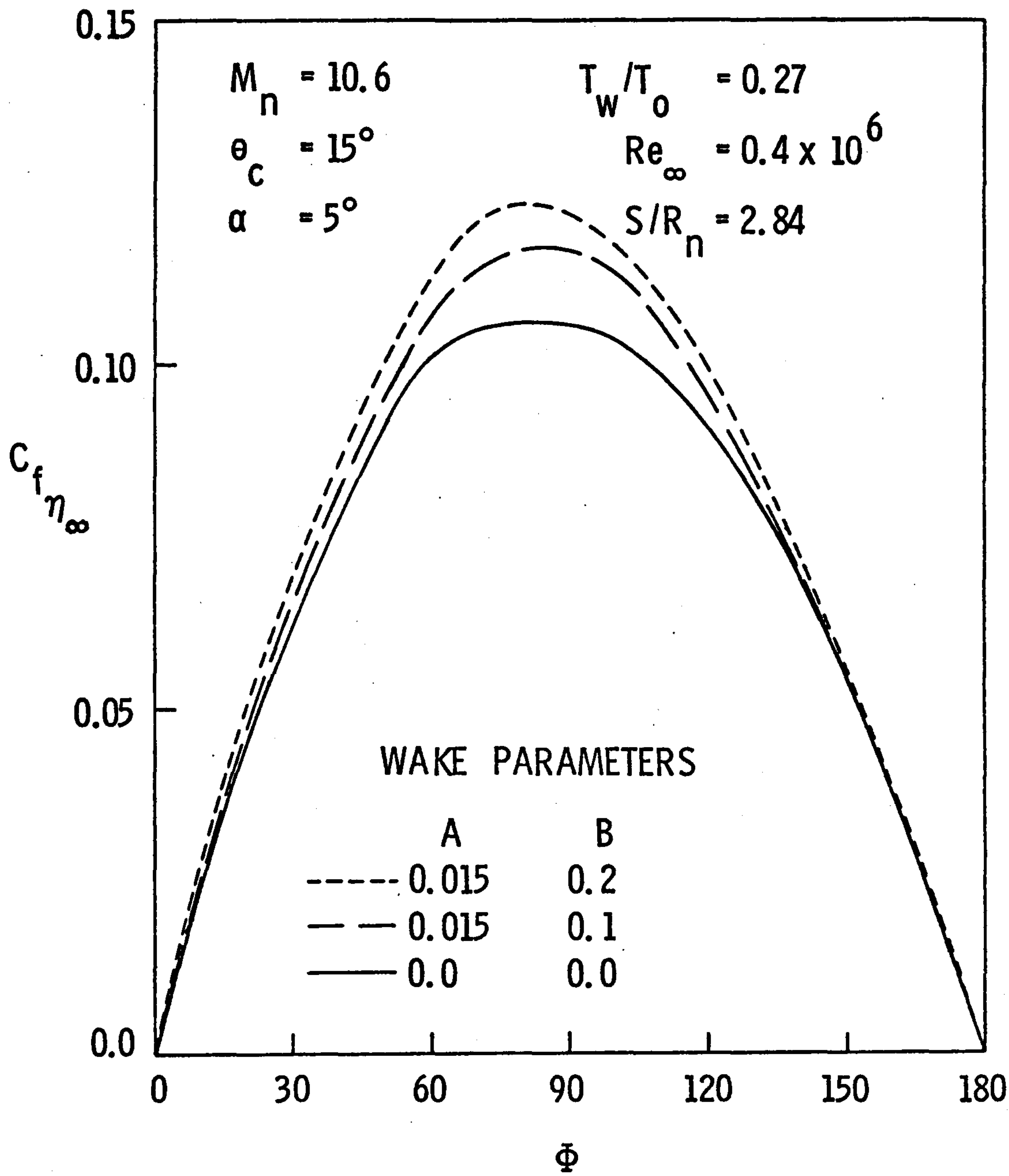

Figure 56. Transverse Skin Friction Coefficient Around a Blunt Cone at 5° Angle of Attack in Uniform Flow and Axisymmetric Wake Flows at S/R_n = 2.84

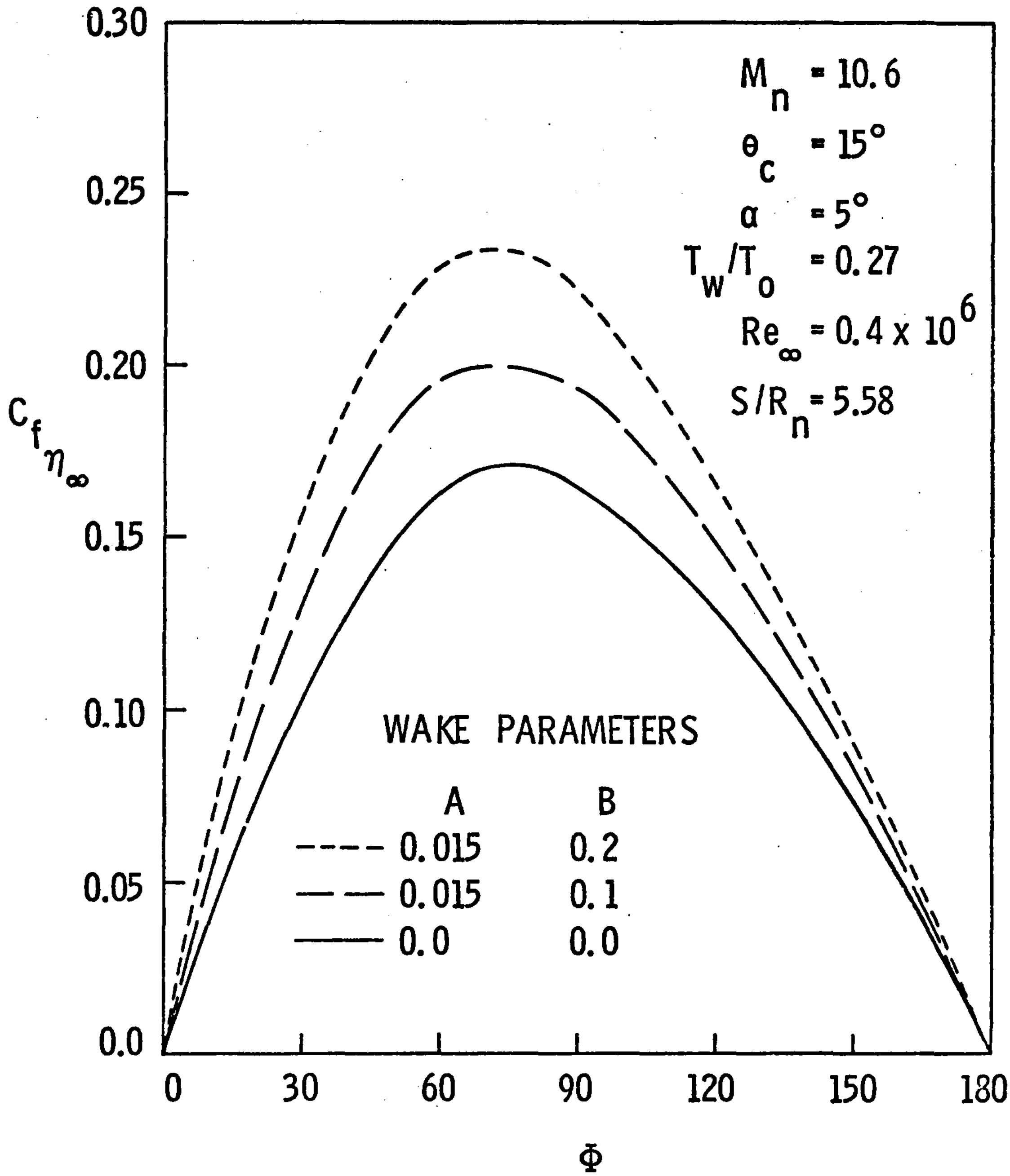

Figure 57. Transverse Skin Friction Coefficient Around a Blunt Cone at 5° Angle of Attack in Uniform Flow and Axisymmetric Wake Flows at S/R_n = 5.58

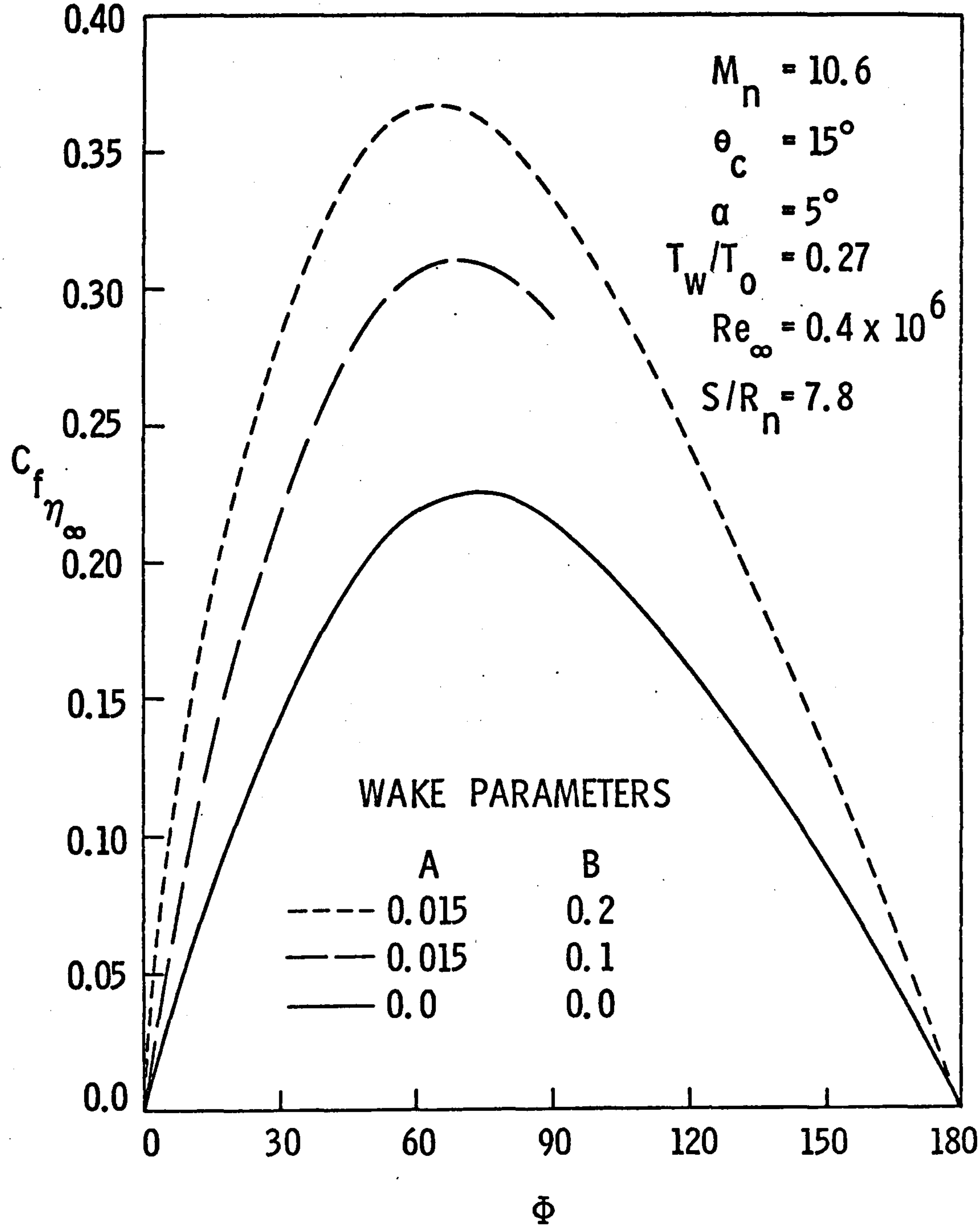

Figure 58. Transverse Skin Friction Coefficient Around a Blunt Cone at 5° Angle of Attack in Uniform Flow and Axisymmetric Wake Flows at S/R_n = 7.8

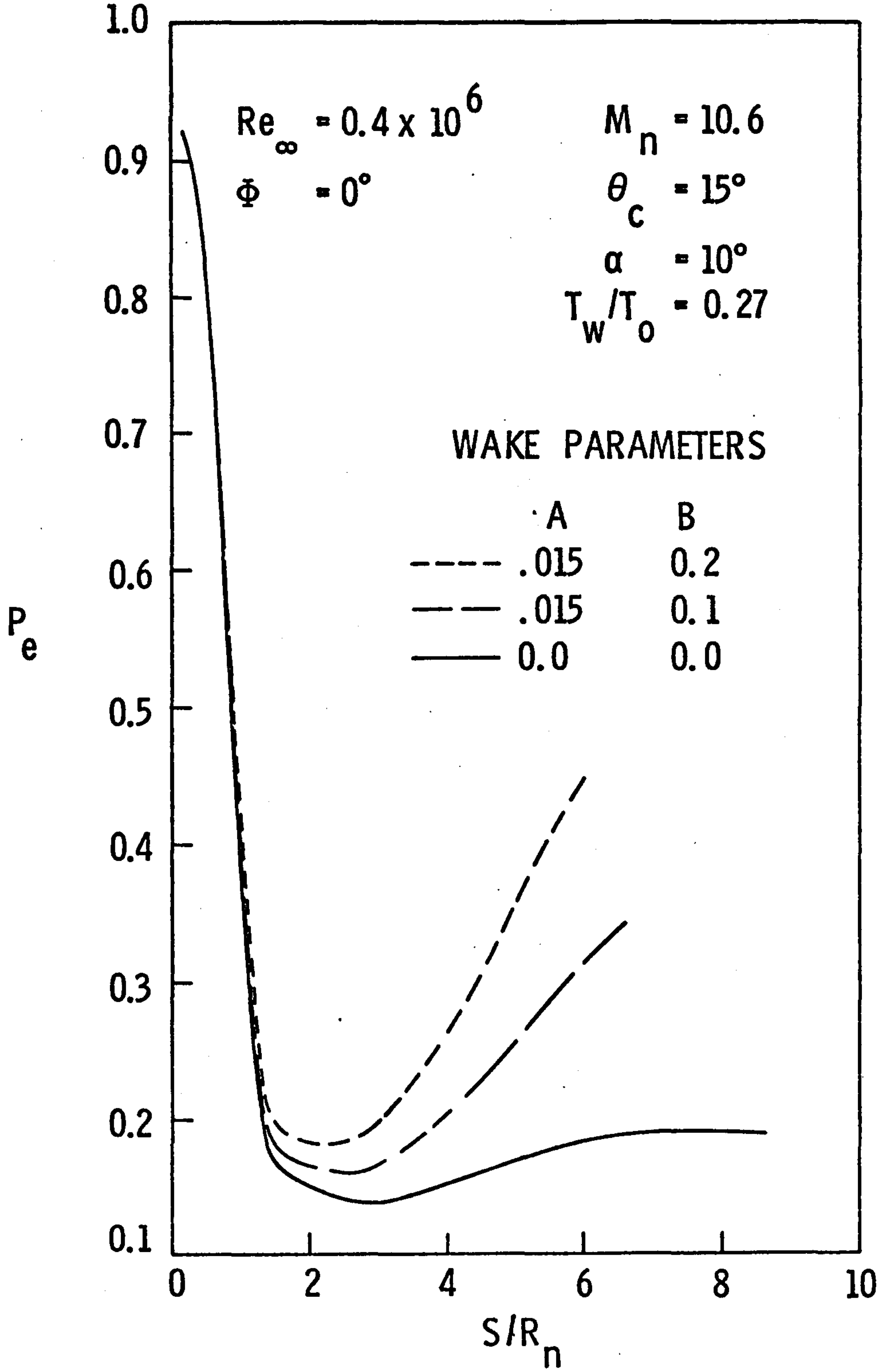

Figure 59. Pressure Distribution Along the Windward Streamline of a Blunt Cone at 10° Angle of Attack in Uniform Flow and Axisymmetric Wake Flows

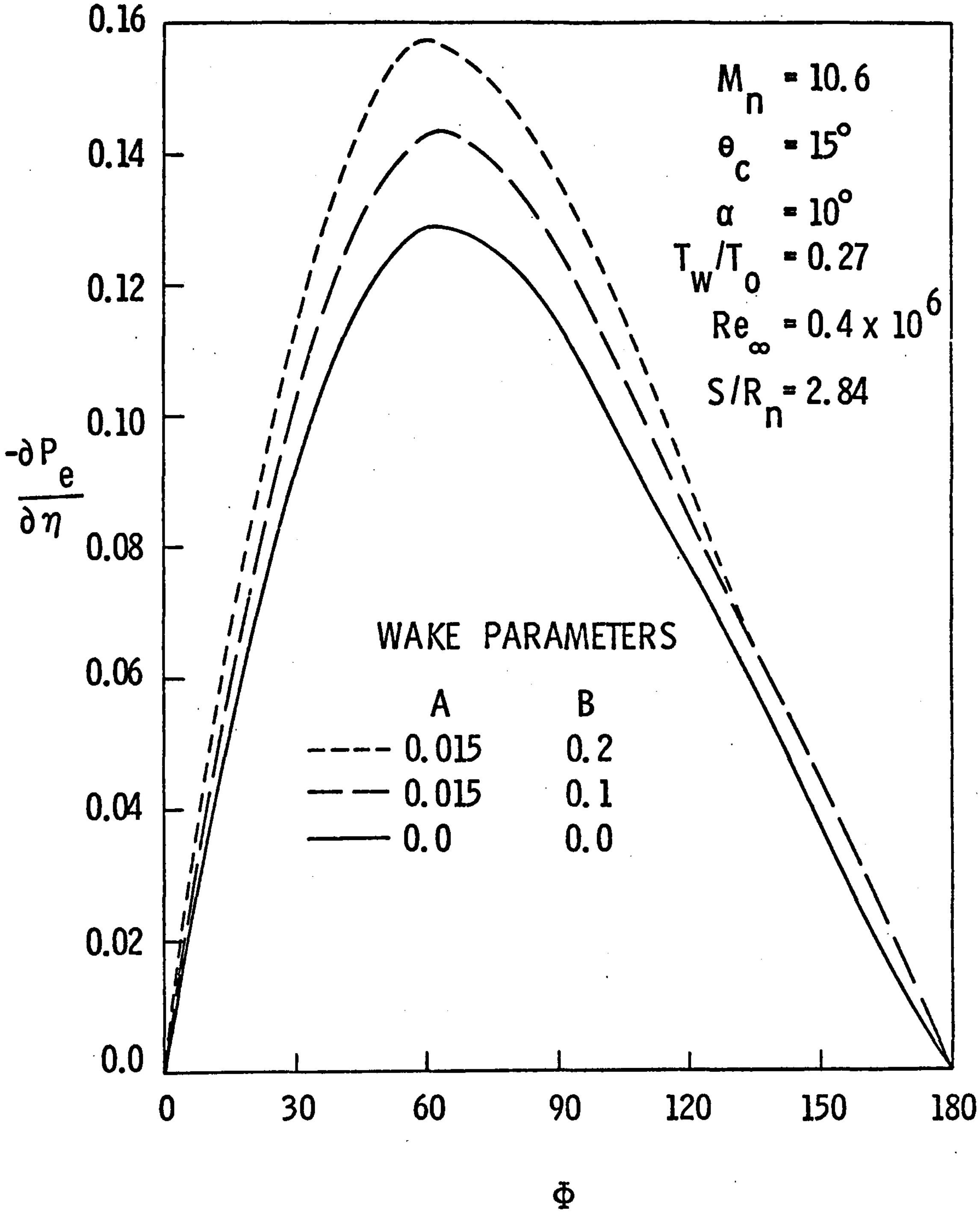

Figure 60. Transverse Pressure Gradient Around a Blunt Cone at 10° Angle of Attack in Uniform Flow and Axisymmetric Wake Flows at $S/R_n = 2.84$

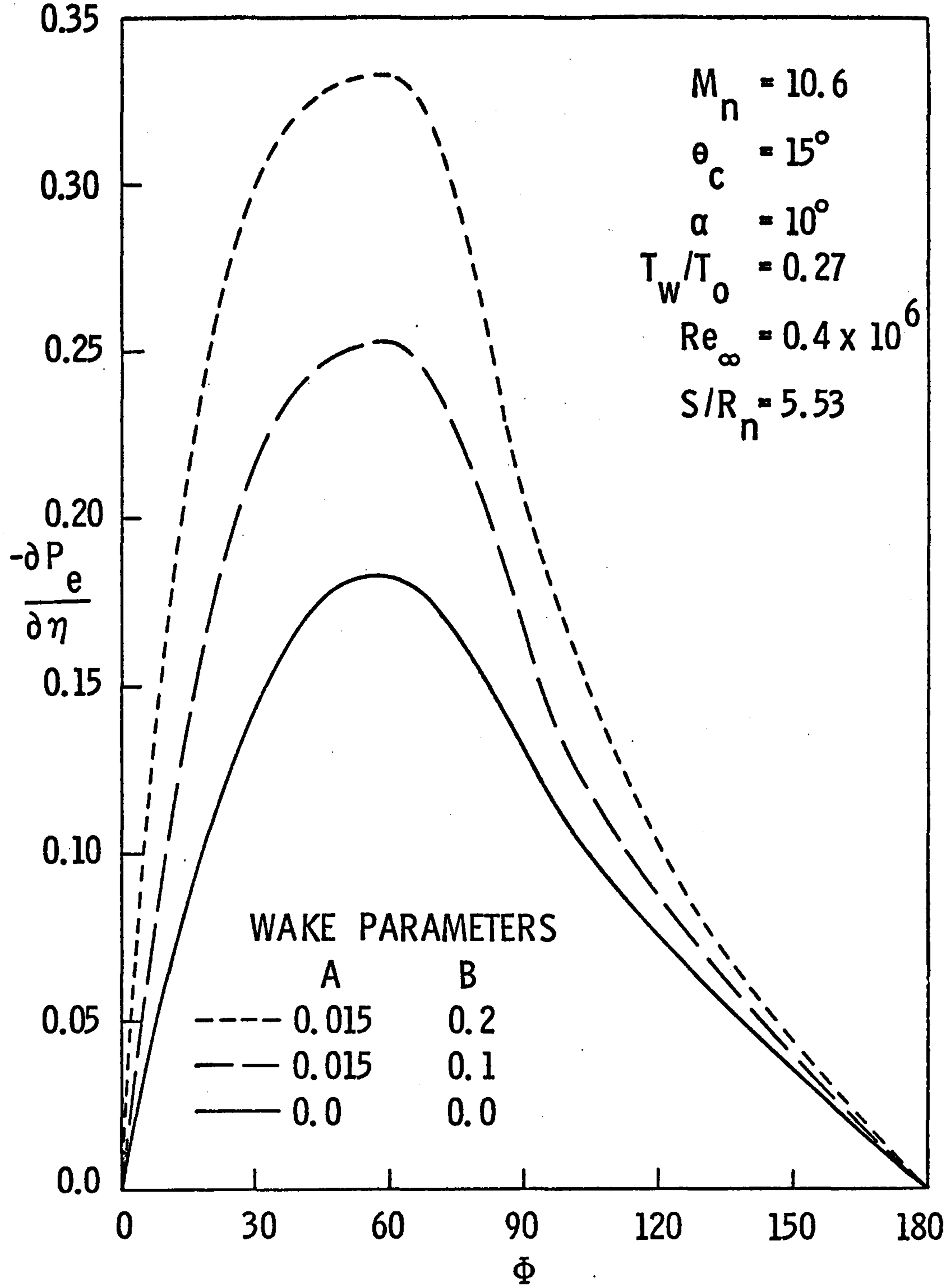

Figure 61. Transverse Pressure Gradient Around a Blunt Cone at 10° Angle of Attack in Uniform Flow and Axisymmetric Wake Flows at $S/R_n = 5.53$

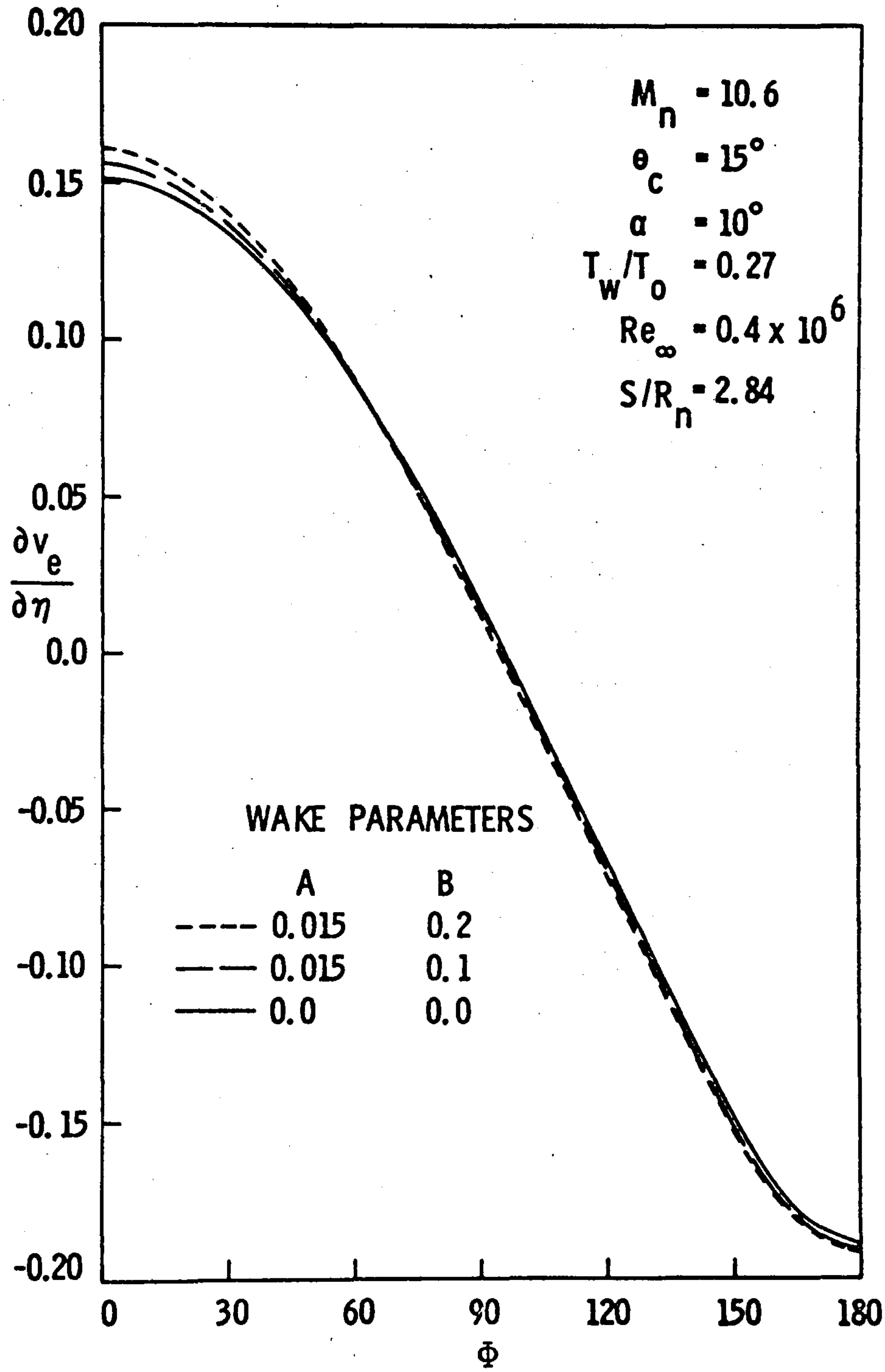

Figure 62. Cross Flow Velocity Derivative Around a Blunt Cone at 10° Angle of Attack in Uniform and Axisymmetric Wake Flows at S/R_n = 2.84

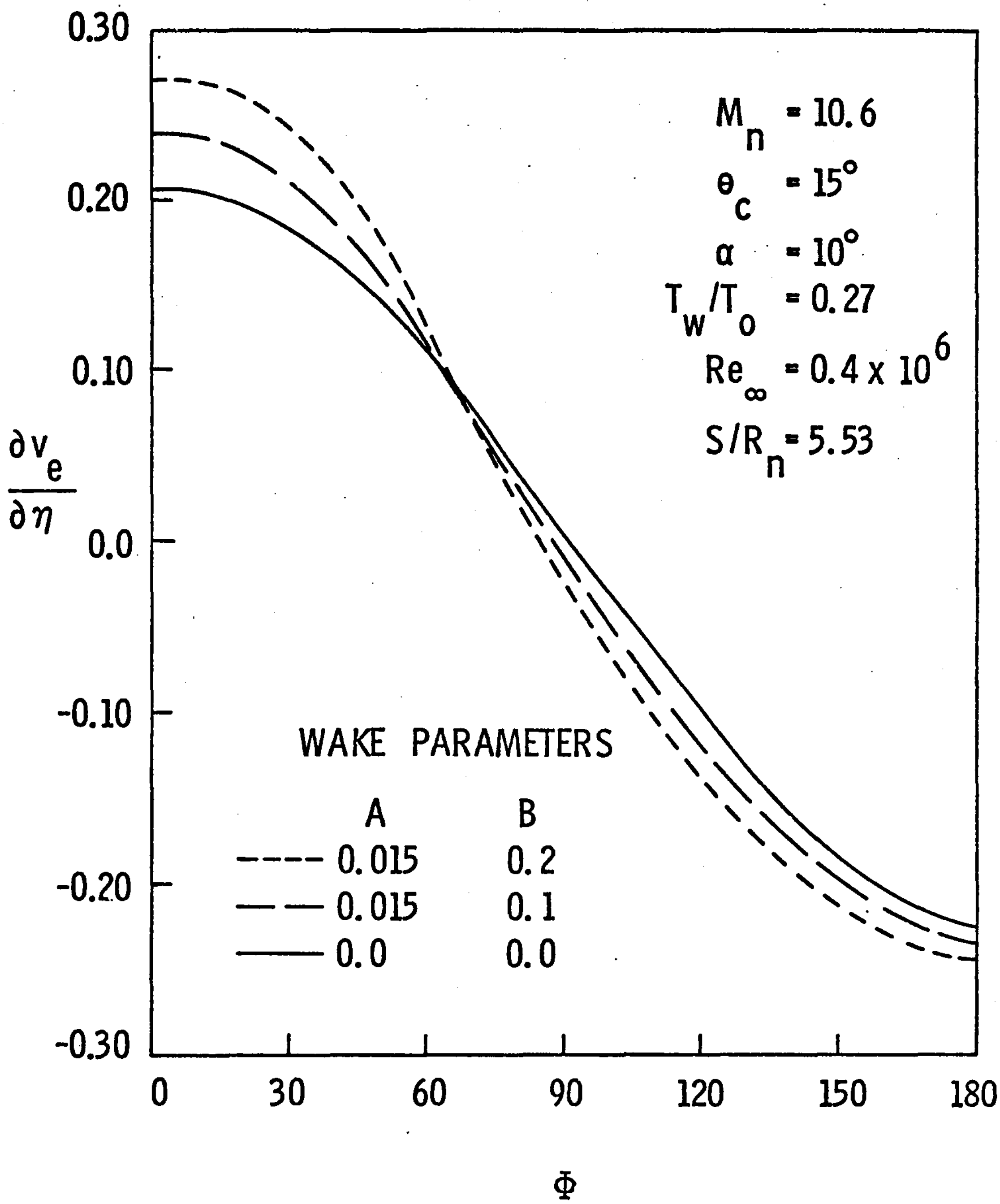

Figure 63. Cross Flow Velocity Derivative Around a Blunt Cone at 10° Angle of Attack in Uniform Flow and Axisymmetric Wake Flows at S/R_n = 5.53

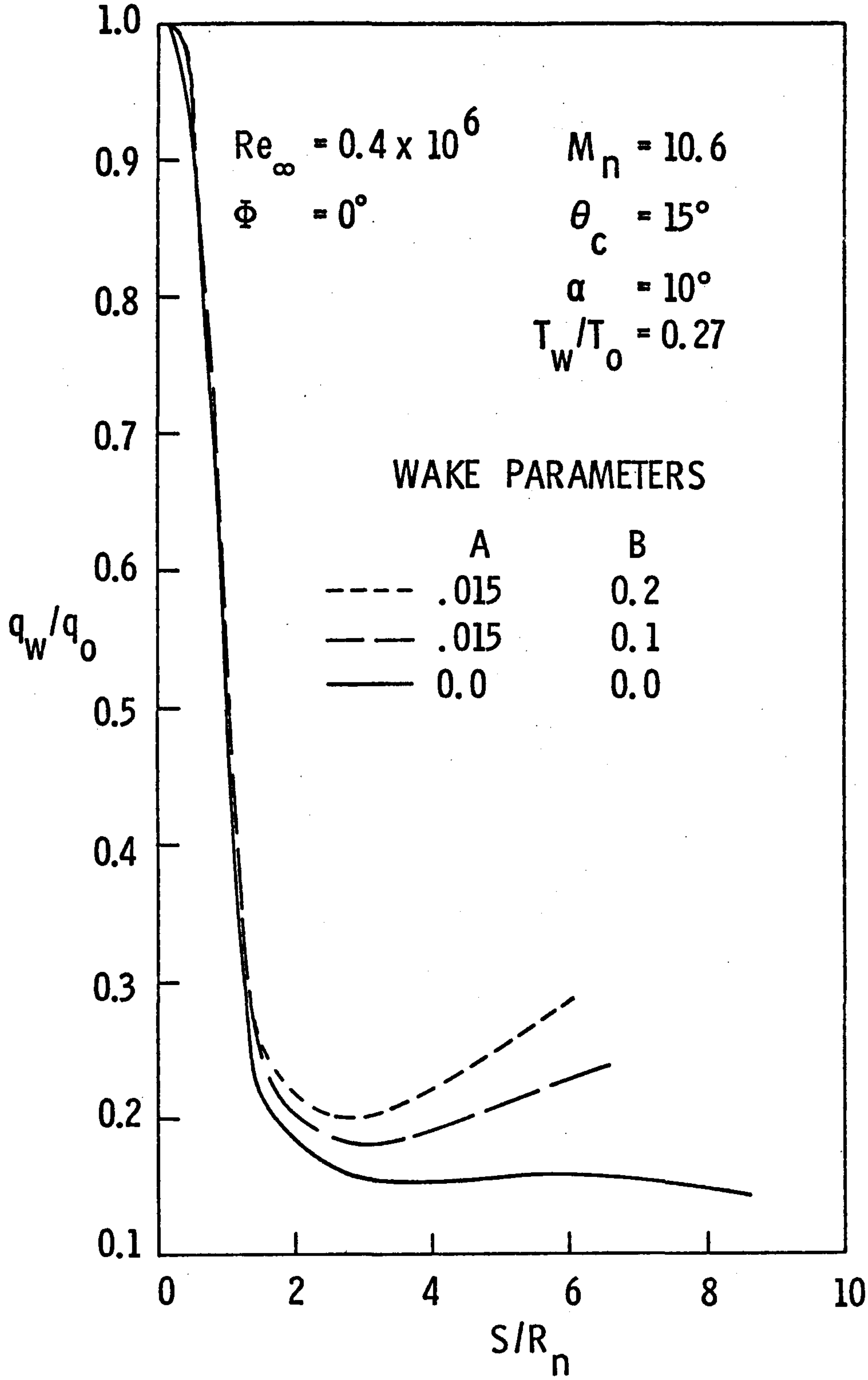

Figure 64. Nondimensional Heat Transfer Rate Along the Windward Streamline of a Blunt Cone at 10° Angle of Attack in Uniform Flow and Axisymmetric Wake Flows

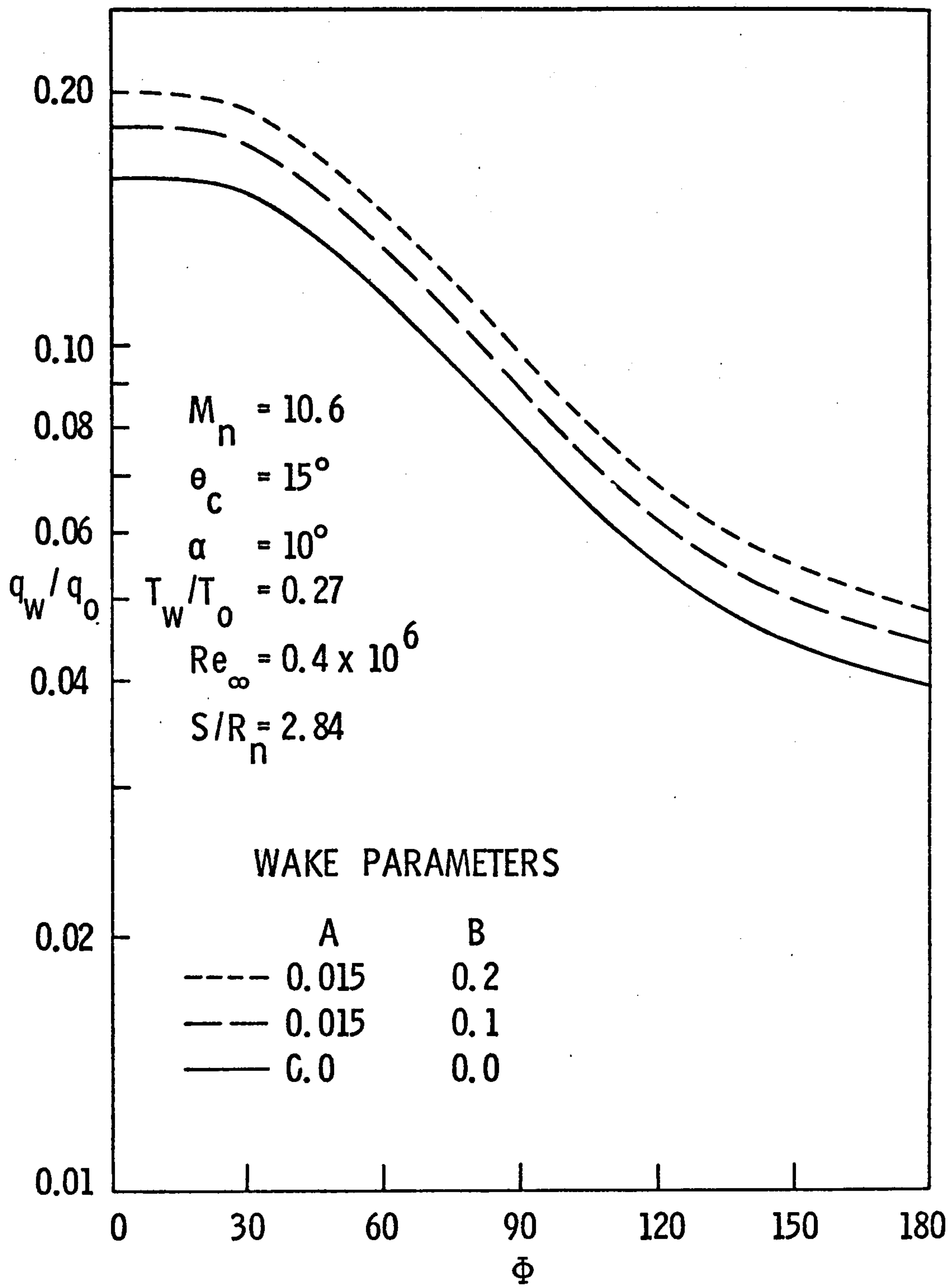

Figure 65. Nondimensional Heat Transfer Rate Around a Blunt Cone at 10° Angle of Attack in Uniform Flow and Axisymmetric Wake Flows at S/R_n = 2.84

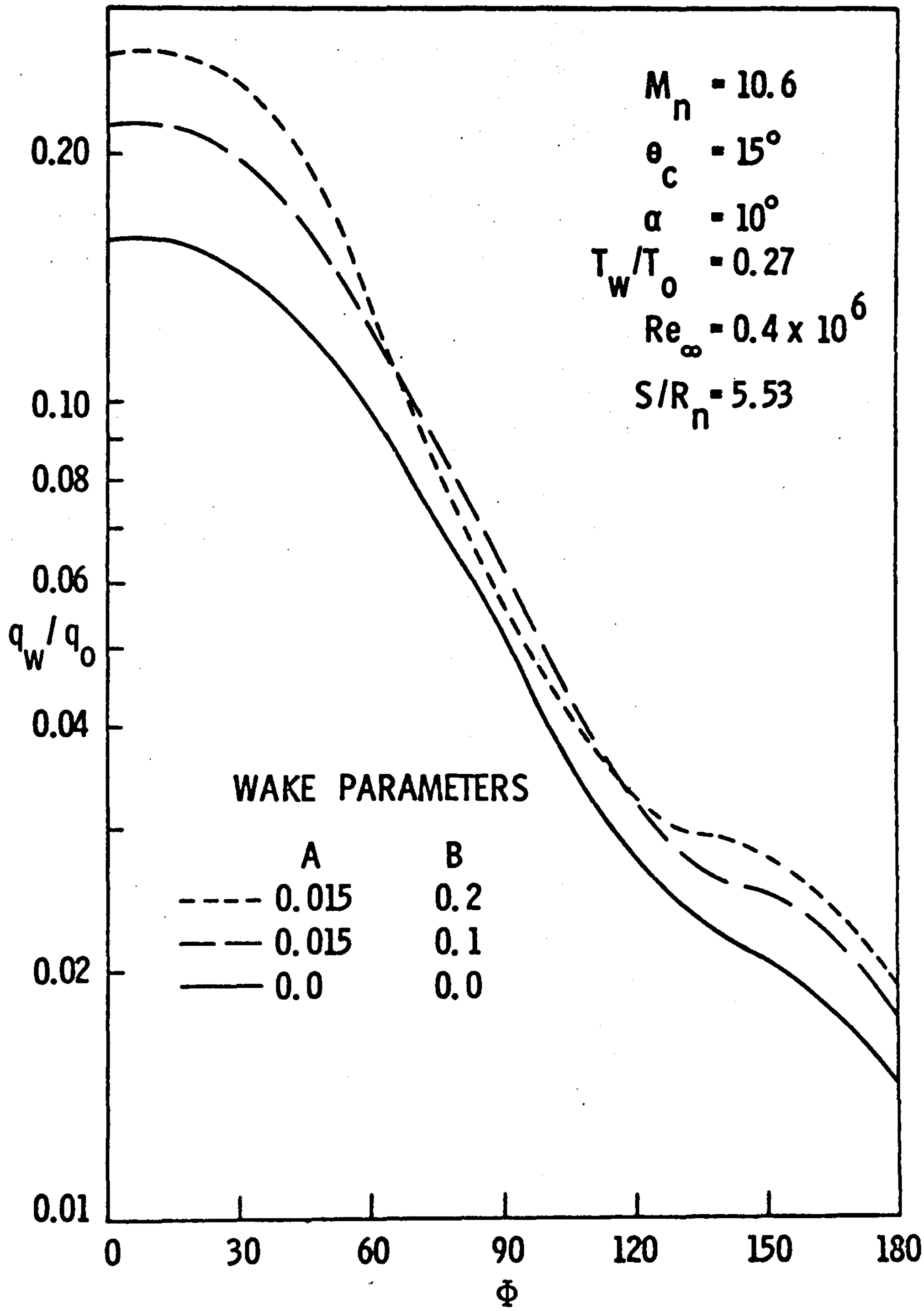

Figure 66. Nondimensional Heat Transfer Rate Around a Blunt Cone at 10° Angle of Attack in Uniform Flow and Axisymmetric Wake Flows at S/R_n = 5.53

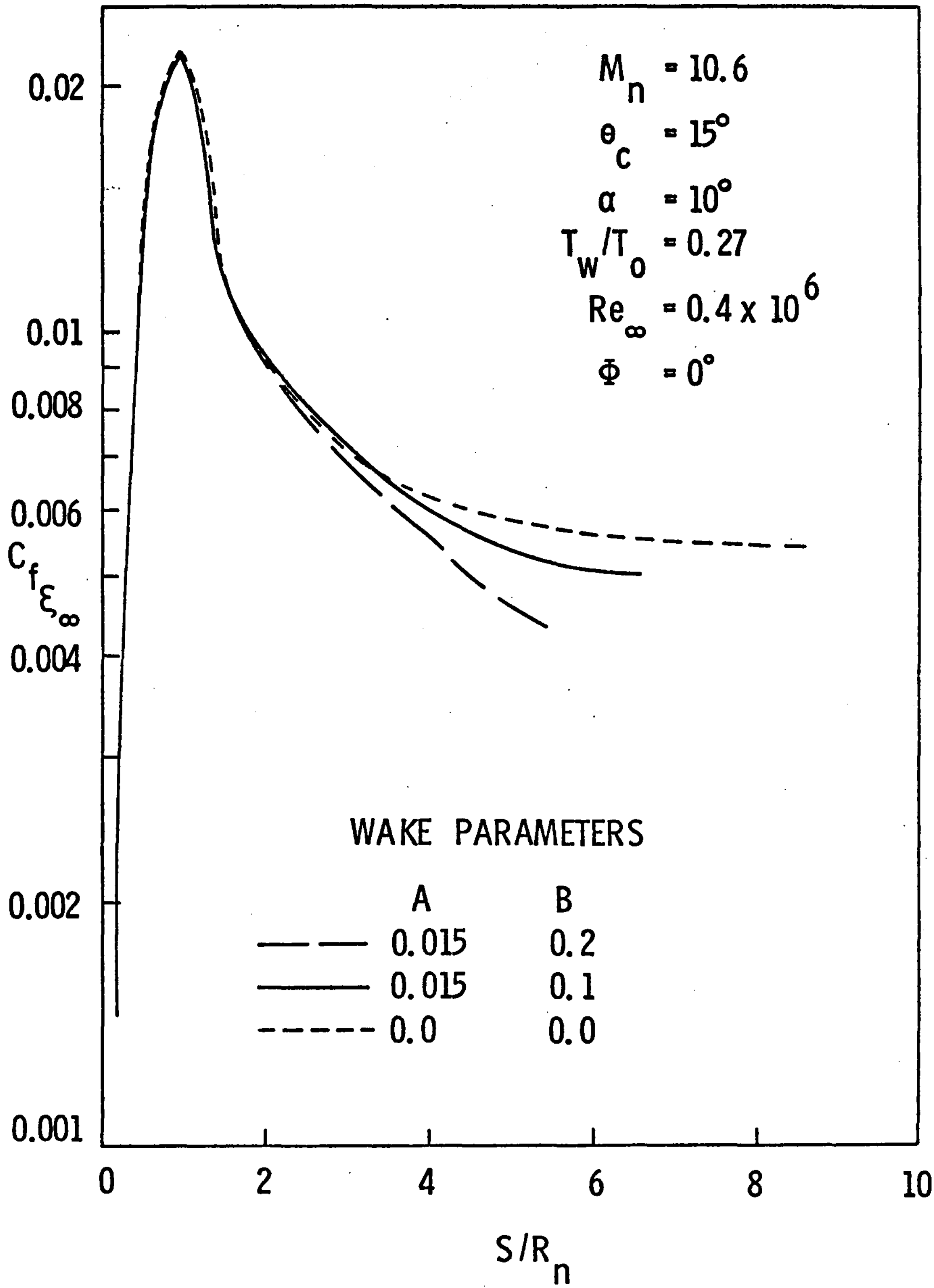

Figure 67. Longitudinal Skin Friction Coefficient Along the Windward Streamline of a Blunt Cone at 10° Angle of Attack in Uniform Flow and Axisymmetric Wake Flows

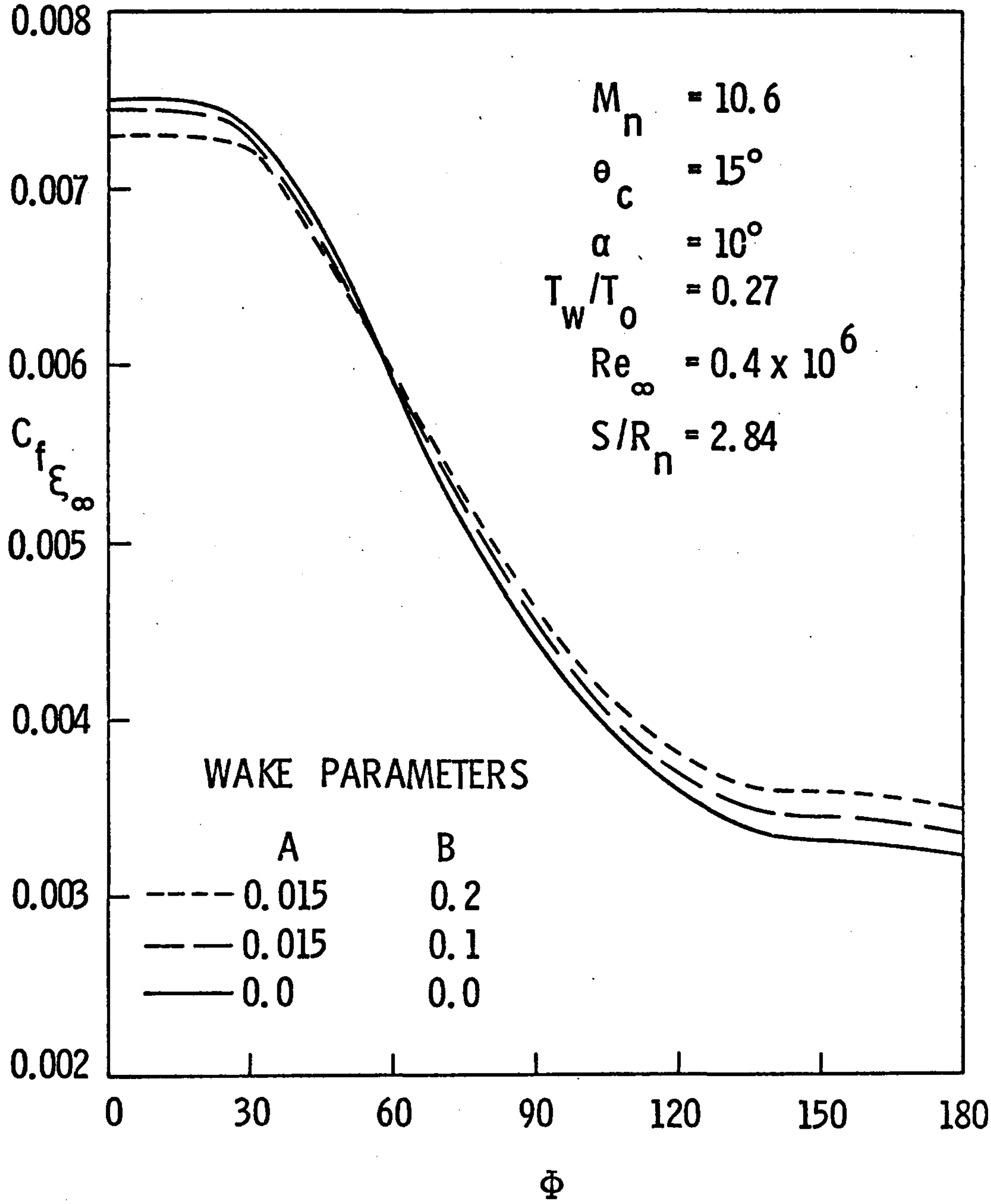

Figure 68. Longitudinal Skin Friction Coefficient Around a Blunt Cone at 10° Angle of Attack in Uniform Flow and Axisymmetric Wake Flows at S/R_n = 2.84

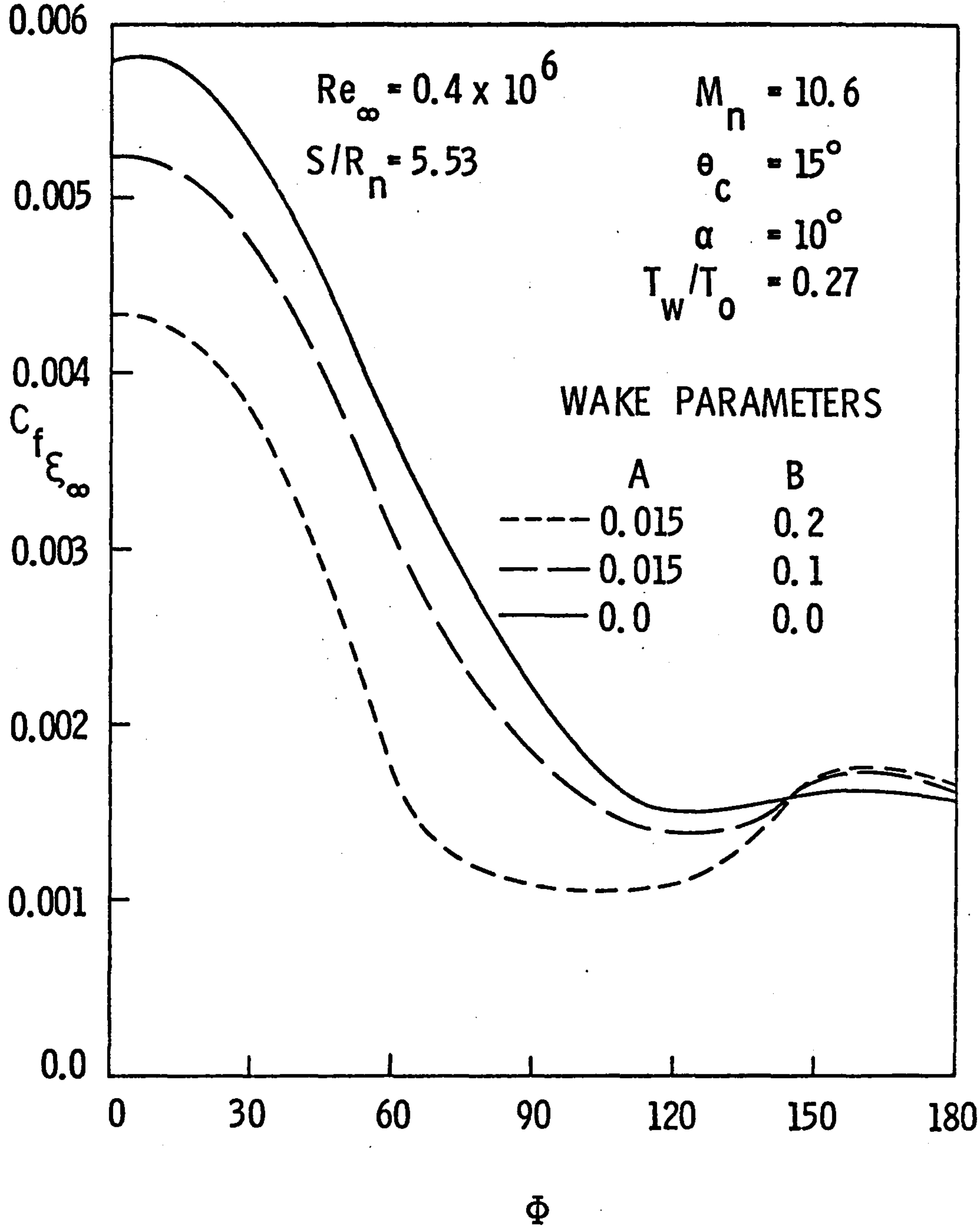

Figure 69. Longitudinal Skin Friction Coefficients Around a Blunt Cone at 10° Angle of Attack in Uniform Flow and Axisymmetric Wake Flows at $S/R_n = 5.53$

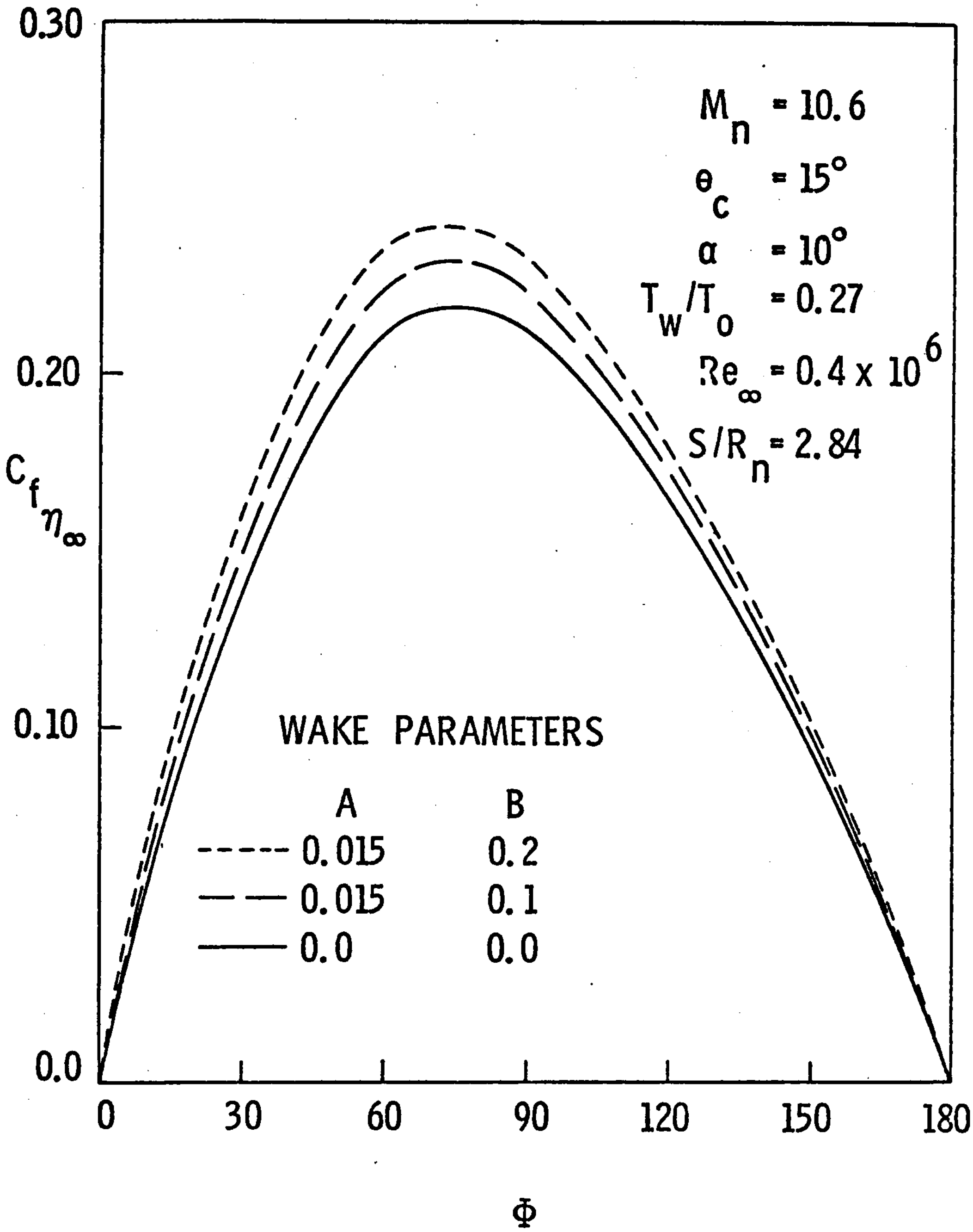

Figure 70. Transverse Skin Friction Coefficient Around a Blunt Cone at 10° Angle of Attack in Uniform Flow and Axisymmetric Wake Flows at S/R_n = 2.84

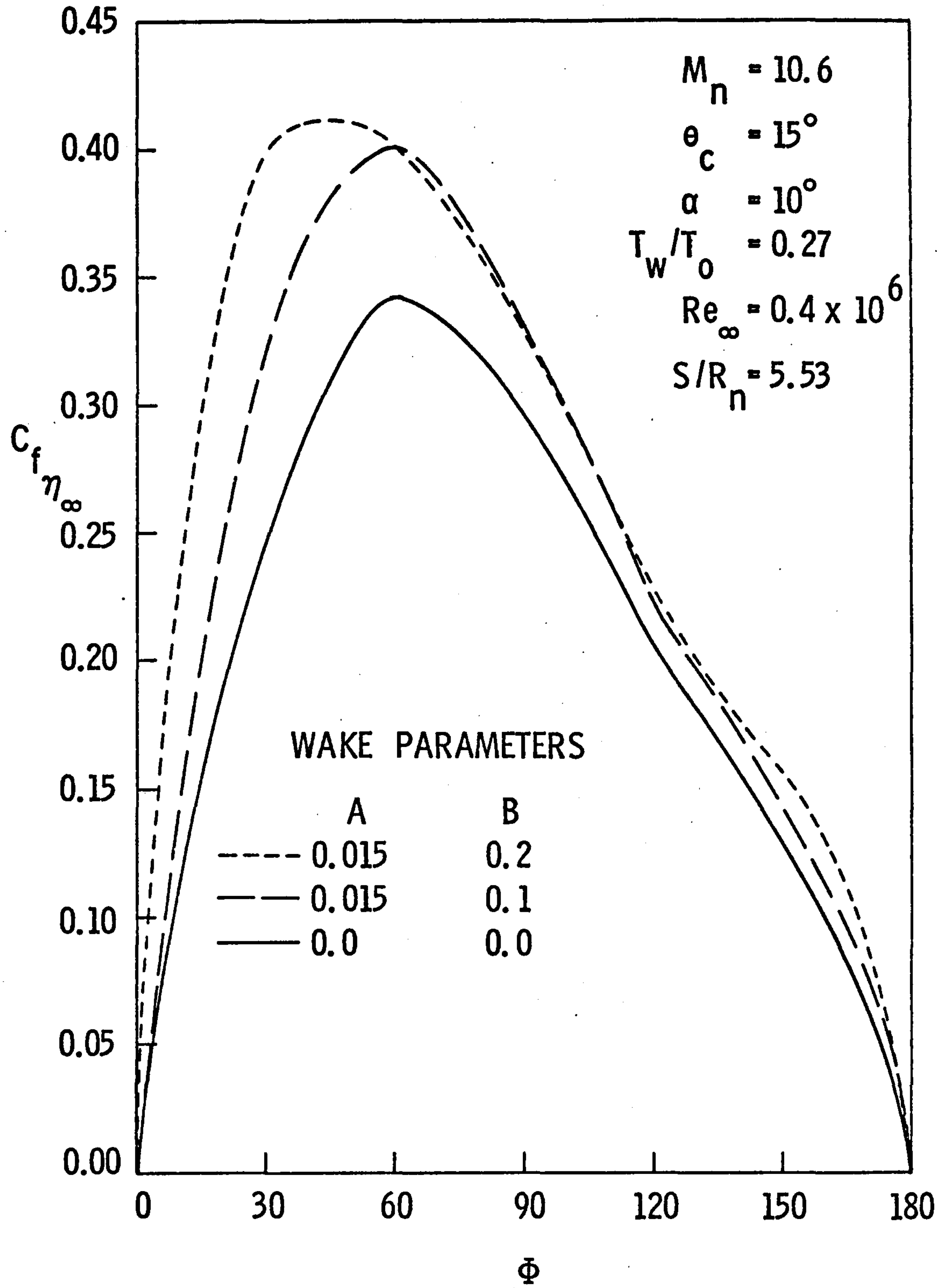

Figure 71. Transverse Skin Friction Coefficient Around a Blunt Cone at 10° Angle of Attack in Uniform Flow and Axisymmetric Wake Flows at S/R_n = 5.53

The vita has been removed from
the scanned document

BOUNDARY LAYER FLOWS OVER SHARP AND

SPHERICALLY BLUNTED CONES AT ANGLE OF ATTACK

TO SUPERSONIC NONUNIFORM FREE STREAMS

by

Michael C. Frieders

(ABSTRACT)

Methods have been developed to solve the problem of laminar boundary layers on sharp and spherically blunt cones at angle of attack to nonuniform supersonic free streams. A three-dimensional boundary-layer solution is used to solve sharp cone problems and the afterbody of blunt cone problems. An axisymmetric boundary-layer solution is used to solve the axisymmetric region of blunt cones. An interpolation method has been developed enabling the use of axisymmetric solution data as starting data for the three-dimensional boundary layer solution on a blunt cone. An existing implicit finite-difference numerical scheme was used to solve both the axisymmetric and three-dimensional boundary-layer equations. Edge properties for a sharp cone and for the afterbody of a blunt cone come from method of characteristics solutions of the inviscid flow field. A modified inverse method for solving the inviscid flow field is used to provide edge properties for the axisymmetric region of blunt cones. Results obtained for blunt cones in uniform flow are compared to experimental data with good agreement. Uniform flow results for sharp cones are compared to experimental

data and to existing numerical data. Skin friction and heat transfer data obtained for sharp and blunt cones in nonuniform flow fields show a departure from the uniform flow values. Normalized skin friction and heat transfer coefficients for a sharp cone in two-dimensional shear flow increase downstream relative to conical flow values. The effect of wake flow on a blunt cone is to increase the heat transfer considerably, relative to uniform flow values. Downstream values of skin friction are shown to fall below uniform flow values. Decreasing the width of the wake causes more severe departure from uniform flow values, for both skin friction and heat transfer on blunt cones. The presence of free-stream nonuniformities hastened the onset of separation particularly in the blunt cone cases. The beginning of separation occurred sooner in both the longitudinal and transverse planes. Smaller width wakes and higher angles of attack caused earlier onset of separation.